Tides and Transport: Application to Lofoten and Vesterålen, Northern Norway

Eli Børve

Dissertation for the degree of Philosophiae Doctor (PhD)

Section for Meteorology and Oceanography

Department of Geosciences

University of Oslo

Series of dissertations submitted to the
Faculty of Mathematics and Natural Sciences, University of Oslo
No. 2471

ISSN 1501-7710

Cover: Hanne Baadsgaard Utigard.
Print production: Reprosentralen, University of Oslo.

:Preface

This synthesis and collection of papers are submitted for the degree of pilosophiae doctor (PhD) in physical oceanography at the Section for Meteorology and Oceanography (MetOs), Department of Geosciences, University of Oslo. The thesis consists of an introduction part and the following papers. Summary of all four papers, including author contributions, are specified in Chapter 4 of the introdution part.

Paper I: Ole Anders Nøst and **Eli Børve**, "Flow separation, dipole formation and water exchange through tidal strait", accepted for publication in Ocean Science

Paper II: **Eli Børve**, Pål Erik Isachsen, and Ole Anders Nøst, "Rectified tidal transport in Lofoten-Vesterålen, Northern Norway", in revision for Ocean Science.

Paper III: Jan Erik H. Weber and **Eli Børve** (2021), "Diurnal continental shelf waves with a permeable coastal boundary: Application to the shelf northwest of Norway", European Journal of Mechanics/B fluids, doi: 10.1016/j.euromechflu.2021.05.003

Paper IV: **Eli Børve**, Ole Anders Nøst, Pål Erik Isachsen, Peygham Ghaffari, Frank Gaardsted, Stig Falk-Petersen, "Tidal effects on transport and dispersion in the Lofoten and Vesterålen region, Northern Norway" (manuscript in preparation).

Other publications from the PhD period that are not included in the thesis:

I Jan Erik H. Weber and **Eli Børve**,"On group velocity and damping of diurnal continental shelf waves", submitted to Continental Shelf Research.

:Acknowledgements

First and foremost, I would like to thank my team of supervisors Pål Erik Isachsen and Ole Anders Nøst for guiding me through the challenging PhD path. The progress of a PhD is in many ways analogous to particle drift induced by nonlinear tidal dynamics, the path includes many steps back and forth, sometimes spinning in circles, but over time there is a (un)steady progress towards the final destination. I would like to thank you both for guidance, support and not least your patience along this journey. Your knowledge and expertise are truly appreciated.

I would also like to give a special thanks to Jan Erik H. Weber who enthusiastically brought me into the universe of continental shelf waves, and to Stig Falk-Petersen for bringing in a biological perspective to the work and engaging in the last study on transport in Lofoten and Vesterålen. Kjetil, Stig, Qin, Astrid and Kristine thank you for reading through and giving feedback on the thesis. I would also like give a big thanks the oceanography section at Akvaplan for all help and support with modelling, discussing science and just for being such a fun group to be apart of.

A special thanks goes to all my friends, family and colleagues in Akvaplan for bringing joy, cheering, supporting and keeping me social through this PhD period. I am extremely lucky and privileged to have some many fantastic peoples in my life. None of this would have been possible without you. I would like to thank Helga and Katrine, you are always only a phone call away when I have pressing need for support, air out frustration or just need some proper life wisdom. I would like to thank Ingrid and Linn who made sure I got enough fresh air, exercise, joy, and socialization during the PhD period. To all my fantastic colleagues in Tromsø, in particular, Sanna, Kristine BP and Astrid: thank you for making my workday much brighter by accompanying me for good talks, lunch, coffee breaks and mid-day walks. A special thanks goes also out to the ApN-sporty group, for the extremely hot, extremely cold and extremely social (pre. covid) non-work related activities, forcing me out of the office from time to time. Thank you to my 'home-office mate' Linn who kept me company (and sane) through the restrictions the past year and a half. Eli Anne and Harrison, thank you for providing me a roof over my head, occasional feeding, support, and company after long days at the office. I also want to like thank you my family who has been cheering and supporting me all the way. Last but not least, I want to give a huge thanks to my fellow and good friend Marta. You have been my rock during this PhD. I truly appreciate all the good talks, scientific discussions, your good advises and support through this journey and not at least the friendship that has grown over the course of the PhD-period.

Skare, September 2021
Eli Børve

Contents

Part I

Thesis

Chapter 1

:Introduction

"There is no Phenomenon in Nature that has so much exercised and puzzled the Wits of Philosophers and learned Men as this. Some have thought the Earth and Sea to be a living Creature which, by it's Respiration, caused this ebbing and flowing. Others imagined that it proceeds, and is provoked, from a great Whirl-pool near Norway, which, for fix Hours, absorbs the Water, and afterwards disgorges it in the same space of Time. ... But most Philosophers, who have observed the Harmony that these Tides have with the Moon, have given their Opinion, that they are entirely owing to the Influence of that Luminary. But the Question is, what is this Influence?"

– from ***Geographia generalis*** by Bernardus *Varenius* (1712).

1.1 Motivation

When tidal waves encounter shallow shelves and complex coastlines, the associated currents often dominate the water movement. Particularly through narrow straits and inlets, and over shallow banks, the periodic currents can become prominent (e.g. Moskstraumen in northern Norway and Georges Bank in the gulf of Main; *Gjevik et al.*, 1997; *Hu et al.*, 2008).

The coastal ocean currents are instrumental in defining the marine ecosystems and their associated biodiversity (*Skjoldal et al.*, 2004). Water flow regulates temperature and salinity and provides an important transport medium for substrates, nutrients, plankton, waste and chemical contaminants (e.g. *Blauw et al.*, 2012; *Richardson et al.*, 2000; *Skjoldal et al.*, 2004; *Zhao et al.*, 2019).

The coastal zone, comprising shallow shelf and coastal seas, are characterized by a 3-5 times higher primary production than the deep ocean (*Simpson and Sharples*, 2012; *Zhao et al.*, 2019), and number of studies have shown a substantial co-variability been tides and phytoplankton fluctuations (*Blauw et al.*, 2012; *Otto et al.*, 1990; *Zhao et al.*, 2019). In the North Sea, for example, a prolonged primary production has been linked to periodic enhanced turbulent mixing and upwelling corresponding to the spring-neap tidal cycle (*Richardson et al.*, 2000). The high primary production in tide-dominated coastal regions leads to high abundance of zooplankton, which provides the food source for larger pelagic organisms like larvae and fish.

Not only is the oscillating motion important for vertical mixing and transport of nutrient to the surface layers, but it may also influence the large-scale time-mean circu-

lation in coastal seas (*Parker*, 2007). When strong tidal currents interact with complex topography like steep slopes or narrow straits, they can generate prominent residual circulations and water exchange which are important to the marine environment (*Loder*, 1980; *Wells and van Heijst*, 2003, e.g.). Transport and abundance of pelagic larvae, for example, has been shown to be linked to tidal transport and circulation (e.g. *Loder and Wright*, 1985; *Lough and Manning*, 2001; *Luettich et al.*, 1999; *Townsend and Pettigrew*, 1996).

The coastal zone, containing the bulk of the world's living marine resources, are also highly attractive for human development (*Clark*, 2009). Coastal areas have the most densely populated regions of the world, and the rich marine resources attract industries like fisheries, aquaculture and oil & gas exploration (*Simpson and Sharples*, 2012). Obtaining a healthy and balanced interplay between human industries and marine ecosystems requires an understanding of the risks and impacts involved, which are closely connected to oceanic transport and spreading processes.

The Lofoten and Vesterålen region in Northern Norway is the study site featured in this thesis and a relevant example of a complex marine ecosystem attractive to multiple stakeholders. The region is known for its high biodiversity, excellent fishing grounds and outstanding marine resources. The archipelago is thus a hot spot for the fishing industry but has also seen an increase of aquaculture activity in recent years and oil & gas exploration was considered. While the latter has been prohibited by the government for the regions north and west of the Lofoten archipelago, a nearby area south of Lofoten is open for exploration.

The Lofoten and Vesterålen region hosts spawning grounds for many important fish stocks, amongst them the Northeast Arctic (NEA) cod (*Hjermann et al.*, 2007). NEA cod forms the largest stock of the Atlantic cod (Gadus morhua *Yaragina et al.*, 2011), and it is one of the most important species for Norwegian fisheries (*Oiestad*, 1994). A high percentage of the spawning grounds of the NEA cod (60-70 %) are located in the Lofoten and Vesterålen region, where Vestfjorden is the major spawning area (*Sundby and Bratland*, 1987). From the spawning grounds, about five months of pelagic drift awaits the offspring to reach their nursing ground in the Barents Sea (*Ådlandsvik and Sundby*, 1994). Since both the survival and growth rate during these early life stages of the NEA cod is crucial for the recruitment of the fish stock (*Hjort*, 1914; *Houde*, 2008; *Vikebø et al.*, 2005), knowledge of drift patterns and the underlying ocean dynamics is important for identifying factors controlling the recruitment.

The coastal sea around Lofoten and Vesterålen region is known to be dominated by tidal motion. The tidal wave amplitude in this region is over 1 m and current speed exceeds 2-3 m/s in many of the straits dividing the Lofoten and Vesterålen Archipelago (*Moe et al.*, 2002). Even though many observational and model studies have been conducted to map the transport pattern of the eggs and larvae from Lofoten and Vesterålen to the Barent Sea (e.g. *Opdal et al.*, 2008; *Sundby*, 1978; *Vikebø et al.*, 2007; *Ådlandsvik and Sundby*, 1994), very few (if any) have investigated the influence of tidal dynamics on the large-scale flow pattern, despite the prominent presence of tides in the region.

1.2 Objective

The overarching goal of this thesis is to improve our understanding of the impact and importance of tides for long-term net transport in shallow coastal areas, with a particular focus and application to the Lofoten-Vesterålen region in the northwest of Norway. The periodic tides are always present, and thereby also their nonlinear contribution to the time-mean transport and circulation. In order to understand the impact of tides a high level of knowledge about the nonlinear tidal transport dynamics is required. To achieve the overarching goal, we address following objectives:

- Investigate which tidal transport processes are present and important in the Lofoten and Vesterålen region.
- Investigate the nonlinear dynamics arising from the interaction between barotropic tides and topography leading to prominent time-mean transport in Lofoten and Vesterålen.
- Investigate the relative impact of tidally-induced transport to the total particle transport in Lofoten and Vesterålen, with application to the transport of cod eggs/larvae from Vestfjorden.

Chapter 2

:Background

2.1 Tides in the ocean

2.1.1 Tide-generating forces

The periodic movement of the ocean has, at all times, fascinated people in coastal regions. The constant rising and sinking of the ocean surface has been subject to many creative, yet natural, explanations such as the breathing or the pulse of the Earth (*Varenius*, 1712).

Today, it is well known that this periodic movement is caused by gravitational forces exerted by the Moon, the Sun and the Earth. Even though the coinciding pattern of high and low tide and the position of the Moon was noticed and documented well before the Christian era (*Marmer*, 1922), the phenomenon was not physically explained until Newton's discovery of the law of gravitation (*Principa Mathematica*, 1687) in the late 17th century.

The Earth is subject to tide-generating forces as it moves in a varying gravitational field due to a common attraction with other celestial bodies like the Moon and the Sun (*Barger and Olsson*, 1995). The gravitational attraction between the Earth and the Moon can be expressed by Newton's law of gravity

$$F_g = G\frac{M_e M_l}{R_l^2} \tag{2.1}$$

where, F_g is the gravitational force, G is the universal gravitational constant ($6.67 \times 10^{-11}\mathrm{Nm^2kg^{-2}}$), R_l is the distance between the mass center of Earth and Moon, and M_e and M_l is the masses of Earth and Moon, respectively (*Pugh and Woodworth*, 2014). 2.1 states that force of gravitational attraction between the Earth and the Moon is proportional to the product of their masses and inversely proportional to the square of the separation distance (*Pugh and Woodworth*, 2014). Since the gravitational forces vary with respect to distance to the Moon, a particle at the point on Earth closest to the Moon (A in Fig 2.1) experiences somewhat greater gravitational attraction towards the Moon compared to a particle located at the point farthest away from the Moon (B in Fig 2.1),

$$F_{gA} = G\frac{M_e M_l}{(R_l - r_e)^2} \quad and \quad F_{gB} = G\frac{M_e M_l}{(R_l + r_e)^2} \tag{2.2}$$

where r_e is the radius of the Earth (*Pugh and Woodworth*, 2014).

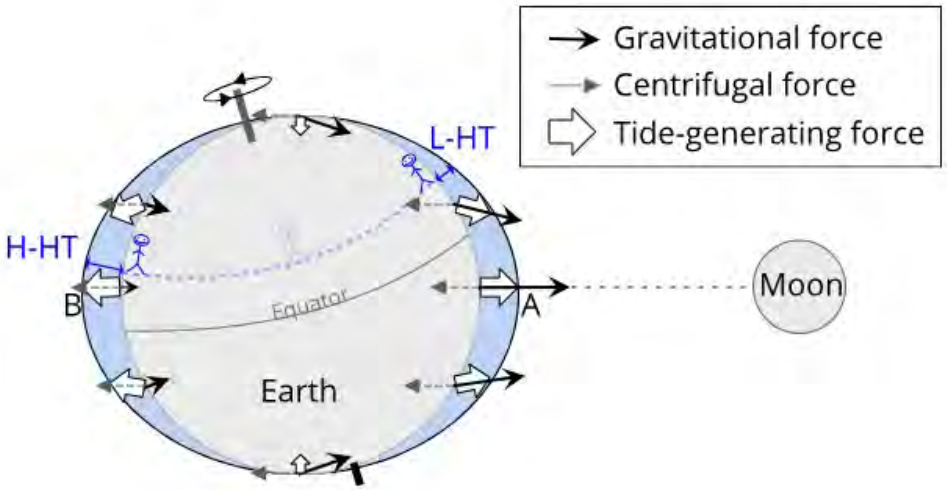

Figure 2.1: *Illustration showing the tide-generating forces at the Earth's surface exerted by the Earth-Moon system (tide-generating force = gravitational force + centrifugal force). The blue man represents an observer on a fix point on Earth. As the Earth rotates one cycle around its own axis, the observer will experience different amplitudes of the high and low tide due to the declination between the equatorial plane and the line intersecting the Earth and the Moon, called the diurnal inequality. At the point closest to the Moon the observer experiences the low high-tide (L-HT) and at the point farthest away from the Moon the observer experiences a high high-tide (H-HT).*

The Earth and Moon also revolve around a common center of mass, which induce an additional force to the system. The Earth encircles this center over the course of one lunar month. In fact, every particle at any point on Earth will conduct this circular motion. Newton's second law states that for a body to accelerate a force must be applied to it. Since all particles on Earth revolve around this common center of mass, they all experience the same acceleration. Thus, the same forcing is needed to perform the revolution. This force, called the centrifugal force (also due to the gravitational attraction between the two celestial bodies) is therefore equally strong everywhere on Earth (Fig. 2.1) (*Pugh and Woodworth*, 2014).

To visualize the effect of the two forces, a water-covered Earth without continents is considered (Fig. 2.1). At the center of mass on Earth the centrifugal force and the gravitational force are equally strong, but oppositely directed. At the point on earth closest to the Moon, however, the gravitational pull is strongest and dominates the centrifugal force (Fig. 2.1). Here, the water piles up under the attraction to the Moon creating a bulge of water. At the point farthest away from the Moon, the gravitational force is weakest and the centrifugal force dominates. Since the centrifugal force is oppositely directed from the gravitational pull, an additional bulge of water is created here, facing away from the Moon (Fig. 2.1) (*Gerkema*, 2019). The sum of the gravitational pull from the Moon and the centrifugal force, is called the *tide-generating forces* (*Gill*, 1982). These forces are responsible for setting the tidal motion in the ocean.

Note that it is the non-uniform gravitational field that gives rise to the tide-generating force, which can also be described in an inertial frame of reference. In an inertial frame of reference the coordinate system is centered on Earth (moving along with the body), instead of a coordinate system outside Earth (watching the body moves), as

described above (*Barger and Olsson*, 1995). Here, a similar example as given in (*Pugh and Woodworth*, 2014) can be used to describe the differential gravitational pull and resulting tidal bulges. Imagining a water balloon falling from a roof top towards the ground. The part of the balloon facing the ground experiences a slightly greater gravitational force compared to the center of the balloon (our reference point). Similarly, the part of the balloon facing the sky, experiences slightly weaker gravitational force from Earth compared to the center of the balloon. Hence the part of the balloon facing the ground/sky accelerates towards ground slightly faster/slower than the center of the balloon . The balloon is thus under strain from the differential gravitational forces, which acts to deform the balloon into an elliptical shape with the major axis in the direction of the gravitational force. In the Earth-Moon system, the deformation is along the Moon-Earth axis (*Barger and Olsson*, 1995; *Pugh and Woodworth*, 2014).

The Sun causes a similar tide-generating force. However, since the gravitational pull is proportional to the mass of the Sun, but inversely proportional to the square of the distance between the Sun and Earth (2.1), the gravitational pull is weaker. While the Moon is responsible for about 65 percent of the tidal motion, the Sun is only contributes about 35 percent (*Gjevik*, 2009).

Since Earth also rotates around its own axis, an observer on a fixed location on Earth will experience a continuously changing sea level with two high waters (tides) a day (Fig. 2.1 (*Parker*, 2007). These tides are called the semi-diurnal tides, representing the principal contributions from the Sun and the Moon (*Gerkema*, 2019). However, unless the Moon is exactly above the equator, the equatorial plane and the line from the Earth to the Moon intersect at an angle (Fig. 2.1). Then the maximum height of one bulge, for example the one facing the Moon, is located south of the equator while maximum height of the other bulge, facing away from the Moon, is located north of the equator. The observer will therefore experience one high high-tide (H-HT) and one low high-tide (L-HT) a day (blue man in Fig. 2.1) (*Parker*, 2007). The difference in the two high tides is called the daily inequality, which sets up the diurnal tides.

Beside the Sun and the Moon moving relative to the Earth, their position also varies relative to each other. Therefore, the combined tidal forcing exerted by the Moon and the Sun on Earth varies in time. About twice a month, at full and new moon, the Moon, Sun and Earth are aligned. At these times, the gravitational forces of the Moon and the Sun pull in the same direction, amplifying each other to generate spring tide. At half-moon, the Earth-Sun line and the Earth-Moon line are perpendicular, and the gravitational forces acts against each other. This is called the neap tide (Fig.2.2) (*Gerkema*, 2019).

The semi-diurnal and diurnal tides are the principal periods of the tide-generating forces acting on the world's oceans (*Gerkema*, 2019). However, due to the elliptical paths of rotation of the astronomic bodies and time-varying declination between the rotational planes, the tidal forcing varies periodically in time. These temporal variations cause modulations of the principal periods (*Parker*, 2007). The net tidal forcing acting on a position on Earth can therefore be expressed as the sum of sinusoidal forcing with different periods and amplitude, which we refer to as tidal constituents (*Gerkema*, 2019).

In total, there are discovered in total few hundreds astronomical tidal constituents, with periods ranging from a few hours to tens of thousands of year (*Gerkema*, 2019). An overview of the most important constituents and their periods is given in Table

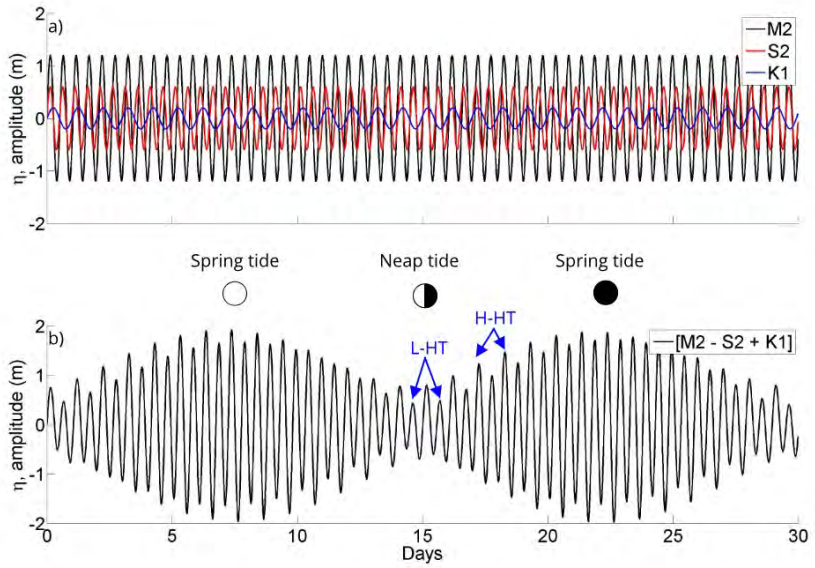

Figure 2.2: *The variations in tidal amplitude for individual tidal constituents a) and for the combination of different tidal constituents in b). The upper panel a) shows two sinusoidal tidal waves with the period of the principle semi-diurnal constituents M2 and S2 and the principle diurnal constituent K1. The lower panel b) shows the combination of the M2 and the S2 tidal wave, [M2–S2], which leads to the spring-neap cycle (period of 14.765 days) and the diurnal inequality K1, which adds the daily variation of high-high tides (H-HT) and low-high tides (L-HT).*

2.1. The spring-neap cycle (Msf) is a modulation of the two principal semi-diurnal oscillations (M_2 - S_2), and therefore not a truly fortnightly oscillation, but a compound tide (Fig. 2.2) (*Gerkema*, 2019). Taking also into consideration varying bathymetry and the presence of continents on Earth, advection and friction will further modulate the tides in the ocean. These tidal modulations are called shallow-water tides (*Gerkema*, 2019).

The tidal motion in the world's ocean is thus much more complex than the simplistic explanation of the tide-generating forces provided above. However, this explanation, commonly called the *equilibrium theory of tides*, provides a useful insight on the dominating forces and the understanding of the main periods of the tidal motion on Earth.

2.1.2 Tidal motion in the ocean

In reality, the movement of the tidal bulges is influenced by the rotation of the Earth, ie. the Coriolis acceleration, and is restricted by the boundaries given by continental coastlines. Tidal waves, which are the ocean response to tidal forcing, often manifest themselves as Kelvin waves, travelling poleward along the eastern boundaries and equatorward along the western boundaries (*Gerkema*, 2019). The structure of a Kelvin wave can be derived from the shallow water equations, where the nonlinear terms in the momentum balance is neglected

$$\frac{\partial u}{\partial t} - fv = -g\frac{\partial \eta}{\partial x} \tag{2.3}$$

Table 2.1: *The main tidal constituents with period and descriptions(Parker, 2007)*

Constituent	Period	Description	Type
M2	12.421 hrs	Principal lunar	Semidiurnal
S2	12.000 hrs	Principal solar	Semidiurnal
N2	12.658 hrs	Principal lunar elliptical	Semidiurnal
K1	23.934 hrs	Declination to Sun/Moon	Diurnal
O1	25.819 hrs	Principal lunar declination	Diurnal
P1	24.066 hrs	Principal solar declination	Diurnal
Mf	13.661 days	Lunisolar fortnightly	Long-period tides
Msf	14.765 days	Lunar synodic fortnightly	Long-period tides
Mm	27.555 days	Lunar monthly	Long-period tides
Ssa	182.621 days	Semiannual solar	Long-period tides

$$\frac{\partial v}{\partial t} + fu = -g\frac{\partial \eta}{\partial y} \tag{2.4}$$

$$\frac{\partial \eta}{\partial t} + H\frac{\partial}{\partial x}(Hu) + H\frac{\partial}{\partial y}(Hv) = 0. \tag{2.5}$$

Here u, v is the depth averaged velocity components, $H = \eta + h$ is the total water depth, η is the time varying sea surface elevation, h is the mean water depth, where as $\eta << h$ and h is uniform in space (flat bottom). g is the gravitational acceleration from Earth and f is the Coriolis frequency (*Gerkema*, 2019). Consider an ocean with a strait coastline in the x direction, and the positive y-direction is directed away from the coast (Fig. 2.3a). By allowing only motion parallel to the coast $(v = 0)$ and assuming the motion can be described by a wave solution

$$\eta = F(y)sin(kx - \omega t), \tag{2.6}$$

a set of equation describing the Kelvin wave properties can be obtained from (2.3)-(2.5), and (2.6),

$$\eta = \eta_0 e^{sgn(k)(f/c)y} sin(kx - \omega t), \quad and \quad u = sgn(k)\eta_0\sqrt{\frac{g}{H}} e^{sgn(k)(f/c)y} sin(kx - \omega t) \tag{2.7}$$

η_0 is amplitude of the Kelvin waves, $c = \sqrt{gH}$ is the phase speed and $\omega = c|k|$ is the dispersion relation of the Kelvin wave (*Gerkema*, 2019). The wave number $k = sgn(k)|k|$ can both be positive and negative. k is negative/positive when the wave propagates in positive/negative x-direction (Fig. 2.3). More details are provided in *Gerkema* (2019). The solution for the Kelvin wave is plotted in Figure 2.3a. From

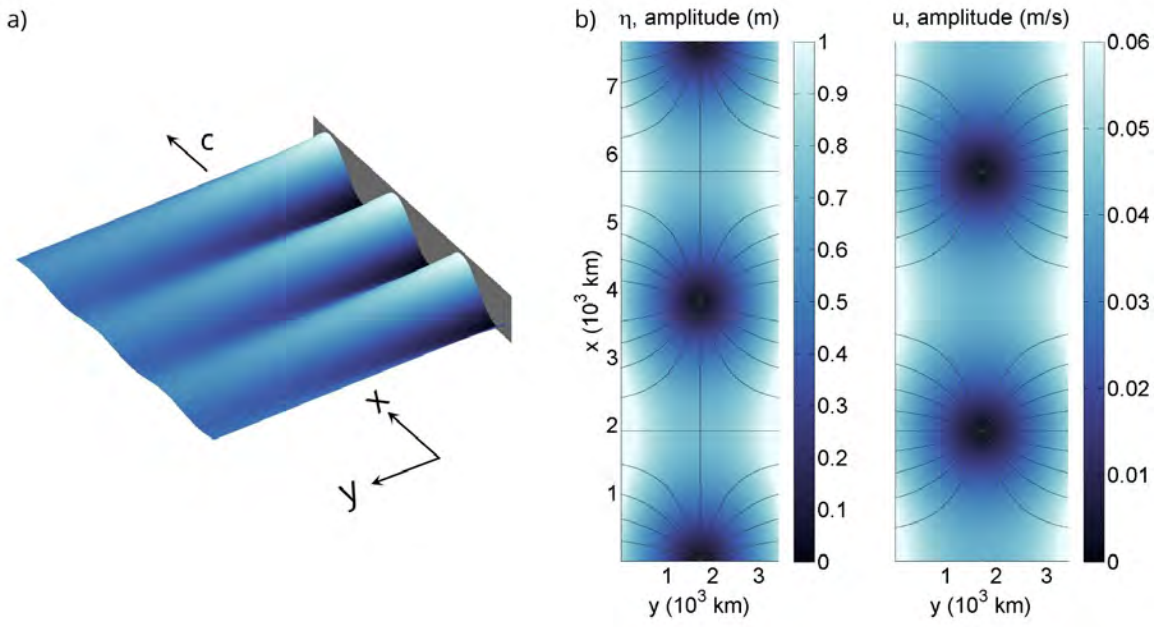

Figure 2.3: *Properties of Kevin waves. a) A propagating Kelvin wave along a coastal boundary on the Northern Hemisphere. b) A combination of a poleward propagating Kelvin wave along the eastern boundary and an equatorward propagating Kelvin wave along the western boundary in an "ocean channel". The colors indicate the amplitude, and the contours in b) show the co-tidal lines. The figures are modified after Figure 5.6 and Figure 5.7 (a and b) in Gerkema (2019)*

(2.7) one can also see that the velocity u and sea surface elevation η are in phase, meaning maximum along-shore velocities and maximum sea surface height occur at the same time.

An ocean basin, such as the North Atlantic, can be simplified into a north-south directed channel with a flat bottom. A poleward propagating Kelvin wave travels along the eastern boundary whilst an equatorward Kelvin wave propagates along the western boundary. The resulting feature of the oppositely directed Kelvin wave pair is shown in Figure 2.3b. The combination of these two waves creates amphidromic points (points with zero amplitude) in the channel, and maximum amplitudes at the coast. Co-phase lines encircles the amphidromic centre points in a cyclonic fashion (in the Northern Hemisphere). Along the coast, the surface elevation and velocity are in phase, behaving like a single Kelvin wave (shown in Fig. 5.7e in *Gerkema*, 2019). In the middle of the basin, the phase shift between the sea surface height and the velocity varies from plus/minus 90 degrees due to the different locations of the corresponding amphidromic points (*Gerkema*, 2019).

While the simplified model in Figure 2.3 illustrates well the main feature of the large-scale behavior of tidal waves in the ocean, their behaviour in the real ocean is much more complex. A realistic ocean basin has neither a flat bottom nor the shape of a rectangular channel. The different ocean basins might be shaped approximately as a channel or a semi-enclosed basin, the topography will vary greatly in space and most continents are companioned with a shallow shelf, which all greatly change the character of the Kelvin waves and the positions of the amphidromic points of the different constituents (*Gerkema*, 2019; *Parker*, 2007).

The presence of a continental slope and shallow shelf, for example, distorts the

Kelvin wave into including cross-slope velocities ($v \neq 0$) (*Gerkema*, 2019). As the water depth decreases on the shelf, the amplitudes both in sea surface height and velocities increases. With decreasing depth, the relative fraction of the water column occupied by the viscous bottom boundary layer increases, meaning that bottom friction has a greater impact on the flow. Hence, in shallow coastal seas, particularly in the presence of complex topography, the linearized shallow water equations(2.3) - (2.5) might not be sufficient to describe tidal motion. The interaction between strong tidal currents and topography generates nonlinear advection and frictional damping, which, unlike the linear terms, leads to compound tides (shallow-water tides) and residual currents influencing the circulation and transports in shallow coastal seas (*Gerkema*, 2019; *Parker*, 2007).

2.2 Tidal transport dynamics in shallow coastal seas

Prominent time-mean transport induced by tides may occur when strong tidal currents interact non-linearly with topography (*Parker*, 2007). The net tidally-induced transport is typically estimated by calculating the mean value over a set of full tidal-cycles. In addition to identifying the magnitude of mean tidal transport, the different underlying processes can be extracted by conducting a Reynolds decomposition of the time-varying transport. For example, the transport of tracer through a cross-section can be written

$$\overline{Q_p} = \overline{Q_v C_p} = \overline{(\overline{A} + A')(\overline{u_n} + u_n')(\overline{c_p} + c_p')}, \tag{2.8}$$

where $Q_v = Au$ is the volume transport, C_p is the concentration of a property or particles in the water transported through the cross-section A, and u_n is the normal velocity into the cross-section. The overline denotes the time-mean value and the prime indicates the time fluctuation.

For simplicity a rectangular cross-section can be considered. Then $\overline{A} = WH$, where W and H is the width and mean water depth of the cross-section, respectively. $A' = W\eta$, where η is the time varying sea surface height of the tidal wave. Hence, the full Reynolds decomposition becomes

$$\overline{Q_p} = \underbrace{\overline{A}\,\overline{c_p}\,\overline{u}}_{\text{I}} + \underbrace{\overline{A}\,\overline{c_p' u'}}_{\text{II}} + \underbrace{\overline{c_p} W \overline{\eta' u'}}_{\text{III}} + \underbrace{\overline{u} W \overline{\eta' c_p'}}_{\text{IV}} + \underbrace{W \overline{\eta' u' c_p'}}_{\text{v}}. \tag{2.9}$$

From (2.9), one sees that the net transport of properties/particles through a constriction can be divided into five different terms, whereas the first three terms (I-III) most easily can be linked to physical processes.

The first term (I) represents a mean transport of properties due to a net volume transport induced by a time-mean current. (I) typically becomes important in regions where strong tidal currents encounter steep topography. The processes, called *tidal rectification*, may generate prominent residual circulation through a nonlinear interaction between the oscillating currents and the topographic slope. The second term (II) represents a net transport of properties arising from a co-variance between the tidal current and the concentration of property/particles in the water. This is called *tidal pumping*. As the name suggests, this process is typically important in regions where the strong oscillating tidal currents are forced through narrow constrictions, such as inlets and

straits, resulting in pump-like exchange of water through the constriction. The current brings different water through the cross-section in one direction, compared the opposite direction. The third term (III) is a net volume transport due to a co-variance between the sea surface height and the tidal current velocities, called the *Stokes transport*. This process is typically present when the tidal wave behaves like a progressive wave, for example through an open channels and along the shelf (as an undisturbed Kelvin wave). The two last terms on the RHS results from a co-variance between the variables η and c_p and between all three variables. In the proceeding, we will look into first three terms on the RHS of (2.9).

2.2.1 I – Tidal rectification

In regions where oscillating tidal currents meets topography, the nonlinear interaction may lead to prominent residual currents (*Parker*, 2007). The process, which we call tidal rectification, results from a cross-slope vorticity flux that is balanced by an along-slope mean flow (*Huthnance*, 1973; *Zimmerman*, 1978).

Mathematically, the relationship between the cross-slope vorticity flux and the residual current can be obtained from the vorticity equation derived from the nonlinear shallow water equations

$$\frac{\partial u}{\partial t} + u\frac{\partial u}{\partial x} + v\frac{\partial u}{\partial y} - fv = g\frac{\partial \eta}{\partial x} - \frac{\tau_b^x}{H} \tag{2.10}$$

$$\frac{\partial v}{\partial t} + u\frac{\partial v}{\partial x} + v\frac{\partial v}{\partial y} + fu = g\frac{\partial \eta}{\partial y} - \frac{\tau_b^y}{H} \tag{2.11}$$

$$\frac{\partial \eta}{\partial t} + \frac{\partial}{\partial x}(uH) + \frac{\partial}{\partial y}(vH) = 0 \tag{2.12}$$

where $\mathbf{u} = (u, v)$ is the depth averaged velocity, η is the time varying sea surface elevation, $H = \eta + h$ is the total water depth, g is the gravitational acceleration τ is kinematic bottom friction and f is the Coriolis frequency (*Zimmerman*, 1978, 1981). Horizontal viscosity and surface stress are neglected. Since the tidal rectification typically occurs on small spatial scales, such as around banks or islands, the Coriolis parameter f can be taken as constant within the area of interest. The vorticity equation is obtained by cross-differentiating (2.10) and (2.11)

$$\frac{\partial \xi}{\partial t} + \nabla \cdot u(f + \xi) = -\nabla \times \left(\frac{\tau_b}{H}\right), \tag{2.13}$$

where, $\xi = \partial v/\partial x - \partial u/\partial x$ is relative vorticity. For simplicity, the bottom friction $(\tau_b^x, \tau_b^y) = R(u, v)$ is assumed linear. The relationship between the vorticity flux and the mean velocity (resulting from bottom friction) can be found by integrating (2.13) over an area enclosed by a depth contour and converting into a line integral by applying Stokes theorem. The time-mean vorticity flux, averaged over one tidal cycle, gives the approximate balance

$$\oint \overline{u\xi} \cdot \hat{n}\, ds = -\frac{1}{H} \oint R\bar{u} \cdot \hat{t}\, ds, \tag{2.14}$$

where $\hat{t}$ and $\hat{n}$ are unit vectors tangential (positive clockwise) and normal (positive outwards) to the contour, respectively, and the overline indicates the time-average (more details can be found in *Paper II*). Since time-varying motion is dominated by the oscillating tidal currents, the time-averaged $\partial/\partial t \oint u \cdot \hat{t}\, ds$ can be assumed negligible when only one or a few tidal cycles are considered. However, if a longer time period is evaluated, say the spring-neap cycle, this term is not necessarily small and cannot be neglected (*Paper II*). (2.14) relates a positive flux of relative vorticity down-slope to an anticyclonic residual current and a negative flux of vorticity down-slope to a cyclonic residual current.

The mechanisms responsible for generating the vorticity flux may be understood by following a water column that is periodically forced up and down a topographic slope by tides (*Zimmerman*, 1978, 1981). The vorticity equation (2.13) can be rewritten into the Lagrangian form assuming rigid lid

$$\frac{D\xi}{Dt} = \underbrace{\frac{\xi + f}{H}\mathbf{u}\cdot\nabla H}_{\text{(i)}} + \underbrace{\frac{R}{H^2}\mathbf{u}\times\nabla H}_{\text{(ii)}} - \underbrace{\frac{R}{H}\xi}_{\text{(iii)}}. \tag{2.15}$$

(*Paper II*; *Zimmerman*, 1978). $D/Dt = \partial/\partial t + \mathbf{u}\cdot\nabla$ is the total rate of change a water parcel experiences both in time and space. (2.15) states that a water parcel may experience change in relative vorticity along its path due to three potential processes given by the terms on the RHS. The two first terms (i) and (ii) represents production of relative vorticity, while the latter term (iii) represents frictional dissipation of relative vorticity.

The first term (i) of the RHS in (2.15) represents a change in relative vorticity due to squeezing and stretching of a water column that forced up and down a topographic slope. This generation process, illustrated in Figure 2.4a and 2.4b, has its origin in conservation of angular momentum. Consider a water column with radius r and height H equal the water depth, that has some weak initial positive spin ($\xi > 0$). When the water column is forced up a topographic slope, H decreases while r increases in order to conserve its volume. If no torque is acting on the water column (like friction or velocity shear) the angular momentum, which is proportional to the initial spin and radius r, is conserved, Therefore, when the radius of the water column increases, the spin decreases in order to conserve the angular momentum.

A classic analogy to this process is an ice skater doing a pirouette. If the ice skater keeps the arms close to the body the pirouette can be performed with an incredible spin. To slow down the motion, the skater may stretch out the arms leading to an increase of radius and decrease of spin.

In oceanography, this relationship is called conservation of potential vorticity, and is valid in absence of friction. In that case (2.15) reduces to

$$\frac{D\xi}{Dt} - \frac{\xi + f}{H}\mathbf{u}\cdot\nabla H = 0, \quad \text{or} \quad \frac{D}{Dt}Q = 0 \tag{2.16}$$

Here $Q = (f + \xi)/H$ is the potential vorticity (*Gill*, 1982). In absence of friction Q is constant. Since f is assumed constant, only the relative vorticity ξ is affected by changing water depths. Hence, when the water column moves into shallow water it will acquire negative vorticity (Fig. 2.4a), and contrary, with a move into deeper water

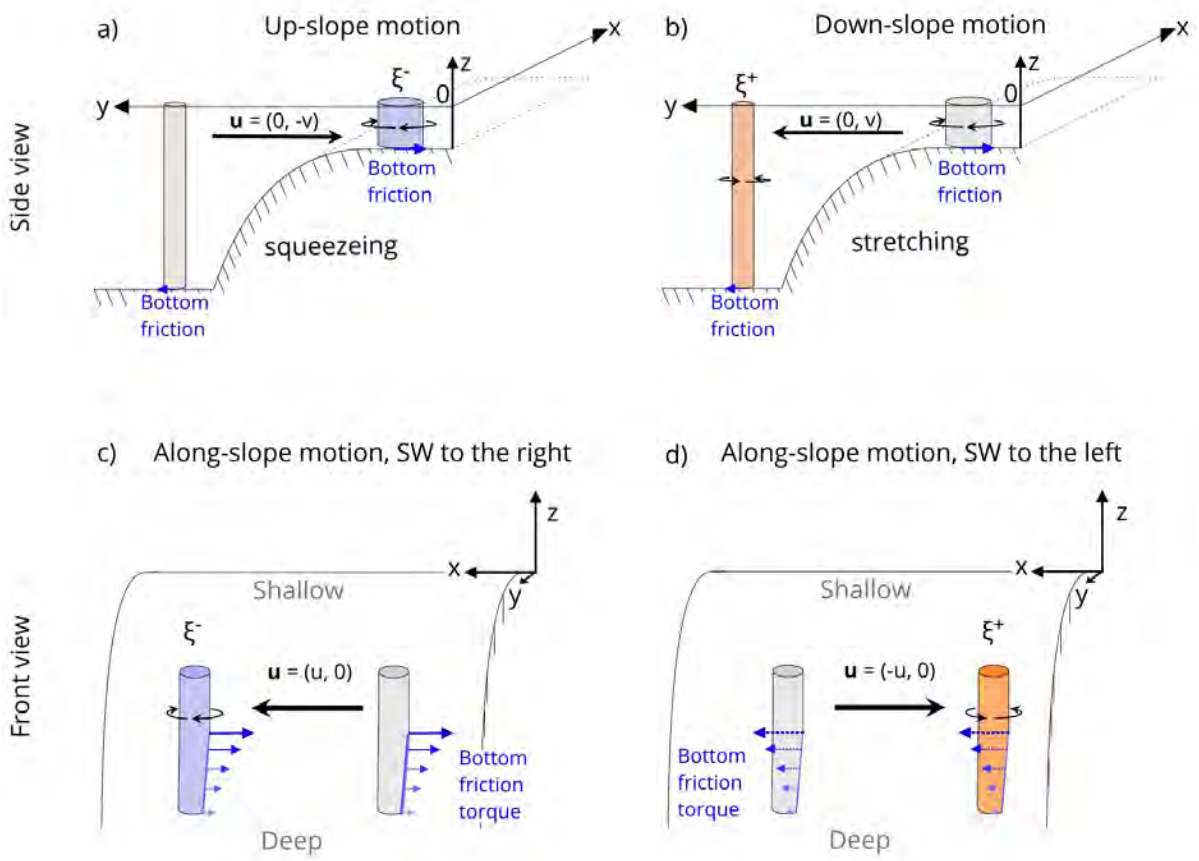

Figure 2.4: *Mechanisms which induce relative vorticity to a water column that is forced across topography in the upper panels a) and b) and to a water column that is forced along the topography in the lower panels c) and d). In a) a water column aquires negative relative vorticity by squeezing when it is forced into shallower water. In b) a water column aquires positive relative vorticity by stretching when it is forced into deeper water. This mechanism (squeezing and stretching) is related to potential vorticity. In c) a water column acquires negative relative vorticity when it moves along-slope with shallow water (SW) to the right due to differential bottom friction induced by the sloping bottom topography under the water column, called the bottom friction torque. In d) a water column acquires positive relative vorticity when it moves along-slope with shallow water to its left due to the bottom friction torque.*

positive vorticity will be gained (Fig. 2.4b). In presence of bottom friction, some relative vorticity is lost to dissipation, and the potential vorticity is no longer fully conserved. However, the frictional loss is much weaker than the effect by squeezing and stretching when the water column forced up and down the slope by tidal motion.

The second term (ii) on the RHS of (2.15), represents a vorticity production term due to a differential bottom friction torque that acts on a water column when it moves along a topographic slope (*Maas et al.*, 1987). A water column moving along-slope will experience somewhat stronger bottom friction on its shallow side compared to its deep side. The deep side of the water column will therefore move slightly faster inducing a negative spin (vorticity) when the water column moves with shallow water to its right (Fig 2.4c). Conversely, if the water column moves with shallow water to its left, the differential bottom friction will induce a positive spin on the water column (Fig. 2.4d).

The third term (iii) om the RHS of (2.15) represents dissipation of relative vortic-

ity by bottom friction. Even though dissipation generally is small, it is instrumental for generating vorticity flux across the depth contours, and thereby inducing a residual circulation (*Paper II; Zimmerman*, 1978). A water column that is forced up and down a topographic slope will typically acquire negative relative vorticity up-slope, and positive relative vorticity down-slope. In the absence of bottom friction, the water column acquires as much negative vorticity up-slope as positive vorticity down-slope, and the net change in relative vorticity after one tidal cycle is zero. With bottom friction present the water column loses some negative vorticity in shallow waters, and some positive vorticity in deeper waters. Over one or more tidal cycles, the water column transports net negative vorticity up-slope and a net positive vorticity down-slope. The vorticity flux, and corresponding rectified current, is sustained by external forcing by the tidal potential.

The angle of the tidal motion on the slope and the resulting responses are displayed in Figure 2.4, where panel (a) shows the different angles of the tidal motion and panels (b)-(d) show the direction of the vorticity flux and residual current based on the vorticity production term and angle of the tidal forcing (in the northern hemisphere). Figure 2.4b. shows the net positive down-slope vorticity flux generated by stretching and squeezing (potential vorticity), which is always balanced by an anti-cyclonic along-slope mean current (in the Northern Hemisphere). Figures 2.4c and 2.4d show the vorticity flux due to the bottom friction torque (ii), which influences the vorticity flux when the tidal current is not rectilinear in the cross-slope direction. When the water column is forced up and down the slope with an along-slope angle, the second term of the RHS (ii) in (2.15) modifies the cross-slope vorticity production by potential vorticity (i). In the case where the tidal current is directed up-slope at an angle with shallow water to the right (Fig. 2.5c), both production terms (i) and (ii), will generate negative vorticity up-slope and positive vorticity down-slope, enforcing the anticyclonic residual current. If the tidal current is directed up-slope at an angle with shallow water to the left, the bottom friction torque will generate positive vorticity up-slope and negative vorticity down-slope. In this case, the bottom friction torque counteracts the vorticity generation due to squeezing and stretching. Depending on which production term is largest, (i) or (ii), the bottom friction torque will act to reduce the anticyclonic residual circulation (i>ii), or reverse the residual current into a cyclonic motion (i<ii, Fig. 2.5d).

2.2.2 II - Tidal pumping

Tidal pumping is an exchange process that occurs through narrow constraints like inlets and straits. The exchange process, which is caused by a temporal asymmetry in the tidal flow field, is associated with a zero net mass flux. The simplest model to explain the tidal pumping was provided by *Stommel and Farmer* (1952), who was the first to investigate this phenomenon. In the model the tidal current enters a strait from all directions, following potential flow lines (Fig.2.6a). The surface area of the volume of water that enters the strait over the course of half a tidal cycle has a shape of a semicircle. This region is typically called the sink region. After half a tidal cycle, the current reverses and flows out of the strait through the same opening. When the tidal current exits the strait, the flow decelerate as the opening widens, forming a local high pressure outside the opening. If the deceleration is rapid enough, the adverse pressure gradient will, together with friction, bring the flow at the coast to a halt and potentially

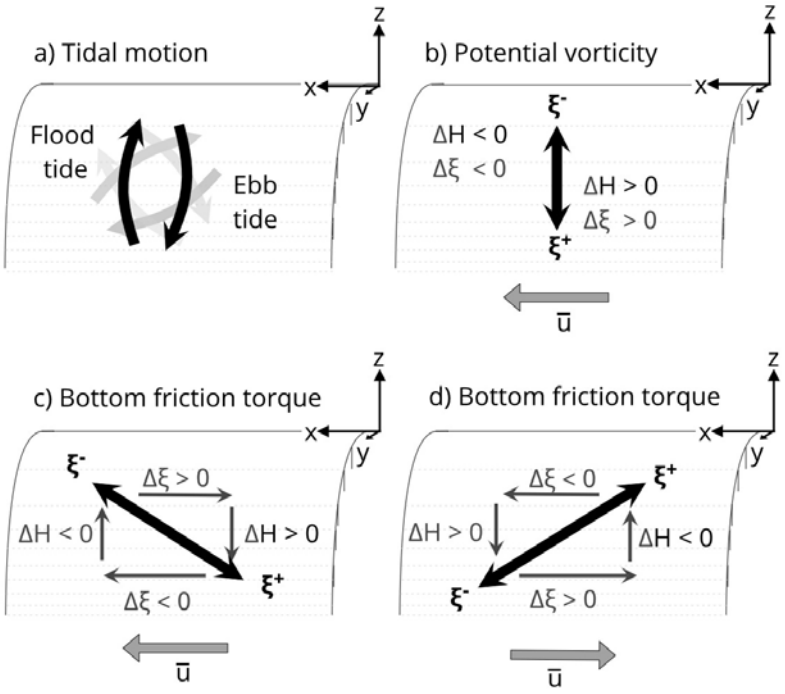

Figure 2.5: *Sketch illustrating the direction of the tidal forcing that may induce a cross-slope vorticity flux in a) and the corresponding direction of vorticity flux and resulting residual circulation induced by the two mechanisms, potential vorticity (squeezeing/stretching) in b) and bottom frictional torque in c) and d). The motion of the water column forced by the tide is indicated by the thick black arrow, while the direction of the residual current $\overline{u}$ is indicated by the gray thick arrow in b), c) and d).*

reverse it, causing flow separation (*Kundu et al.*, 2016). When the flow separates it will continue straight ahead as tidal jet (Fig.2.6b). The water transported by the jet, follows a narrow path, where the bulk of the water is transported out of the sink region. During the subsequent tidal cycle, when the flow re-enters the strait, only the small fraction of the tidal jet inside the sink region will be drawn back into the strait. The water that is located outside the sink region, on the other hand, will be exchanged (Fig. 2.6b).

An analogue to tidal pumping, is respiration (*Wells and van Heijst*, 2003). Humans and animals breathe in the same amount of air as they breathe out. The air we breathe out exits our mouth (or nose) with high speed, like a jet, and is swiftly transported away, while the air we breathe in is extracted from a large volume surrounding the mouth (nose). The air we breathe in therefore contains little of the CO_2 rich air we just exhaled, inhibiting us from suffocation.

More recent studies show that the flow asymmetry is intimately connected to the formation of dipole vortices at the opening of the straits (e.g. *Paper I Afanasyev*, 2006; *Kashiwai*, 1984; *Wells and van Heijst*, 2003). At the point of separation (of the exiting tidal current), a strong velocity front is formed, which immediately rolls-up into a vortex. If the flow separates at both sides of the opening, two vortices of opposite direction are formed at a distance close to the width of the constriction. If the distance is short enough for two vortices to interact, they will form a self-propagating dipole (*Wells and van Heijst*, 2003). The dipole captures most of the water expelled from the construction. Should the dipole escape the return flow, the flow asymmetry and thus the net water exchange will be large (Fig. 2.6b) (*Paper I)*.

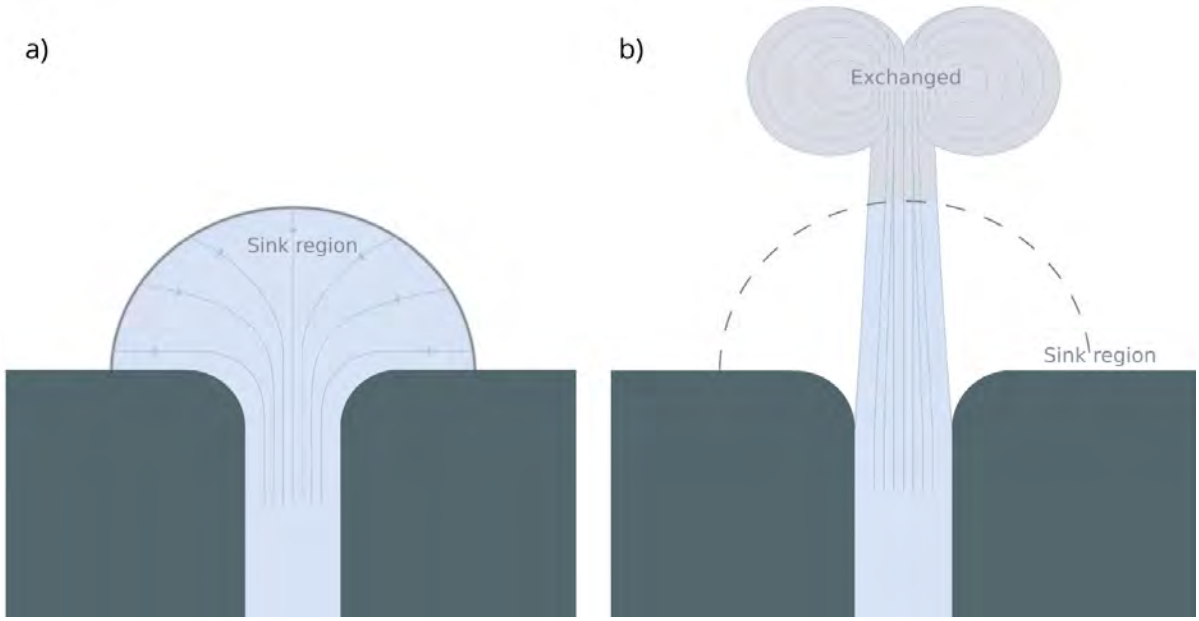

Figure 2.6: *A sketch illustrating flow asymmetry (Fig. 9 in Paper II). a) shows the structure of the tidal current entering the constriction during southward flow (e.g.ebb tide). b) visualises the tidal current forming a jet while exiting the same constriction during northward flow (e.g. flood tide).*

2.2.3 III - Stokes transport

Stokes transport is the third process which may induce a net transport by tides. Stokes transport occurs when the tidal wave acts as a progressive wave (*Guo et al.*, 2014). A progressive wave is characterised by the current velocity and sea surface height being in phase, i.e. maximum velocity and sea surface elevation occur simultaneously (*Gerkema*, 2019). Considering a progressive wave propagating northward through a strait - high tide occurs at the time of maximum current velocity northward and low tide occurs at the time of maximum current velocity southward. When integrating the volume flux through a constriction over one tidal cycle, more water is transported northward than southward (Fig 2.7).

Based on wave properties, the Stokes transport can be expressed as

$$U_s = \frac{1}{2} U \eta cos(\phi), \tag{2.17}$$

where η is the tidal amplitude in sea surface height and U is the tidal current velocity amplitude (*Guo et al.*, 2014). ϕ is the phase shift between the vertical (η) and the horizontal motion of the tides (u). In a progressive wave $\phi = 0$, which leads to a Stokes transport $U_s = U\eta/2$. In a shallow strait, η can be significant relative to the mean depth and Stokes transport may thus be prominent (e.g. *Garel and Óscar Ferreira*, 2013; *Guo et al.*, 2014). Contrarily, a standing wave as typically encountered in semi-enclosed fjord systems, is defined by $\phi = \pi/2$, which results in zero Stokes transport, $U_s = 0$.

2.3 Continental shelf waves with diurnal frequency

Continental shelf waves (CSWs) are vorticity waves propagating along the continental margins (*Gill*, 1982). CSWs, or coastally trapped waves (CTWs) in presence of

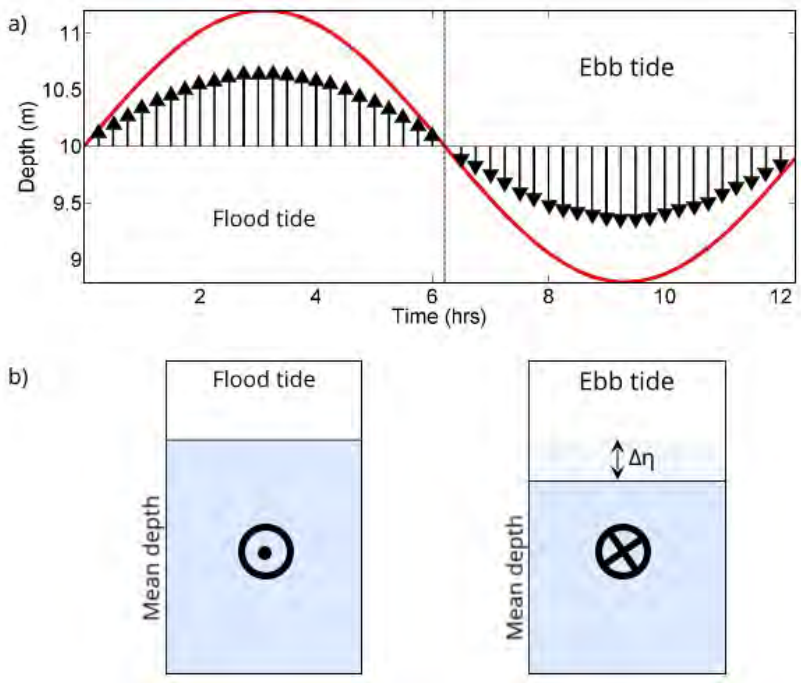

Figure 2.7: *Volume transport by Stokes transport through a strait. a) shows the time variation in water depth (red curve) and the current velocity (black arrows) during one tidal cycle, for a progressive tidal wave. b) shows the corresponding time-mean water depth during flood tide, to the left, and during ebb tide to the right. At flood tide the current is pointed out of the page, corresponding to upward directed arrows in a), and conversely, the currents are pointing into the paper (down in b) during ebb tide. The difference in the time-mean water depth* $\Delta\eta$ *between the two tidal phases (tidal current) leads to a net volume transport through the strait.*

stratification (*Brink*, 1991), are known to set up strong currents and thereby influence the shelf and shelf-slope dynamics (example are given in *Huthnance*, 1995; *Martinsen et al.*, 1979; *Middleton and Bye*, 2007). In particular, the presence of CSWs are intimately connected to cross-slope fluxes (upwelling) (e.g., *Bonaldo et al.*, 2018; *Echevin et al.*, 2014; *Middleton and Bye*, 2007; *Saldías et al.*, 2021). Besides the Stokes drift along the shelf, which is virtually independent of friction, the effect of bottom friction on the CSW field induces a small phase shift that through nonlinearity yields an additional Eulerian mean alongshore velocity (e.g., *Denbo and Allen*, 1983; *Weber and Drivdal*, 2012). Additionally, *Weber and Børve* (2021) (*Paper III*) applies a novel approach to the nonlinear damping problem of CSWs along a permeable coastline. Here we show that wave damping through lateral exchange of water with narrow fjords and straits (which works similar to damping due to bottom friction on the shelf) induces a nonlinear Eulerian mean current. The Lagrangian particle transport induced by CSW damping along the shelf can be obtained from the sum of the Stokes drift and Eulerian mean current.

CSWs are generated by forced oscillatory motion across the steep topography at the transition between the coast/shelf and the deep ocean (*Gill*, 1982). Due to conservation of potential vorticity, these waves are formed and transmitted along the escarpment, with a phase that propagates with shallow water to the right in the Northern Hemisphere (Fig. 2.8) (*Longuet-Higgins*, 1965). When potential vorticity is conserved, $(\xi + f)/H$ is constant (From Eq. 2.16). The direction of propagation can be illustrated by deriving the potential vorticity equation (2.16) from the inviscid shallow water equations; see e.g. *Gill* (1982).

Assuming that f is constant, the relative changes in water depth H are balanced by a corresponding change in ξ. The same dynamics yield here as for the water column moving up and down a topographic slope in (Section 2.2.1), i.e. a water column moving into deeper waters (H increases) acquires positive (cyclonic) relative vorticity, and a water column moving into shallower water acquires negative (anticyclonic) relative vorticity. Due to the direction of rotation (f >0), the displacement always propagates with shallow water to the right in the Northern Hemisphere (Fig. 2.8) (*Huthnance*, 1978).

2.3.1 Generation of CSWs

CSWs are generated through input of relative vorticity in a shelf region (*Adams and Buchwld*, 1969). This vorticity input is typically accomplished by a forcing of water columns across a shelf slope, which will induce relative vorticity as potential vorticity is conserved in the process. The cross-slope motion can be set up by. e.g. sporadic wind events connected to passing weather systems (*Buchwald and Adams*, 1968; *Gill and Schumann*, 1974), or through a more periodic cross-slope motion due to oscillating diurnal tides (e.g., *Cartwright*, 1969; *Lam*, 1999; *Thomson and Crawford*, 1982). The generation of CSWs in both cases is due to a momentum transfer, either by surface stress by wind or bottom stress by tides, through a blocked Ekman transport in presence of a coastline. The blocked Ekman transport leads to cross-slope pressure gradients, which are able to initiate CSWs by vorticity input (*Lam*, 1999). Note that it is the variations in the topography that permits for CSWs to exits, the coastal boundary is only important for the generation mechanism (*Gill*, 1982).

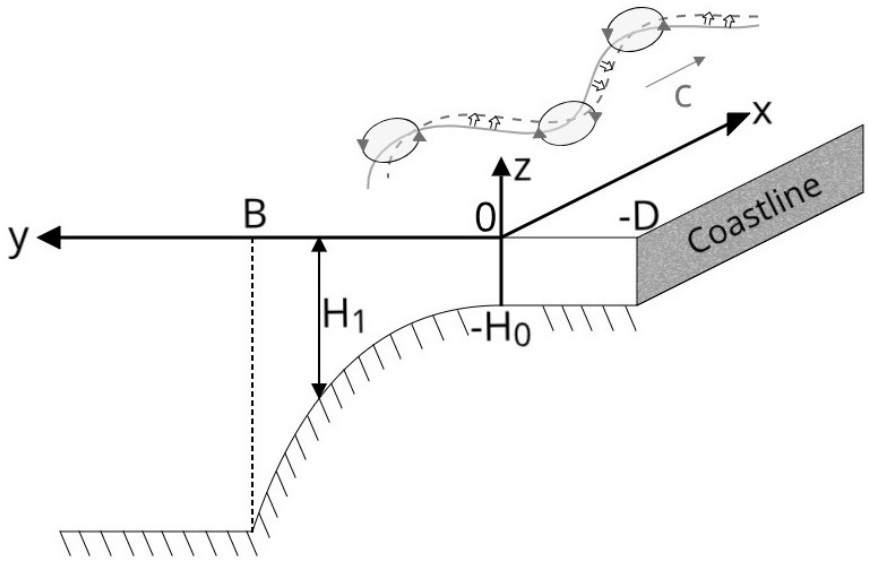

Figure 2.8: *Illustration of the propagation mechanism from continental shelf waves along an exponential shelf slope at the Northern Hemisphere, after Figure 10.18 in Gill (1982). By conservation of potential vorticity will a water column that moves into shallow water acquires negative (anticyclonic) relative vorticity, while a water column that moves into deep water acquires positive (cyclonic) relative vorticity. The resulting motion for a particle in the ocean, indicated by the broad arrows, show a general movement in positive x-direction. The solid line represents the original position of water parcels, wile the dashed line indicates the position after the disturbance has set up the CSW. c is the phase speed of the CSW. The bottom topography is given by (2.18).*

In addition, the oscillating motion through straits has also shown to be an important source of vorticity input for CSW generation, e.g. Bass Strait in Australia (*Middleton*, 1988; *Morrow et al.*, 1990), Hudson Strait connecting to the Laborador shelf (*Middleton and Wright*, 1991) and Juan Fuca Strait in British Columbia (*Flather*, 1988; *Foreman and Thomson*, 1997). Diurnal CSWs observed on the shelf west of Vancouver Island have been shown numerically to be generated from a vorticity flux induced by the strong diurnal currents encountering the abrupt change in topography near the entrance of the Juan Fuca Strait (*Flather*, 1988; *Foreman and Thomson*, 1997). Independent of generation mechanism. the existence of diurnal CSWs is linked to local vanishing of the group velocity caused by the cross shelf-slope variation in topography (*Foreman and Thomson*, 1997; *Lam*, 1999).

2.3.2 Dispersion relation for CSWs

The properties of CSWs depends on the forcing mechanism as well as the shelf-slope topography. The dispersion relation of CSWs can be evaluated analytically along the lines of *Buchwald and Adams* (1968) and *Gill and Schumann* (1974), when the bottom topography is a well-behaved function. In reality, bottom topography is complex, but analytical solutions using a fitted approximation for the topographic slope provides a valuable insight in the CSW properties. A typical function, that has for example shown to fit the continental margin northwest of Norway, is the exponential shelf slope approximation (*Drivdal et al.*, 2016). Here, the water depth H (Fig. 2.8), increases

exponentially away from the coast,

$$H(y) = \begin{cases} H_0 & \text{-W} \leq \text{y} \geq 0 \\ H_0 e^{2by} & 0 \leq \text{y} \geq \text{B} \\ H_0 e^{2bB} & \text{y} \geq \text{B} \end{cases} \tag{2.18}$$

where b is a constant describing the bottom slope, B is the width of the slope region, and W is the width of the inner shelf. The region is bounded by a closed boundary at the coast ($y = -W$), and a flat bottom offshore (y>B).

The shallow water equations (2.3)-(2.5) are used to evaluate the structure of the wave travelling along the shelf break. Since the horizontal scale of the depth variations in this problem is small compared to the Rossby radius $R_o = \sqrt{gH}/f$, the rigid-lid approximation can be applied, and velocities u and v can be expressed in terms of stream functions

$$Hu = -\frac{\partial \psi}{\partial y}, \quad Hv = \frac{\partial \psi}{\partial x}. \tag{2.19}$$

Since the water depth H only varies in y-direction and the nonlinear terms are neglected, the vorticity equation (2.16) is reduced to

$$\frac{\partial \xi}{\partial t} - \frac{f}{H}\frac{\partial H}{\partial y} v = 0. \tag{2.20}$$

A travelling wave solution can be assumed for this problem

$$\psi = H^{1/2}\phi(y)e^{i(kx-\omega t)} \tag{2.21}$$

where k is the along-shore wave number and ω is the wave frequency (*Buchwald and Adams*, 1968; *Gill*, 1982). Inserting (2.19) for u and v in (2.20) gives

$$\frac{\partial}{\partial t}\left[\frac{\partial}{\partial x}\left(\frac{1}{H}\frac{\partial \psi}{\partial x}\right) + \frac{\partial}{\partial y}\left(\frac{1}{H}\frac{\partial \psi}{\partial y}\right)\right] - \frac{1}{H^2}\frac{\partial H}{\partial y}\frac{\partial \psi}{\partial x} = 0. \tag{2.22}$$

Here, an exponential slope with no inner shelf is considered (W = 0), and (2.22) can be solved for ϕ

$$\frac{\partial^2}{\partial y}\phi + (\frac{2kfb}{\omega} - b^2 - k^2)\phi = 0, \tag{2.23}$$

and

$$\phi = C_1 sin(ly) + C_2 cos(ly) \tag{2.24}$$

where,

$$l^2 = \frac{2kfb}{\omega} - b^2 - k^2 \tag{2.25}$$

(2.25) gives the dispersion relation for the CSW.

Typically an impermeable coastline is assumed for the CSW problem, meaning that there is no normal velocity into the coast. This boundary condition $v = 0$ at $y = 0$ is only satisfied for $\phi(0) = 0$, Thus, C_2 must be zero and

$$\phi \propto \sin(ly). \tag{2.26}$$

In the deep ocean ($y \geq B$) the criteria of continuity in pressure (η) and normal fluxes must be satisfied. This second boundary condition implies (from (2.22), (2.19) and $H(B) = H_0 e^{2bB}$), that

$$k\psi + \frac{\partial \psi}{\partial y} = 0, \quad y = B \tag{2.27}$$

(see also *Weber and Drivdal* (2012)). Inserting for $\phi = C_1 sin(ly)$ into (2.27), the transcendental frequency equation

$$tan(lB) = -\frac{l}{b+k} \tag{2.28}$$

is obtained, from which we can determine $l(k)$ (*Buchwald and Adams*, 1968). (2.28) states that there is an infinite number of solutions to the frequency equation, and therefore also an infinite number of modes. However, the wave energy is largest in the first modes (*Huthnance*, 1975). In the case of an exponential shelf with a finite inner shelf, $|W| > 0$ the transcendental frequency equation becomes

$$tan(lB) = \frac{(1+T)l\kappa}{T(b^2+l^2) - \kappa^2 - (1-T)bk} \tag{2.29}$$

where

$$T = tanh(kW) \tag{2.30}$$

(*Lam*, 1999), see *Drivdal et al.* (2016) for details.

Figure 2.9 shows an example of a dispersion diagram where the first three modes are included (values are taken from Transect T1 in *Paper-III*). Here, the highest energy is found in the first (barotropic) mode. Zero group velocity occurs at the maximum value for ω/f, where $c_g = \partial\omega/\partial k = 0$. Hence, at this location the wave energy from the first mode CSWs with diurnal frequencies (close to the K_1 frequency) is trapped (*Buchwald and Adams*, 1968; *Lam*, 1999). This represents a form of resonance for the diurnal frequency in the region (*Lam*, 1999). For the example in Figure 2.9, the resonance occurs for CSWs with frequencies near the diurnal K_1 tidal frequency.

2.4 Ocean circulation around Lofoten and Vesterålen

The Lofoten and Vesterålen region, situated in the northwest of Norway (Fig. 2.10), is used as a geographic study area of this thesis. The region is known for strong tides (*Gjevik*, 2009; *Gjevik et al.*, 1997; *Moe et al.*, 2002) and has complex topography which indicates that tidally-induced transport might be important here. The oceanographic region is bounded by the Norwegian coastline to the east and the deep Norwegian Sea to the west. The continental shelf is split in two by the Lofoten and Vesterålen archipelago. Inside the archipelago the deep and wide Vestfjorden is located. The large embayment reaches depths > 600 m at the head, but is restricted by a 250 m deep sill at the entrance. The shelf west of the Lofoten and Vesterålen archipelago is much shallower with mean depths between 100 and 200 m. South of Lofoten, the shelf is more than 200 km wide, but narrows drastically northward to only about 10 km at the northern tip of Vesterålen.

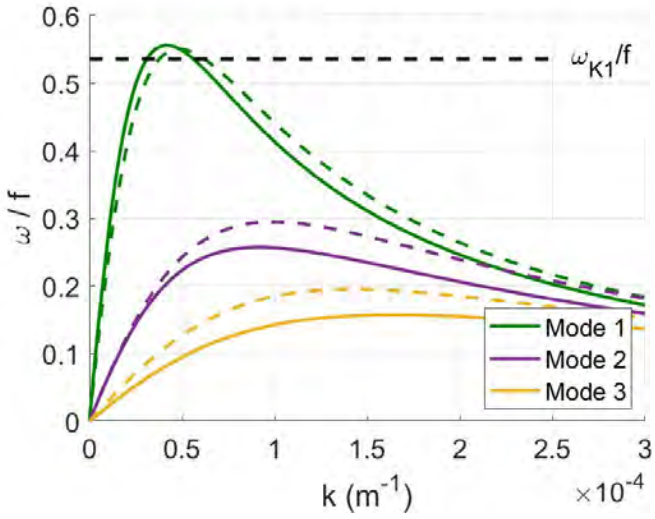

Figure 2.9: *Dispersion diagrams for transect T1 outside Vesterålen, from Paper-III (location and bottom slope are shown in Figure 3 and Figure 4). Solid lines represent an exponential slope with no inner shelf, D = 0, and dashed lines the case of an inner shelf D = 16 km. The horizontal dashed line shows the non-dimensional tidal frequency for the K1 component.*

The general circulation in the Lofoten and Vesterålen region is dominated by two large-scale currents (Fig. 2.10): the Norwegian Coastal Current (NCC) and the Norwegian Atlantic Current (NwAC). The NCC is a wedge-shaped narrow current flowing northeastward along the coastal boundary (*Mork*, 1981). Just north of the Træna trench the NCC bifurcates, where the main branch turns west on to the outer shelf region, while the smaller branch takes a detour via Vestfjorden (Fig. 2.10). The NwAC flows parallel to the NCC, but is located farther offshore at the shelf slope. The two currents have very different properties, NCC contains fresh (and cold) coastal waters, while NwAC contains saline (and warm) Atlantic waters. South of Lofoten the two currents are separated by the shelf. As the shelf narrows towards Vesterålen, the two currents are forced into close vicinity resulting in an energetic region with high rate of baroclinic instabilities and eddy formations (*Isachsen*, 2015; *Koszalka et al.*, 2011).

Field campaigns (e.g. *Mitchelson-Jacob and Sundby*, 2001; *Sundby*, 1978) show that the mean surface circulation in Vestfjorden is largely wind-driven (Fig. 2.11). During northeasterly (NE) winds, the cyclonic circulation inside Vestfjorden is strengthened and the flow along the northwest side out of Vestfjorden is enhanced (Fig. 2.11). At the shelf the NE winds induce an enhanced offshore transport due to a westward Ekman-transport and increased destabilization of the NwAC (*Strand et al.*, 2017). During southwesterly (SW) winds, on the other hand, the surface circulation in Vestfjorden partly reverses, and water exits along the east side (*Mitchelson-Jacob and Sundby*, 2001; *Sundby*, 1978).

In addition to wind forcing, tides highly influence and partly dominates the current variability in Lofoten and Vesterålen. The tidal wave, which arrives from the north Atlantic, between Scotland and Island (*Gjevik*, 2009), propagates northeastward along the coast with increasing amplitude. In the Lofoten and Vesterålen region, Vestfjorden acts as a trap for the tidal wave (*Gjevik et al.*, 1997; *Moe et al.*, 2002) (Fig. 2.12a and b). When entering Vestfjorden, the wave slows down and increases in amplitude due to

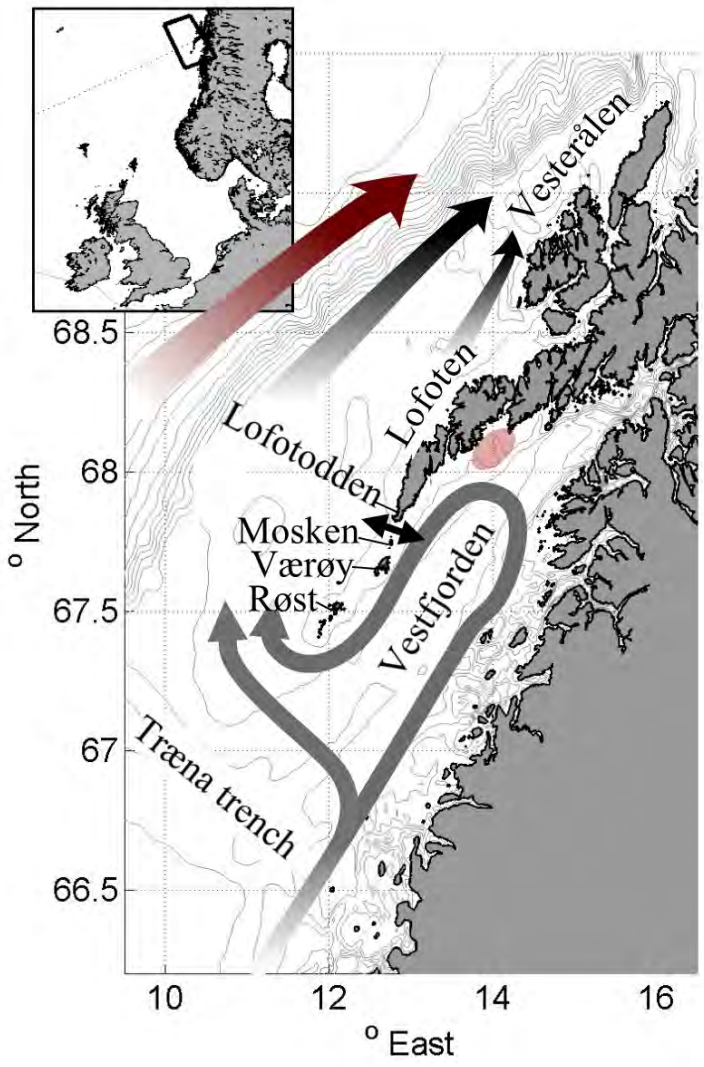

Figure 2.10: *General ocean circulation around Lofoten and Vesterålen. The gray and red arrows illustrate the mean flow pattern of the cold and fresh Norwegian Coastal Current (NCC), and the warmer more saline Norwegian Atlantic Current (NwAC). The thick two-headed arrow is Moskstraumen. The red patch inside Vestfjorden shows the NEA spawning ground Henningsværstraumen. The sketch is from Paper-IV, based on Sætre (1999) and Mitchelson-Jacob Sundby (2001).*

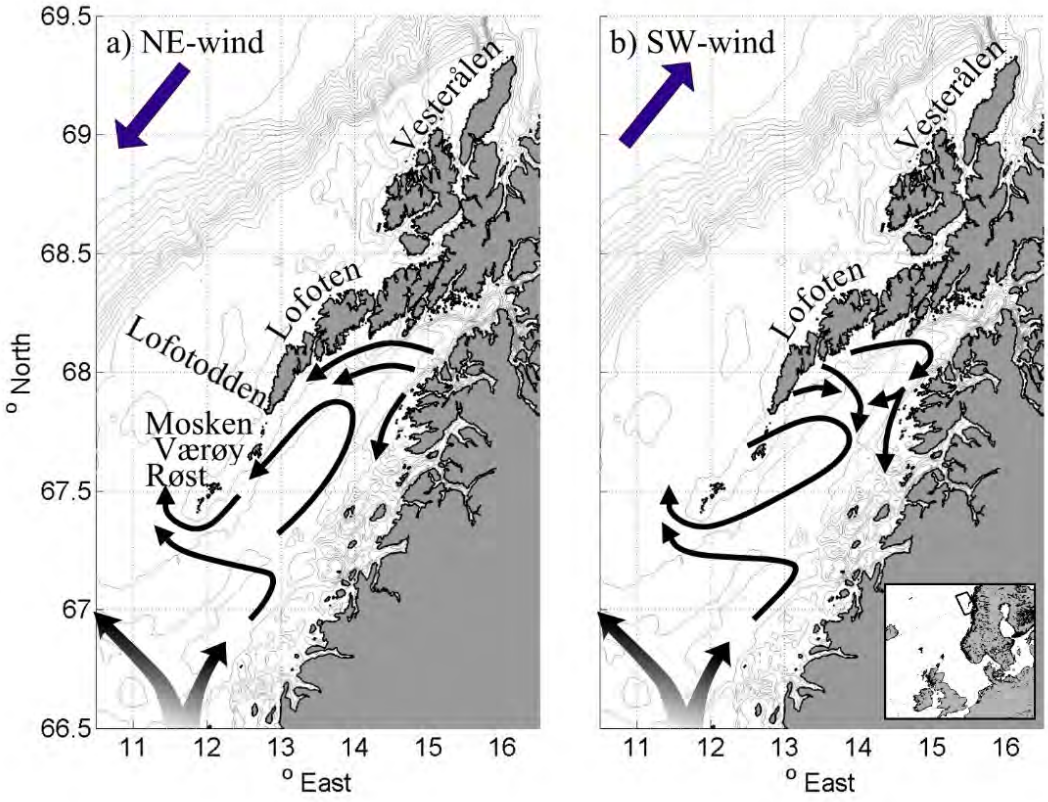

Figure 2.11: *Ocean circulation in Vestfjorden during northeasterly and southwesterly winds in the left (a), and right (b) panels, respectively. The thin black arrows show the mean surface circulation in Vestfjorden during the two wind directions, indicated by the blue arrow in the upper left corner of the figures. After Mitchelson-Jacob and Sundby (2001).*

the geometric constraints of the wide embayment. In contrast, the wave that travels on west of the archipelago speeds up along the narrowing shelf, resulting in a small phase shift and a large gradient in the sea surface height amplitude across the archipelago (Fig. 2.12a and b).

The large gradient in the sea surface height, sets up strong tidal currents in the straits cutting through the archipelago. The current speeds in many of the straits exceeds 2-3 m/s (Fig. 2.12c and d). South of Lofotodden (Fig. 2.10) the well-known tidal current, Moskstraumen, is situated. Moskstraumen, also called the Lofoten Maelstrom, is famous for its vigorous and deadly currents, which are feared by seafarers. Written observations are tracked all the way back to the Medieval ages (references can be found in *Gjevik et al.*, 1997), whereas the first to actually document the relationship between the periodically vigorous maelstrom and the position of the Moon was the famous poet, Peter Dass (*Dass*, 1793).

The K_1 tide show similar behaviour as the M_2 tide, but has a more complex pattern on the shelf. Large variability in the phase of the sea surface height (Fig. 2.12b) and an amplification velocities for the K_1 tide (Fig. 2.12 d) are evident on the shelf west of Vesterålen. The enhanced currents on the shelf, which is not accompanied by a corresponding amplification in sea surface height, is attributed to a formation of diurnal CSWs (*Moe et al.*, 2002; *Ommundsen and Gjevik*, 2000). CSWs are much shorter than the tidal kelvin waves, which explains the large amplification in the horizontal wave field (velocities) while only a small amplification occurs in the vertical (sea surface height) (*Cartwright*, 1969).

The strong tidal currents in the Lofoten and Vesterålen region also set up prominent time-mean residual currents when interacting with topography (Fig. 2.13. These residual currents are closely located to the regions with the highest tidal current amplitudes (in straits, over and around ridges and banks). Particularly evident is the residual circulation around the islands at the southwestern tip of the Lofoten archipelago, around Mosken and Værøy and Røst, and around the banks west of Vesterålen. These residual currents clearly implies that tidally-induced transport may be important in the region.

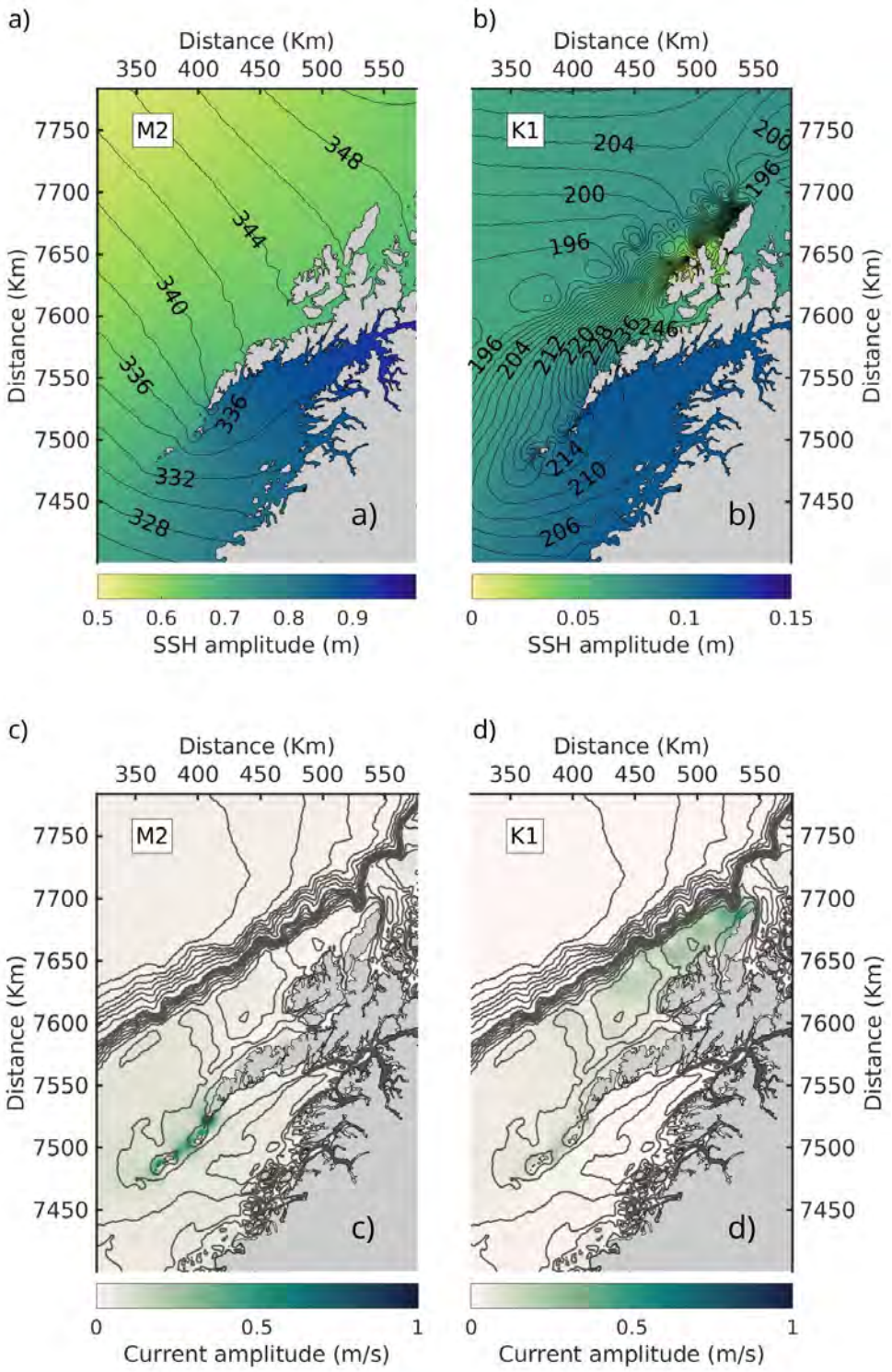

Figure 2.12: *M2 and K1 tides from the model run in Paper II. The upper panels show the amplitude (colors) and phase (contours) of the sea surface height for the M2 tides in a) and K1 tide in b). The lower panels show the tidal currents amplitude (colors) for the M2 tide in c) and K1 tide in d). The contours show the bottom topography.*

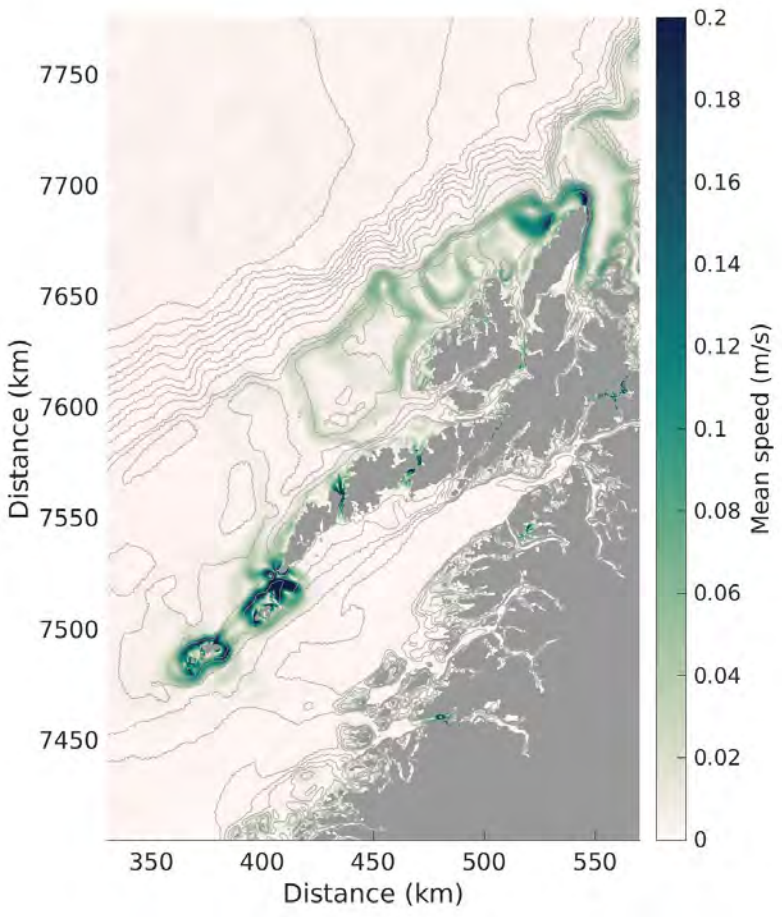

Figure 2.13: *Time-mean residual tidal current, from the 2D-tidal run in Paper II. The colours indicate current speed and the contours show the bottom topography.*

Chapter 3

:Methods and data

The studies conducted in this thesis are mainly based upon numerical modelling. A great challenge within coastal ocean modelling is to resolve small-scale flow dynamics near land and over complex topography while at the same time covering a large spatial domain. Using a structured grid model would require high resolution throughout the whole domain, which would come at an unacceptable computational cost. To overcome this challenge we use an unstructured-grid ocean model, the Finite Volume Community Ocean Model (FVCOM), which allows us to concentrate the fine resolution in specific regions only.

3.1 FVCOM - Unstructured-grid numerical modeling

FVCOM is a prognostic, free-surface, three-dimensional primitive equation ocean model. The model solves the integral form of the governing equations of mass, momentum and tracers over control volumes (Fig. 3.1) (*Chen et al.*, 2003). Here, a control volume is a fictitious volume fixed in space of which the water and particles flow through. The control volume for horizontal velocities is bounded by a triangular grid cell and depth levels (Fig. 3.1c). Each triangular grid cell consists of three edges connected by a node and a centroid in the center (Fig. 3.1b). The horizontal velocities (u,v) are located at the centriods, and computed from a net momentum flux through the surfaces comprising the grid cell. The vertical velocity (w) and scalar variables like temperature (T), salinity (S), and tracer concentrations (c) are located at the nodes. The scalars are calculated from the net flux across the surface surrounding the tracer control volume (Fig. 3.1 b).

The triangular horizontal grid can be refined in areas with complex coastlines and over steep topographic slopes in order to include small-scale dynamics. In the vertical, a terrain-following grid can be applied and the resolution can be refined depending on which depths are of interest (*Chen et al.*, 2003). In *Paper IV*, for example, we use fine resolution near the surface to obtain a realistic wind drag, which decrease rapidly with depth (an example of a vertical grid is shown in Fig. 3.1a).

FVCOM was originally developed for modelling complex coastal regions and estuaries where small-scale dynamics and accurate coastlines are important. The model is well-suited for simulating tidally-driven circulation in coastal regions where strong currents and topographic interactions strongly influence the ocean dynamics. Numerous model studies which applied FVCOM in coastal modelling have shown that the model

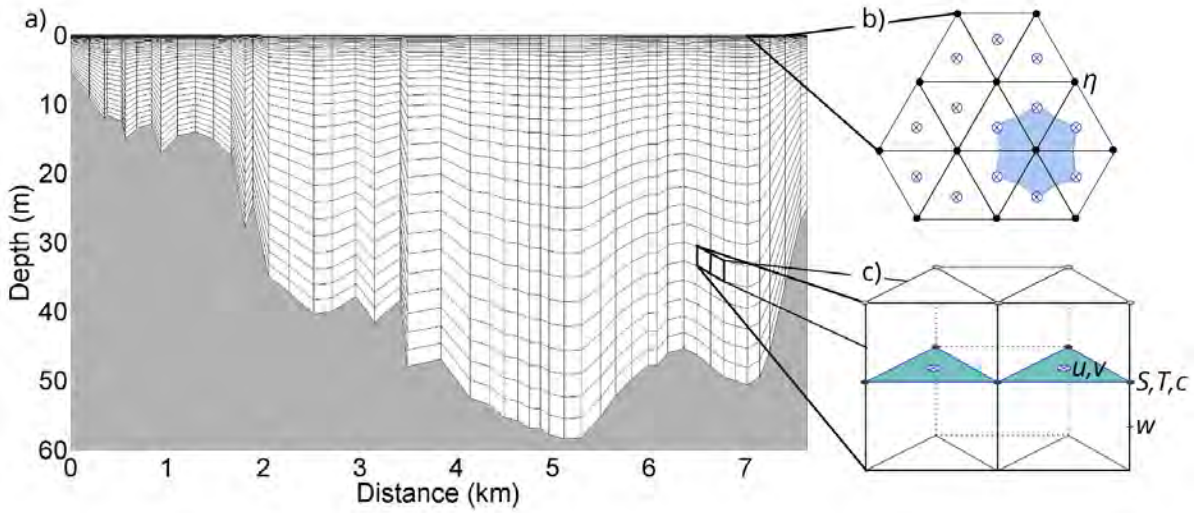

Figure 3.1: *Example of 3D-FVCOM grid. a) displays the vertical grid at a cross-section through Moskstraumen in Lofoten (used in Paper IV). The vertical and horizontal lines mark the boundaries of each grid cell. In total there is 34 vertical layers with increasing resolution towards the surface. b) shows a section of the horizontal grid. Dots represents the nodes and the circles with cross represents the centroids. The blue shaded area shows the control volume around a node. c) shows a section of the vertical slice of two 3D-grid cells. The nodes are located at the corners of the grid cells (marked with grey dots) and contains information about vertical velocity (w), salinity (S), temperature (T), and tracer concentration (c). The sea surface height (η) is also given at the node positions, but only at the surface. The horizontal velocity components (u,v) are located at the cell-center, indicated by the white dot with a blue cross.*

system is robust and works well for this purpose (e.g. *Chen et al.*, 2011; *Sun et al.*, 2016; *Zhao et al.*, 2006, ; more studies can be found at http://fvcom.smast.umassd.edu/fvcom-publications/).

3.1.1 Model set-ups

The simulations conducted in this thesis have all the same basic set-up. The model calculates momentum advection using a second-order accuracy flux scheme (*Chen et al.*, 2013; *Kobayashi et al.*, 1999) and applies a quadratic bottom stress. The vertical eddy diffusion coefficient is calculated using the modified *Mellor and Yamada* (1982) level 2.5 turbulent closure scheme by *Galperin et al.* (1988), while the horizontal diffusion of momentum is calculated using the Smagorinsky closure scheme (*Smagorinsky*, 1963). More details on the model can be found in the manual (*Chen et al.*, 2013).

In total we run four different model simulations in this thesis. In all simulations we use down to 30-50 m resolution at the coast within the focus areas, and relax the resolution away from the coast and towards the boundaries. All straits are resolved with a minimum of five grid cells across the narrowest constriction, whereas the strait openings in general have 10 or more grid cells across the flow direction. In *Paper I* where we simulate idealized tidal straits, the resolution is even higher (15 cells) across the narrowest straits. Such high resolution allows us to model flow separation, development of eddies, and other rectification processes, which are important for generating nonlinear tidal transport.

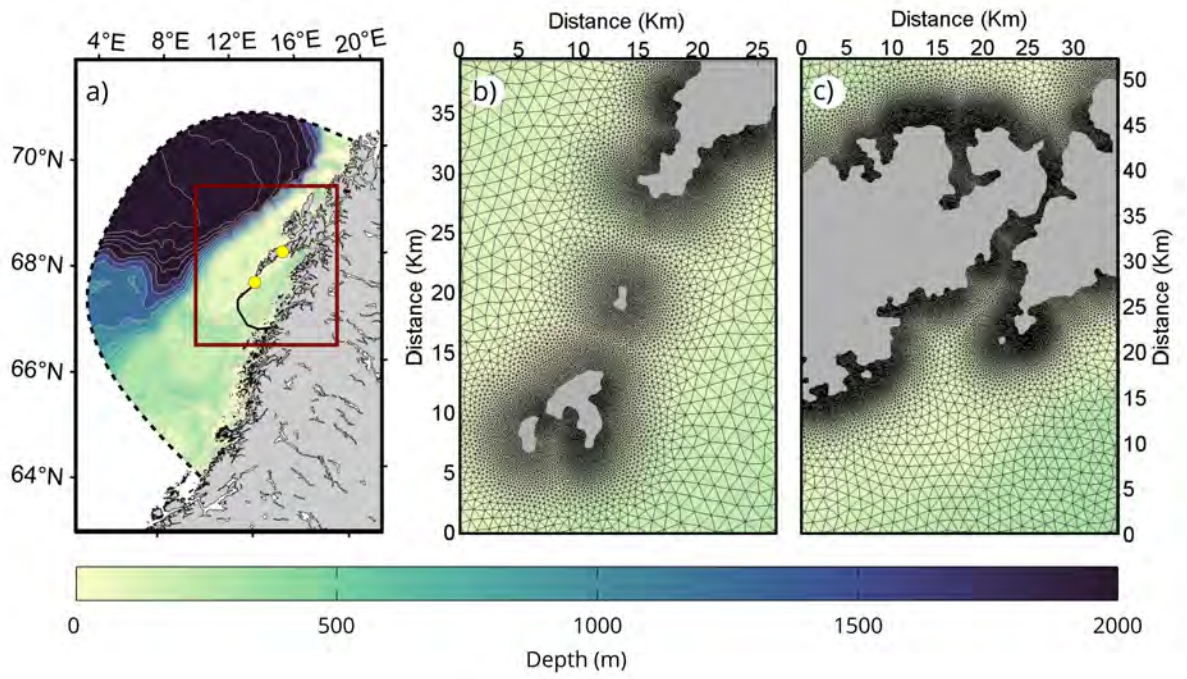

Figure 3.2: *The model domain with topography (colors) for northern Norway is displayed in the left panel (a) (Paper II and Paper IV). The red rectangle indicated the Lofoten and Vesterålen region, whereas the black line indicates the boundary to Vestfjorden. The middle and right panels show the grid resolution in Moskstraumen (b) and Gimsøystraumen (c). The two straits are highlighted on the map in (a) by the the yellow dots. The southern dot shows the location of Moskstraumen and the northern dot shows the location of Gimsøystraumen.*

Regarding the model domain and boundary conditions, various set-ups are applied for the different studies. In the idealized studies (Paper I and Paper II) we use a semi-2D set-up of FVCOM (leaving out any buoyancy effects). We investigate a fully barotropic ocean in both idealized studies, where the temperature, salinity and thereby density have constant values inside the domain. Tidal dynamics are the only focus of these studies, hence we neglect surface stress (winds) and other atmospheric influence (precipitation, radiation, evaporation), and force the two models with variations in the sea surface evaluations along the open boundaries only. In *Paper I* the model is forced by a single northward propagating Kelvin wave with M2 period (12.42 hours). In *Paper II* we use the sea surface elevation extracted from the global assimilated tidal model TPXO 7.2 (*Egbert and Erofeeva*, 2002) for model forcing.

The last study conducted in the thesis (*Paper IV*) include two fully realistic 3D coastal ocean around Lofoten and Vesterålen. The model-set up is similar in the two simulations, where only the ocean forcing is different. In the vertical a terrain-following sigma coordinate system was used, with a total of 34 layers. For realistic response to wind forcing, the vertical resolution is highest near the surface and coarsens with increasing depth (Fig 3.1a). The model was forced with ocean properties like temperature, salinity, 3D current velocities, and sea surface height (SSH) obtained from the NorShelf model. NorShelf is an operational set up of Regional Ocean Modeling System (ROMS) run by MET.no (*Röhrs et al.*, 2018). In one simulation we apply hourly data from Norshelf to include full tidal forcing, while in the other simulation we apply daily mean fields to exclude the main tidal constituents (semi-diurnal and diurnal).

The atmospheric forcing is applied using hourly data fields from the MetCoop model provided by the Norwegian Meteorological Institute (*Müller et al.*, 2017) in both simulations.

3.2 Drift modelling

We couple the hydrodynamic model to drift models to gain a better understanding of the tidal transport dynamics. Here we have two options: an Eulerian tracer model and a Lagrangian particle model. The Eulerian method considers tracers as a continuum and the time evolution is calculated through conservation equations on fixed control volumes, in the same fashion as salinity and temperature in a hydrodynamic model. The Lagrangian method tracks the pathway of individual particles as they are advected by the ocean currents. For concentration and water exchange estimates, an Eulerian model set-up is much more cost efficient than applying the Lagrangian method, which would require an enormous amount of particles for robust concentration estimates (*Zhang and Chen*, 2007). The advantage of the Lagrangian approach, on the other hand, is the ability to track pathways of individual particles, determining transport patterns and dispersion.

In the idealized studies (*Paper I* and *Paper II*) we couple FVCOM to an online Eulerian tracer model, 'Framework for Aquatic Biogeochemical Models' (FABM) (*Bruggeman and Bolding*, 2014). In each simulation we conduct one initial release within a specified area and calculate the outward net transport of tracer. The passive tracer does not affect the dynamics of the flow, but is advected passively with the ocean currents and diluted by diffusion in the hydrodynamical model (*Bruggeman and Bolding*, 2014). We use the Eulerian approach in the idealized studies. Here we investigating the dynamical processes induced by tides, and the passive tracer allows us to calculate how efficient the water exchange by tidal pumping is and to investigate other nonlinear tidal transport dynamics and where they might be of importance.

In the realistic simulations (*Paper IV*) we apply the offline Lagrangian particle drift model, OpenDrift (*Dagestad et al.*, 2018) to simulate the pathways of cod eggs. Within OpenDrift we use the OceanDrift module as it allows for passive advection of particles by the 3D ocean currents only. The particle location at each time step is thus determined by the currents at their previous location. The reason for only consider passive drift is to focus on and quantify the nonlinear tidal transport contribution to the net transport out of Vestfjorden. The Lagrangian approach allows us to investigate the different transport patterns and identify differences in the transport patterns when the nonlinear tidal dynamics are included in the model simulation.

Chapter 4

: Summary of papers

4.1 Paper I: 'Flow separation, dipole formation and water exchange through tidal straits'

Objective

The aim of this study is to understand the processes leading to net water exchange through narrow tidal straits, called tidal pumping.

Summary

Tidal pumping is an important mechanism for water exchange and transport between fjord regions and the shelf seas, as well as along coastlines comprising islands and narrow straits. In this study, we investigate the dynamics leading to net water exchange through idealized tidal straits applying numerical ocean modelling. In total we carried out 164 numerical simulations where we varied the widths and lengths of the straits, as well as the amplitude of the tidal forcing. In all simulations the openings of the strait were formed by a quadrant of a circle with a radius of 2 km. The tidal pumping is closely connected to flow separation at the strait openings and the formation of self-propagating dipoles. We therefore investigate the constraints of the strait geometries on the tidal flow, and the subsequent effect on flow separation and dipole formation. In addition, we use the knowledge obtained from analyzing the processes responsible for net water exchange, to derive a simple kinematic model for effective tracer transport by tidal pumping through narrow straits.

Main findings

- The effective tracer transport by self-propagating dipoles depends on three dimensionless parameters representing strait length, dipole travel distance and dipole size.

- For effective water transport by tidal pumping to occur, the strait length must be shorter than the tidal excursion. In addition, the dipole must fully or partly escape return flow inside the sink region.

- The initial vortices originate from a roll-up of the velocity front resulting from the flow separation. Only when the initial vortices are located close enough to interact do they form a dipole, which immediately starts to self-propagate.
- The propagation speed of the dipole is proportional to the tidal current velocity, and twice the theoretical propagation speed derived for a vortex pair with no background flow.

Main conclusions

Dipole formation is crucial for effective water exchange by tidal pumping through narrow straits. The dipole vortices that originate from the velocity front, which was formed by flow separation, capture and transport water ejected from the strait. When breaking away from the return flow, dipoles are highly effective in causing net water exchange through tidal straits. The understanding of the physical processes creating net water exchange by tidal pumping is necessary to realistically include these processes in the coastal ocean models. Tidal pumping by dipole formation can only be included if flow separation, which occurs on small spatial scales, is resolved in the models.

Author contribution

I carried out all original (50 m) model simulations, except a set of new high-resolution experiments (10 m) for the sensitivity study. I analyzed most of the model output and produced most of the figures, as well as contributing significantly to writing the original manuscript.

4.2 Paper II: 'Rectified tidal transport in Lofoten-Vesterålen, Northern Norway'

Objective

The aim of this study is to investigate whether nonlinear tidal dynamics contribute to net tracer transport out of Vestfjorden, which is located in the Lofoten and Vesterålen region. In addition, the regional importance of tidally-induced transport and in which areas the tidally-induced transport is of importance are explored.

Summary

The Lofoten and Vesterålen region is a highly productive marine area, and an important spawning ground for many fish species. The region is also well known for prominent tidal currents, particularly in the many straits cutting through the archipelago. While the strong tidal currents are well documented and studied, their impact on time-mean transport has attained little attention. In this study, we model a 2D tidally driven coastal sea in northern Norway with a focus on transport out of Vestfjorden, located southeast of the Lofoten and Vesterålen archipelago. To investigate the net transport and the underlying nonlinear dynamical processes, we release passive tracers inside Vestfjorden and analyze the tracer transport over a 2-month period to include the spring-neap cycle.

Main findings

- Two tidally-induced transport processes were responsible for the bulk of the tracer transport out of Vestfjorden: Tidal pumping through the narrow straits, and tidal rectification around the more isolated island groups south of Lofotodden.

- The most prominent net transport was due to tidal pumping through the short, shallow and narrow straits Moskstraumen and Nordlandsflaget. In addition, the longer straits Nappstraumen and Gimsøystraumen had notable net transport out of Vestfjorden.

- Prominent tidal rectification was evident around the two island groups Mosken-Værøy, and Røst. The anti-cyclonic residual currents had flow speeds up to 0.2 m/s, i.e. a value which reflects the magnitude of the background current (NCC) in the region. These rectified tidal currents contributed to a net tracer transport out of Vestfjorden. Particularly evident was the net transport out of Vestfjorden south of Røst.

Main conclusions

The results from this study clearly points to tides as an important contributor to net tracer transport in the Lofoten and Vesterålen region. Tidal pumping through Moskstraumen and Nordlandsflaget was the most effective transport process, and water with high tracer concentrations were transported tens of kilometers westward onto the shelf. The second most important transport out of Vestfjorden occurred south of Røst,

and can be attributed to tracer advection by the rectified tidal currents around the island. The strength of the rectified currents and the effective tidal pumping, particularly Moskstraumen, suggest that these processes are likely to be important also when other transport dynamics are considered (such as wind forcing and background currents).

Author contribution

I carried out the model simulation and analyzed the model output with input from co-authors. I wrote the text with support of my the co-authors.

4.3 Paper III: 'Diurnal continental shelf waves with a permeable coastal boundary: Application to the shelf northwest of Norway'

Objective

The objective of the study is to investigate if tidally-induced CSWs of diurnal frequency can occur on the shelf west of Lofoten and Vesterålen and how diurnal CSWs contribute to Lagrangian transport on a shelf bounded by a permeable coastline.

Summary

Both model studies and observations show a distinct amplification of the diurnal K1 tidal currents on the shelf west of Vesterålen in Northern Norway. This amplification has in previous studies been suggested to originates from the presence of diurnal CSWs. In this study we calculated the dispersion relation for CSWs on the shelf west of Vesterålen to verify the presence of diurnal CSWs in the region. Diurnal CSWs can be generated by diurnal tidal motion across the shelf slope or forced by strong tidal current in straits near the shelf (such as Moskstraumen). The amplification of the diurnal tidal current indicates an accumulation of CSW energy at diurnal frequency in the region, which must be damped either by bottom friction or lateral exchange. The coast of Norway consists of a myriad of fjords, islands and narrow straits, which allows for a water exchange normal to the coastline. In this study, we apply a novel approach to investigate the effect of wave damping on mean particle transport on the shelf through lateral exchange in the presence of a permeable coastline. The lateral water exchange is modeled by applying a Robin condition at the coastline. The damping of the CSWs induces a small phase shift that through nonlinearity results in an Eulerian mean alongshore velocity. We derive the depth averaged Eulerian mean drift by calculating the nonlinear radiation stress components, and calculate the Lagrangian mean drift from Stokes drift and Eulerian mean drift.

Main findings

- CSWs of diurnal frequency can occur west of Vesterålen for a small range of wave numbers centered around zero group velocity.
- Spatial damping of CSWs through lateral dissipation (exchange between shelf/fjords) leads to pronounced Lagrangian drift on the shelf, particularly along the coast.
- The Lagrangian mean drift current is independent of the value of the damping coefficient, however small, but non-zero.

Main conclusions

We find that the formation of CSWs of diurnal frequency is indeed possible for the shelf west of Vesterålen, and suggest that their generation is driven by the strong tidal current in Moskstraumen. The generation mechanism by tidal motion implies a regular formation of diurnal CSWs. The spatial damping of the CSWs by lateral water

exchange through a permeable coastline is shown to induce a nonlinear Eulerian mean current on the shelf. The resulting Lagrangian particle transport, obtained by the sum of the Eulerian mean current and the Stokes drift is pronounced along the coast, which likely will influence the particle transport on the shelf.

Author contribution

In this study I calculated the dispersion relation of for CSWs on the shelf west of Lofoten and Vesterålen, and thereby show theoretically that CSWs of diurnal frequencies can occur on the shelf west of Vesterålen.

4.4 Paper IV: 'Tidal effects on transport and dispersion in the Lofoten and Vesterålen region, northern Norway'

Objective

The objective of this paper is to investigate the relative importance of nonlinear tidal transport dynamics on the mean particle drift in Lofoten and Vesterålen.

Summary

The coastal sea around Lofoten and Vesterålen contains the largest spawning grounds for the NEA cod, an economically highly valuable species. About 60 % of the NEA cod spawns within Vestfjorden, which is connected to the shelf through numerous straits with strong tidal currents. While the ocean dynamics in the Lofoten and Vesterålen region are highly influenced by tides, the tidally-induced transport have gained little attention. In this study, we investigate if the nonlinear tidal dynamics contribute and affect the transport of particles from Henningsværstraumen in Vestfjorden towards the shelf and northwards along the shelf. To understand the relative contribution by tides, we conducted two numerical simulations of the coastal sea around Lofoten and Vesterålen: one including and one excluding tides. In both simulations we released particles continuously near the surface in Henningsværstraumen, simulated the spawning of cod eggs from March till May, and investigated the mean transport patterns during 4 weeks of passive drift.

Main findings

- The particle transport out of Vestfjorden was almost 10 % higher when the diurnal and semidiurnal tides were included in the model simulations, compared to when they were excluded.
- While almost 90 % of the particles followed the NCC around the south side of Røst when tides were excluded, a large fraction took a short-cut through Moskstraumen ($\sim$ 30%) when tidal forcing was included.
- The transport of a larger fraction of particles through Moskstraumen and a minor fraction through Nappstraumen results in a generally faster northward bound transport along the shelf at a path closer to the coastline.
- The particle transport was less sensitive to variable wind forcing when tides were present in the simulation.

Main conclusions

The results in this study clearly highlights the importance of including and resolving the nonlinear tidal dynamics when investigating transport in the Lofoten and Vesterålen region. When tides are included, the net transport of particles out of Vestfjorden increases, and the northward transport route along the shelf is also changed. In the presence of tides, a significant fraction of the particles exits through Moskstraumen

while a small fraction leaves Vestfjorden through Nappstraumen and Gimsøystraumen. The transport routes through the straits provides a faster pathway northward along the coastline on the shelf. Without tides, only a small fraction exits Vestfjorden through the straits, whereas the bulk follows the NCC through the main entrance south of Røst. The latter is a slower route towards the NEA nursing grounds in the Barents Sea.

Author contribution

I designed the study and carried out the hydrodynamical modelling of the coastal sea excluding the main tidal constituents. I conducted the particle drift simulations for both scenarios (with and without tides) and analyzed the results. I also wrote the manuscript with support of my co-authors.

Chapter 5

:Summary and future perspectives

The overarching goal of this thesis is to improve our understanding of the impact and importance of tides for long-term net transport in shallow coastal seas, with a particular focus and application to the Lofoten and Vesterålen region in the northwest of Norway. To achieve this goal, four studies have been undertaken. *Paper I-III* comprise detailed investigations of the nonlinear dynamics arising from an interaction between barotropic tides and topography, leading to time-mean transport in the Lofoten and Vesterålen region. *Paper IV* investigates and quantifies the importance of tides for the particle transport in the Lofoten and Vesterålen region relative to other transport processes.

As stated in Chapter 2.2, we can link the tidally-induced transport to three physical processes: *tidal pumping*, *tidal rectification* and *Stokes drift*. The two first processes are investigated in *Paper I* and *Paper II*. Here we combine high-resolution modelling and simplified theory to investigate and understand the dynamics behind, and the factors controlling tidal pumping and tidal rectification. These two processes dominate the tidally-induced time-mean transport from Vestfjorden to the shelf region west and north of the archipelago. In *Paper III* we find that the amplification of the K1 diurnal tidal currents west of Vesterålen is caused by a formation of diurnal CSWs in the region, and suggest that the strong tidal currents in Moskstraumen is responsible for generating these waves. The CSWs can induce time-mean transport by enhancing the tidal current strength on the shelf, which may lead to enhanced nonlinear tidal dynamics. The direct damping of the CSWs also sets up Eulerian mean currents on the shelf, as shown through simplified theory in *Paper III*. Here we calculated the Stokes drift induced by CSWs and the Eulerian mean currents due to wave damping by lateral exchange of water between the shelf and the inner coastal region (through narrow fjords and straits). The sum of the Stokes drift and the Eulerian mean current gives the Lagrangian particle transport induced by the lateral damping of the CSWs along the shelf.

In *Paper IV* we use the knowledge gained in *Paper I-III* and investigate the relative importance of the tidally-induced transport compared to other transport processes in the Lofoten and Vesterålen region. The results from *Paper IV* clearly highlight the importance of including nonlinear tidal dynamics when modelling transport and circulation in the coastal sea of this region. The tidal pumping through Moskstraumen, in particular, provides an important pathway out of Vestfjorden, which also influences the progress of particle drift northward along the shelf. The tidal rectification around the island groups Mosken-Værøy and Røst, which were highly important for tracer transport in the 2D simulation (Fig. 12 in *Paper II*), is also evident in the 3D run when we

plot the difference in flow patterns between the simulations with and without tides (Fig. 6 in *Paper IV*). However, while we clearly see a prominent transport around the south and west side of Værøy in *Paper IV*, it is difficult to extract the relative importance of tidal rectification south of Røst in the presence of the NCC.

While the studies conducted in this thesis highlight the significance of tides for time-mean transport in the Lofoten and Vesterålen region, the findings imply a general importance of nonlinear tidal dynamics for transport and circulation in areas where strong tidal currents interact with complex topography. In the following two sections, a discussion of future perspectives regarding tides and transport in the Lofoten and Vesterålen region, and nonlinear tidal dynamics in general coastal ocean modelling, is presented.

5.1 Tides, transport and the ecosystem in Lofoten and Vesterålen

As discussed above, the results from the studies comprising this thesis show that nonlinear tidal dynamics are important for transport and dispersion of particles in the Lofoten and Vesterålen region. While we used NEA cod eggs and larvae as examples in the thesis, nonlinear tidal dynamics are likely also important also for transporting other marine organisms, nutrients, pollution, and contaminants etc. in this region. However, there is a need for observational data to verify and validate the presence and importance of the nonlinear tidal dynamics in Lofoten and Vesterålen. In this regard, the results in *Paper II* and *Paper IV* can be used to identify locations for in-situ measurements and release point for drifters to increase the likelihood of capturing the nonlinear tidal dynamics in the region.

Focusing on the influence of tidally-induced transport of NEA cod eggs and larvae, we simulated the passive drift of particles to exclude other factors that might generate differences between the net particle drift with and without out tides (*Paper IV*). A natural continuation of this work would be to investigate the impact of tides applying realistic egg and larva properties using an individual-based model (IBM), where egg buoyancy and vertical migration of larvea are also included. Additionally, wind-induced surface gravity waves have been shown to influence the egg-drift in Vestfjorden by *Röhrs et al.* (2014). Their results showed that the Stokes drift tend to move particles closer to land, which potentially increases the importance of tidal pumping through the straits. Hence, to model egg and larvae drift in Lofoten and Vesterålen, both egg and larvae properties in combination with Stokes drift from wind-induced surface gravity waves should be included in future Lagrangian particle model efforts.

The thesis mainly focuses on tidally-induced transport through the straits and over the shallow ridge extending from the archipelago connecting Vestfjorden to the shelf region. However, the amplification of the diurnal tidal currents by diurnal CSWs on the shelf west of Vesterålen implies that the tidal motion might be important for the ocean transport dynamics on the shelf as well. The influence of diurnal CSWs on the shelf circulation and cross-slope transport, has not previously been investigated for this region, and should be pursued further with observations and realistic ocean simulations.

In addition to being an important spawning grounds for many economically important fish stocks, such as the NEA cod, the Norwegian spring-spawning herring, and the NEA haddock, the Lofoten and Vesterålen region is also home to sensitive ben-

thic habitats, large seabird colonies and populations of marine mammals (*Misund and Olsen*, 2013). The presence of CSWs is connected to cross-slope motion, bringing up nutrient rich water from the deeper ocean to the shelf region (*Echevin et al.*, 2014). Additionally, the amplified tidal currents on shelf regions may also generate rectified tidal currents when interacting with topographic features, like banks and troughs. Both upwelling and rectification processes have implications on the marine environment of shelf regions (*Huthnance*, 1995). On Georges Bank, for example, tidal rectification is shown to greatly influence marine productivity by on-bank transport and along bank advection of nutrients and larvae (*Hu et al.*, 2008; *Townsend et al.*, 2006).

Time-mean residual anticyclonic circulation cells have been observed around the shallow banks west and north of Lofoten and Vesterålen. This process has been shown to influence the larvae drift northward towards the Barents Sea (*Bjørke and Sundby*, 1987; *Sundby*, 1984). This topographically steered circulation has not previously been linked to tidal rectification. However, the amplified oscillating currents evident in *Paper II* (see also *Moe et al.*, 2002), have the potential to create rectified tidal currents around banks, which is evident in the 2D-tidal simulations used in *PaperII* (Fig. 2.13). An in-depth study of tidal rectification around the banks in the Lofoten and Vesterålen region using a full 3D-circulation in a stratified coastal ocean could provide valuable insights ecosystem dynamics in the area.

Furthermore, in *Paper III* we hypothesise that diurnal CSWs west of Vesterålen are generated by the strong tidal current of Moskstraumen. The geographic and dynamics setting is similar to the shelf west of Vancouver Island (*Foreman and Thomson*, 1997). Here, *Foreman and Thomson* (1997) show that diurnal CSWs are generated due to strong tidal currents of the Juan de Fuca Strait, which induce a vorticity flux on to the shelf when the current encounter the abrupt topography near the entrance of the strait. The shelf west of Vancouver Island is divided up by deep submarine canyons. A number of studies have indicated that these can periodically be upwelling canyons at times when the wind forcing is strong enough to reverse the slope current (*Connolly and Hickey*, 2014; *Hickey*, 1997). However, a recent study by *Saldías et al.* (2021) shows that propagation of reoccurring CSWs over a submarine canyon can cause upwelling, independent of wind forcing. Similarly, the shelf west of Vesterålen also consists of several deep canyons which are hypothesized to be important upwelling areas for the transport of nutrients from depth on to the shelf. However, the mechanisms behind the upwelling dynamics are not yet fully understood.

A continuation of the work in *Paper III*, extending the investigation into the stratified ocean could provide valuable knowledge on the role of diurnal CSWs on upwelling west of Vesterålen. Such study might bring in an important piece of the puzzle explaining the unique waters around Lofoten and Vesterålen with its impressive diverse ecosystem.

5.2 Non-linear tidal transport dynamics in coastal ocean modelling

While most numerical models today include tidal forcing, the resolution is not always sufficient to resolve the nonlinear tidal dynamics near shore and over steep topography.

As shown in this thesis, a high resolution will allow to integrate a detailed coastline and bathymetry and thus allow for a realistic simulation of transport and circulation patterns. This is in particular of importance in regions where tidal pumping and rectification is likely to be present.

In *Paper I* we evaluated the influence of grid resolution on tidal pumping. For the idealised strait we found that in areas where flow separation occurred a 50 m grid resolution was sufficient to model dipole formation. We performed a grid sensitivity test and found that increasing the grid resolution further to 10 m did not make a significant change in the transport properties of the strait. We conclude that as long as the dynamical processes leading to flow separation and vortex formation is resolved, the tidal pumping by dipole formation is likely to be sufficiently represented. Furthermore, *Vouriot et al.* (2018) show that a resolution on the order of 15 grid-cells across a channel opening is sufficient to provide reasonable eddy-generation and dissipation. However, these numbers are obtained through idealized set-ups, and should also be tested in the presence of realistic bathymetry and coastlines.

The propagation speed and evolution of the vortices in numerical simulations are also highly influenced by the representation of bottom friction and bathymetry in the models (*Hutschenreuter et al.*, 2019; *Vouriot et al.*, 2018). Bottom friction plays an important role in dipole formation and generation of tidal rectification. An investigation of the influence of realistic bottom roughness and corresponding drag coefficients in coastal seas would thus be highly valuable to improve coastal ocean models, particularly in relation to the small-scale shallow-water transport dynamics.

As already mentioned in Chapter 5.1 for the model studies in Lofoten and Vesterålen, there is a general need for more observational studies with the focus on tidally-induced transport properties (particularly of tidal pumping) to enhance our understanding and to verify the presence and strength of these processes in coastal ocean models.

Bibliography

Adams, J. K., and V. T. Buchwld (1969), The generation of continental shelf waves, *Journal of Fluid Mechanics*, *35*, 815–826, doi:10.1017/S0022112069001455. 2.3.1

Afanasyev, Y. D. (2006), Formation of vortex dipoles, *Physics of Fluids*, *18*(037103), doi:10.1063/1.2182006. 2.2.2

Barger, V., and M. Olsson (1995), *Classical mechanics: a modern perspective*, International series in pure and applied physics, 2nd ed. ed., McGraw-Hill, New York. 2.1.1, 2.1.1

Bjørke, H., and S. Sundby (1987), Distribution and abundance indices of postlarval and 0-group cod, in *The effect of oceanographic conditions ondistribution and population dynamics of commercial fish stocks in the Barent Sea.*, Proceedings of the third Sovlet-Norwegian Symposium 26-78 May 1986. 5.1

Blauw, A. N., E. Beninca, R. W. P. M. Laane, N. Greenwood, and J. Huisman (2012), Dancing with the tides: fluctuations of coastal phytoplankton orchestrated by different oscillatory modes of the tidal cycle, *PLoS One*, *7*(11), doi:10.1371/journal.pone.0049319. 1.1

Bonaldo, D., M. Orlić, and S. Carniel (2018), Framing continental shelf waves in the southern adriatic sea, a further flushing factor beyond dense water cascading, *Scientific reports*, *8*(1), 1–11, doi:10.1038/s41598-017-18853-2. 2.3

Brink, K. H. (1991), Coastal-trapped waves and wind-driven currents over the continental shelf, *Annual Review of Fluid Mechanics*, *23*(1), 389–412, doi:10.1146/annurev.fl.23.010191.002133. 2.3

Bruggeman, J., and K. Bolding (2014), A general framework for aquatic biogeochemical models, *Environmental Modelling & Software*, *61*, 249–265, doi:10.1016/j.envsoft.2014.04.002. 3.2

Buchwald, V. T., and J. K. Adams (1968), The propagation of continental shelf waves, *Proceedings of the Royal Society of London*, *305*(1481), 235–250. 2.3.1, 2.3.2, 2.3.2, 2.3.2, 2.3.2

Cartwright, D. E. (1969), Extraordinary tidal currents near st kilda, *Nature*, *223*, 928–932, doi:https://doi.org/10.1038/223928a0. 2.3.1, 2.4

Chen, C., H. Liu, and R. C. Beardsley (2003), An unstructured grid, finite-volume, three-dimensional, primitive equations ocean model: Application to coastal ocean

and estuaries, *Journal of Atmospheric and Oceanic Technology*, *20*(1), 159–186, doi:10.1175/1520-0426(2003)020<0159:AUGFVT>2.0.CO;2. 3.1

Chen, C., H. Huang, R. C. Beardsley, Q. Xu, R. Limeburner, G. W. Cowles, Y. Sun, J. Qi, and H. Lin (2011), Tidal dynamics in the gulf of maine and new england shelf: An application of fvcom, *Journal of Geophysical Research: Oceans*, *116*(C12010), doi:10.1029/2011JC007054. 3.1

Chen, C., R. C. Beardsley, G. Cowles, J. Qi, Z. Lai, G. Gao, D. Stuebe, H. Liu, Q. Xu, P. Xue, J. Ge, S. Hu, R. Ji, R. Tian, H. Huang, L. Wu, H. Lin, Y. Sun, and L. Zhao (2013), *An Unstructured Grid, Finite-Volume Coastal Ocean Model: FVCOM User Manual, version 3.1.6*, Marine Ecosystem Dynamics Modeling Laboratory, 4 ed. 3.1.1

Clark, J. R. (2009), *Coastal seas: the conservation challenge*, John Wiley & Sons. 1.1

Connolly, T. P., and B. M. Hickey (2014), Regional impact of submarine canyons during seasonal upwelling, *Journal of Geophysical Research: Oceans*, *119*(2), 953–975, doi:10.1002/2013JC009452. 5.1

Dagestad, K.-F., J. Röhrs, Ø. Breivik, and B. Ådlandsvik (2018), Opendrift v1. 0: a generic framework for trajectory modelling, *Geoscientific Model Development*, *11*(4), 1405–1420, doi:10.5194/gmd-11-1405-2018. 3.2

Dass, P. (1793), *The trumpet of Nordland*. 2.4

Denbo, D. W., and J. S. Allen (1983), Mean flow generation on a continental margin by periodic wind forcing, *Journal of Physical Oceanography*, *13*(1), 78–92, doi:10.1175/1520-0485(1983)013<0078:MFGOAC>2.0.CO;2. 2.3

Drivdal, M., J. E. H. Weber, and J. B. Debernard (2016), Dispersion relation for continental shelf waves when the shallow shelf part has an arbitrary width: Application to the shelf west of norway, *Journal of Physical Oceanography*, *46*, 537–549, doi:10.1175/JPO-D-15-0023.1. 2.3.2, 2.3.2

Echevin, V., A. Albert, M. Lévy, M. Graco, O. Aumont, A. Piétri, and G. Garric (2014), Intraseasonal variability of nearshore productivity in the northern humboldt current system: The role of coastal trapped waves, *Continental Shelf Research*, *73*, 14–30, doi:https://doi.org/10.1016/j.csr.2013.11.015. 2.3, 5.1

Egbert, G. D., and S. Y. Erofeeva (2002), Efficient inverse modeling of barotropic ocean tides, *Journal of Atmospheric and Oceanic Technology*, *19*(2), 183–204, doi:10.1175/1520-0426(2002)019<0183:EIMOBO>2.0.CO;2. 3.1.1

Flather, R. A. (1988), A numerical model investigation of tides and diurnal-period continental shelf waves along vancouver island, *Journal of Physical Oceanography*, *18*, 115–139, doi:10.1175/1520-0485(1988)018<0115:ANMIOT>2.0.CO;2. 2.3.1

Foreman, M. G. G., and R. E. Thomson (1997), Three-dimensional model simulations of tides and buoyancy currents along the west coast of vancouver island, *Journal of Physical Oceanography*, *27*, 1300–1325, doi:10.1175/1520-0485(1997)027<1300:TDMSOT>2.0.CO;2. 2.3.1, 5.1

Galperin, B., L. H. Kantha, S. Hassid, and A. Rosati (1988), A quasi-equilibrium turbulent energy model for geophysical flows, *Journal of the atmospheric sciences*, *45*(1). 3.1.1

Garel, E., and Óscar Ferreira (2013), Fortnightly changes in water transport direction across the mouth of a narrow estuary, *Estuaries and Coasts*, *36*(2), 286–299, doi: 10.2307/23484933. 2.2.3

Gerkema, T. (2019), *An introduction to tides*, Cambridge University Press. 2.1.1, 2.1.1, 2.1.2, 2.1.2, 2.1.2, 2.3, 2.1.2, 2.2.3

Gill, A. E. (1982), *Atmosphere-Ocean Dynamics*, vol. 30, Academic Press. 2.1.1, 2.2.1, 2.3, 2.3.1, 2.8, 2.3.2

Gill, A. E., and E. H. Schumann (1974), The generation of long shelf waves by the wind, *Journal of Physical Oceanography*, *4*, 83–90, doi:10.1175/1520-0485(1974)004<0083:TGOLSW>2.0.CO;2. 2.3.1, 2.3.2

Gjevik, B. (2009), *Flo og fjære langs kysten av Norge og Svalbard*, Farleia. 2.1.1, 2.4, 2.4

Gjevik, B., H. Moe, and A. Ommundsen (1997), Sources of the maelstrom, *Nature*, *388*, 837–838, doi:10.1038/42159. 1.1, 2.4, 2.4

Guo, L., M. Van der Wegen, J. A. Roelvink, and Q. He (2014), The role of river flow and tidal asymmetry on 1-d estuarine morphodynamics, *Journal of Geophysical Research: Earth Surface*, *119*(11), 2315–2334, doi:10.1002/2014JF003110. 2.2.3, 2.2.3

Hickey, B. M. (1997), The response of a steep-sided, narrow canyon to time-variable wind forcing, *Journal of Physical Oceanography*, *27*(5), 697–726, doi:10.1175/1520-0485(1997)027<0697:TROASS>2.0.CO;2. 5.1

Hjermann, D. O., A. Melsom, G. E. Dingsør, J. M. Durant, A. M. Eikeset, L. P. Røed, G. Ottersen, G. Storvik, and N. C. Stenseth (2007), Fish and oil in the lofoten–barents sea system: synoptic review of the effect of oil spills on fish populations, *Marine Ecology Progress Series*, *339*, 283–299, doi:10.3354/meps339283. 1.1

Hjort, J. (1914), Fluctuations in the great fisheries of northern europe viewed in the light of biological research, *Conseil Permanent International Pour L'Exploration De La Mer*. 1.1

Houde, E. D. (2008), Emerging from hjort's shadow, *Journal of Northwest Atlantic Fishery Science*, *41*, 53–70, doi:10.2960/J.v41.m634. 1.1

Hu, S., D. W. Townsend, C. Chen, G. Cowles, R. C. Beardsley, R. Ji, and R. W. Houghton (2008), Tidal pumping and nutrient fluxes on georges bank: a process-oriented modeling study, *Journal of Marine Systems*, *74*(1-2), 528–544, doi:10.1016/j.jmarsys.2008.04.007. 1.1, 5.1

Huthnance, J. M. (1973), Tidal current asymmetries over the norfolk sandbanks, *Estuarine and Coastal Marine Science*, *1*(1), 89–99, doi:10.1016/0302-3524(73)90061-3. 2.2.1

Huthnance, J. M. (1975), On trapped waves over a continental shelf, *Journal of Fluid Mechanics*, *69*(4), 689–704, doi:10.1017/S0022112075001632. 2.3.2

Huthnance, J. M. (1978), On coastal trapped waves: Analysis and numerical calculation by inverse iteration, *Journal of Physical Oceanography*, *8*(1), 74 – 92, doi:10.1175/1520-0485(1978)008<0074:OCTWAA>2.0.CO;2. 2.3

Huthnance, J. M. (1995), Circulation, exchange and water masses at the ocean margin: the role of physical processes at the shelf edge, *Progress in Oceanography*, *35*, 353–431, doi:10.1016/0079-6611(95)80003-C. 2.3, 5.1

Hutschenreuter, K. L., B. R. Hodges, and S. A. Socolofsky (2019), Simulation of laboratory experiments for vortex dynamics at shallow tidal inlets using the fine resolution environmental hydrodynamics (frehd) model, *Environmental Fluid Mechanics*, *19*, 1185–1216, doi:10.1007/s10652-019-09668-y. 5.2

Isachsen, P. E. (2015), Baroclinic instability and the mesoscale eddy field around the lofoten basin, *JGR Oceans*, *120*, 2884–2903, doi:10.1002/2014JC010448. 2.4

Kashiwai, M. (1984), Tidal residual circulation produced by a tidal vortex. part 1. life-history of a tidal vortex, *Journal of the Oceanographical Society of Japan*, *40*, 279–294, doi:10.1007/BF02302521. 2.2.2

Kobayashi, M. H., J. M. Pereira, and J. C. Pereira (1999), A conservative finite-volume second-order-accurate projection method on hybrid unstructured grids, *Journal of Computational Physics*, *150*(1), 40–75, doi:10.1006/jcph.1998.6163. 3.1.1

Koszalka, I., J. H. LaCasce, M. Andersson, K. A. Orvik, and C. Mauritzen (2011), Surface circulation in the nordic seas from clustered drifters, *Deep Sea Research Part I: Oceanographic Research Papers*, *58*(4), 468–485, doi:10.1016/j.dsr.2011.01.007. 2.4

Kundu, P. K., I. M. Cohen, and G. Dowling, David R. Tryggvason (2016), *Fluid Mechanics*, sixth ed., Academic Press. 2.2.2

Lam, F.-P. A. (1999), Shelf waves with diurnal tidal frequency at the greenland shelf edge, *Deep Sea Research Part I: Oceanographic Research Papers*, *46*, 895–923, doi:10.1016/S0967-0637(98)00090-9. 2.3.1, 2.3.2

Loder, J. W. (1980), Topographic rectification of tidal currents on the sides of georges bank, *Journal of Physical Oceanography*, *10*(9), 1399–1416, doi:10.1175/1520-0485(1980)010<1399:TROTCO>2.0.CO;2. 1.1

Loder, J. W., and D. G. Wright (1985), Tidal rectification and frontal circulation on the sides of georges bank, *Journal of Marine Research*, *43*(3), 581–604, doi:10.1357/002224085788440367. 1.1

Longuet-Higgins, M. S. (1965), Planetary waves on a rotating sphere. ii, *Proc. R. Soc. Lond. A*, *284*, 40–68, doi:10.1098/rspa.1965.0051. 2.3

Lough, R. G., and J. P. Manning (2001), Tidal-front entrainment and retention of fish larvae on the southern flank of georges bank, *Deep Sea Research Part II: Topical Studies in Oceanography*, *48*(1), 631–644, doi:0.1016/S0967-0645(00)00130-2. 1.1

Luettich, R. A., J. L. Hench, C. W. Fulcher, F. E. Werner, B. O. Blanton, and J. H. Churchill (1999), Barotopic tidal and wind-driven larvae transport in the vicinity of a barrier island inlet, *Fisheries Oceanography*, *8*(2), 190–209. 1.1

Maas, L., J. T. F. Zimmerman, and N. M. Temme (1987), On the exact shape of the horizontal profile of a topographically rectified tidal flow, *Geophysical & Astrophysical Fluid Dynamics*, *38*(2), 105–129, doi:10.1080/03091928708210107. 2.2.1

Marmer, H. A. (1922), The problems of the tide, *The Scientific Monthly*, *14*(3), 209–222, doi:10.2307/6374. 2.1.1

Martinsen, E. A., B. Gjevik, and L. P. Röed (1979), A numerical model for long barotropic waves and strom surges along the western coast of norway, *Journal of Physical Oceanography*, *9*, 1126–1138. 2.3

Mellor, G. L., and T. Yamada (1982), Development of a turbulence closure model for geophysical fluid problems, *Reviews of Geophysics*, *20*(4), 851–875, doi:10.1029/RG020i004p00851. 3.1.1

Middleton, J. F. (1988), Long shelf waves generated by a coastal flux, *Journal of Geophysical Research: Oceans*, *93*, 10,724–10,730, doi:10.1029/JC093iC09p10724. 2.3.1

Middleton, J. F., and J. A. T. Bye (2007), A review of the shelf-slope circulation along australia's southern shelves: Cape leeuwin to portland, *Progress in Oceanography*, *75*, 1–41, doi:10.1016/j.pocean.2007.07.001. 2.3

Middleton, J. F., and D. G. Wright (1991), Coastal-trapped waves on the labrador shelf, *Journal of Geophysical Research: Oceans*, *96*(C2), 2599–2617, doi:10.1029/90JC02129. 2.3.1

Misund, O. A., and E. Olsen (2013), Lofoten–vesterålen: for cod and cod fisheries, but not for oil?, *ICES Journal of Marine Science*, *70*(4), 722–725, doi:10.1093/icesjms/fst086. 5.1

Mitchelson-Jacob, G., and S. Sundby (2001), Eddies of vestfjorden, norway, *Continental Shelf Research*, *21*(16-17), 1901–1918, doi:10.1016/S0278-4343(01)00030-9. 2.4, 2.11

Moe, H., A. Ommundsen, and B. Gjevik (2002), A high resolution tidal model for the area around the lofoten islands, norhern norway, *Continental Shelf Research*, *22*, 485–504. 1.1, 2.4, 2.4, 5.1

Mork, M. (1981), Experiments with theoretical models of the norwegian coastal current, in *The Norwegian Coastal Current*, vol. 2, edited by R. Sætre and M. M., pp. 518–530, University of Bergen. 2.4

Morrow, R. A., I. S. F. Jones, R. L. Smith, and P. J. Stabeno (1990), Bass strait forcing of coastal trapped waves: Ace revisited, *Journal of Physical Oceanography*, *20*, 1528–1538, doi:10.1175/1520-0485(1990)020<1528:BSFOCT>2.0.CO;2. 2.3.1

Müller, M., M. Homleid, K.-I. Ivarsson, M. A. Køltzow, M. Lindskog, K. H. Midtbø, U. Andrae, T. Aspelien, L. Berggren, D. Bjørge, P. Dahlgren, J. Kristiansen, R. Randriamampianina, M. Ridal, and O. Vignes (2017), Arome-metcoop: A nordic convective-scale operational weather prediction model, *Weather and Forecasting*, *32*(2), 609–627, doi:10.1175/WAF-D-16-0099.1. 3.1.1

Oiestad, V. (1994), Historic changes in cod stocks and cod fisheries: Northeast arctic cod, in *ICES Marine Science Symposia*, vol. 198, pp. 17–30, Copenhagen, Denmark: International Council for the Exploration of the Sea, 1991-. 1.1

Ommundsen, A., and B. Gjevik (2000), Scattering of tidal kelvin waves along shelves which vary in their lengthwise direction, *Preprint series. Mechanics and Applied Mathematics*. 2.4

Opdal, A. F., F. B. Vikebø, and Ø. Fiksen (2008), Relationships between spawning ground identity, latitude and early life thermal exposure in northeast arctic cod, *Journal of Northwest Atlantic Fishery Science*, *41*, 13–22, doi:10.2960/J.v41.m621. 1.1

Otto, L., J. T. F. Zimmerman, G. K. Furnes, M. Mork, R. Saetre, and G. Becker (1990), Review of the physical oceanography of the north sea, *Netherlands Journal of Sea Research*, *26*(2), 161–238, doi:https://doi.org/10.1016/0077-7579(90)90091-T. 1.1

Parker, B. B. (2007), *Tidal Analysis and Prediction*, NOAA Special Publication NOS CO-OPS 3. 1.1, 2.1.1, 2.1, 2.1.2, 2.2, 2.2.1

Pugh, D., and P. Woodworth (2014), *Tidal forces*, chap. 3, pp. 36–59, Cambridge University Press, doi:10.1017/CBO9781139235778.006. 2.1.1, 2.1.1, 2.1.1

Richardson, K., A. Visser, and F. B. Pedersen (2000), Subsurface phytoplankton blooms fuel pelagic production in the north sea, *Journal of Plankton Research*, *22*(9), 1663–1671, doi:10.1093/plankt/22.9.1663. 1.1

Röhrs, J., K. H. Christensen, F. Vikebø, S. Sundby, Ø. Sætra, and G. Broström (2014), Wave-induced transport and vertical mixing of pelagic eggs and larvae, *Limnology and oceanography*, *59*(4), 1213–1227, doi:10.4319/lo.2014.59.4.1213. 5.1

Röhrs, J., A. K. Sperrevik, and K. H. Christensen (2018), Norshelf: A reanalysis and data-assimilative forecast modelfor the norwegian shelf sea, *Tech. Rep. ISSN 2387-4201 04/2018*, Norwegian Meteorological Institute, doi:10.5281/zenodo.2384124. 3.1.1

Saldías, G. S., K. Ramos-Musalem, and S. E. Allen (2021), Circulation and upwelling induced by coastal trapped waves over a submarine canyon in an idealized eastern boundary margin, *Geophysical Research Letters*, *48*, doi:10.1029/2021GL093548. 2.3, 5.1

Simpson, J. H., and J. Sharples (2012), *Introduction to the Physical and Biological Oceanography of Shelf Seas*, Cambridge University Press, doi:10.1017/CBO9781139034098. 1.1

Skjoldal, H. R., R. Sætre, A. Færnö, O. A. Misund, and I. e. Røttingen (2004), *The Norwegian Sea Ecosystem*, Tapir Academic Press. 1.1

Smagorinsky, J. (1963), General circulation experiments with the primitive equations: I. the basic experiment, *Monthly weather review*, *91*(3), 99–164, doi:10.1175/1520-0493(1963)091<0099:GCEWTP>2.3.CO;2. 3.1.1

Stommel, H., and H. G. Farmer (1952), On the nature of eustarine circulation. part i (chapters 3 and 4), *techreport 52–88*, Woods Hole Oceanographic Institution MA. 2.2.2

Strand, K. O., S. Sundby, J. Albretsen, and F. B. Vikebø (2017), The northeast greenland shelf as a potential habitat for the northeast arctic cod, *Frontiers in Marine Science*, *4*, 304, doi:10.3389/fmars.2017.00304. 2.4

Sun, Y., C. Chen, R. C. Beardsley, D. Ullman, B. Butman, and H. Lin (2016), Surface circulation in block island sound and adjacent coastal and shelf regions: A fvcom-codar comparison, *Progress in Oceanography*, *143*, 26–45, doi:https://doi.org/10.1016/j.pocean.2016.02.005. 3.1

Sundby, S. (1978), In/out-flow of coastal water in vestfjorden, ICES. 1.1, 2.4

Sundby, S. (1984), Influence of bottom topography on the circulation at the continental shelf off northern norway., *FiskDir. Skr. Ser. HavUnders*, *17*, 501–519. 5.1

Sundby, S., and P. Bratland (1987), Spatial distribution and production of eggs from north-east arctic cod at the coast of northern norway 1983–1985, *Report series Fisken og Havet.*, *1*. 1.1

Thomson, R. E., and W. R. Crawford (1982), The generation of diurnal period shelf waves by tidal currents, *Journal of Physical Oceanography*, *12*, 635–643, doi:10.1175/1520-0485(1982)012<0635:TGODPS>2.0.CO;2. 2.3.1

Townsend, D. W., and N. R. Pettigrew (1996), The role of frontal currents in larval fish transport on georges bank, *Deep Sea Research Part II: Topical Studies in Oceanography*, *43*(7), 1773–1792, doi:10.1016/S0967-0645(96)00040-9. 1.1

Townsend, D. W., A. C. Thomas, L. M. Mayer, M. A. Thomas, and J. A. Quinlan (2006), *Oceanography of the northwest Atlantic continental shelf (1, W)*, vol. 14A, pp. 119–168, Harvard University Press. 5.1

Varenius, B. (1712), *Geographia generalis*. 1, 2.1.1

Vikebø, F., S. Sundby, B. Ådlandsvik, and Ø. Fiksen (2005), The combined effect of transport and temperature on distribution and growth of larvae and pelagic juveniles of arcto-norwegian cod, *ICES Journal of Marine Science*, *62*(7), 1375–1386, doi: 10.1016/j.icesjms.2005.05.017. 1.1

Vikebø, F., C. Jørgensen, T. Kristiansen, and Ø. Fiksen (2007), Drift, growth, and survival of larval northeast arctic cod with simple rules of behaviour, *Marine Ecology Progress Series*, *347*, 207–219, doi:10.3354/meps06979. 1.1

Vouriot, C. V. M., A. Angeloudis, S. C. Kramer, and M. D. Piggott (2018), Fate of large-scale vortices in idealized tidal lagoons, *Environmental Fluid Mechanics*, *19*, 329–348, doi:10.1007/s10652-018-9626-4. 5.2

Weber, J. E., and E. Børve (2021), Diurnal continental shelf waves with a permeable coastal boundary: Application to the shelf northwest of norway. 2.3

Weber, J. E. H., and M. Drivdal (2012), Radiation stress and mean drift in continental shelf waves, *Continental Shelf Research*, *35*, 108–116, doi:10.1016/j.csr.2012.01.001. 2.3, 2.3.2

Wells, M. G., and G.-J. F. van Heijst (2003), A model of tidal flushing of an estuary by dipole formation, *Dynamics of Atmospheres and Oceans*, *37*(3), 223–244, doi: 10.1016/j.dynatmoce.2003.08.002. 1.1, 2.2.2

Yaragina, N. A., A. Aglen, and K. M. Sokolov (2011), *Cod*, Tapir Academic Press. 1.1

Zhang, Z., and Q. Chen (2007), Comparison of the eulerian and lagrangian methods for predicting particle transport in enclosed spaces, *Atmospheric Environment*, *41*(25), 5236–5248, doi:https://doi.org/10.1016/j.atmosenv.2006.05.086, indoor Air 2005 - 10th International Conference on Indoor Air Quality and Climate (Part II). 3.2

Zhao, C., U. Daewel, and C. Schrum (2019), Tidal impacts on primary production in the north sea, *Earth System Dynamics*, *10*(2), 287–317, doi:10.5194/esd-10-287-2019. 1.1

Zhao, L., C. Chen, and G. Cowles (2006), Tidal flushing and eddy shedding in mount hope bay and narragansett bay: An application of fvcom, *Journal of Geophysical Research: Oceans*, doi:10.1029/2005JC003135. 3.1

Zimmerman, J. T. F. (1978), Topographic generation of residual circualtion by oscialltory (tidal) currents, *Geophysical & Astrophysical Fluid Dynamics*, *11*(1), 35–47, doi:10.1080/03091927808242650. 2.2.1, 2.2.1, 2.2.1, 2.2.1, 2.2.1

Zimmerman, J. T. F. (1981), Dynamics, diffusion and geomorphological significance of tidal residual eddies, *Nature*, *290*, 549–555, doi:10.1038/290549a0. 2.2.1, 2.2.1

Ådlandsvik, B., and S. Sundby (1994), Modelling the transport of cod larvae from the lofoten area, *ICES Mar Sci Symp*, *198*, 379–392. 1.1

Part II

Papers

I

Paper I

Flow separation, dipole formation and water exchange through tidal straits

Ole Anders Nøst **Børve, Eli**
Ocean Science, *accepted - 2021*
doi:10.5194/os-2021-30

Flow separation, dipole formation and water exchange through tidal straits

Ole Anders Nøst[1,3] and Eli Børve[2,4]

[1]Akvaplan-niva AS, 7462 Trondheim, Norway
[2]The University of Oslo, Department of Geosciences, 0315 Oslo, Norway
[3]Nord University, 8026 Bodø, Norway
[4]Akvaplan-niva AS, 9296 Tromsø, Norway

Correspondence: Ole Anders Nøst (oan@akvaplan.niva.no)

Abstract. We investigate the formation and evolution of dipole vortices and their contribution to water exchange through idealized tidal straits. Self-propagating dipoles are important for transporting and exchanging water properties through straits and inlets in coastal regions. In order to obtain a robust data-set to evaluate flow separation, dipole formation and evolution and the effect on water exchange, we conduct 164 numerical simulations, varying the width and length of the straits as well as the tidal forcing. We show that dipoles form and start propagating at the time of flow separation, and their vorticity originates in the velocity front formed by the separation. We find that the dipole propagation velocity is proportional to the tidal velocity amplitude, and twice as large as the dipole velocity derived for a dipole consisting of two point vortices. We analyse the processes creating a net water exchange through the straits and derive a kinematic model dependent on dimensionless parameters representing strait length, dipole travel distance and dipole size. The net tracer transport resulting from the kinematic model agrees closely with the numerical simulations and provide understanding of the processes controlling net water exchange.

1 Introduction

Knowledge of coastal ocean transport processes is vital for predicting human impact on the coastal marine environment. Coastal industry discharges pollutants and nutrients into the ocean. In order to understand the impact on the environment, we need coastal ocean circulation models to calculate concentrations and pathways of spreading. Setting up such models for a complex coastline requires a high level of understanding of near-shore transport processes in order to realistically represent these in the models. In shallow coastal regions with complex topography, tides are often a dominant driver of the ocean circulation and transport. In this study, we investigate the exchange process of tidal pumping through narrow tidal straits.

Tidal pumping is an important mechanism responsible for transport of water properties and particles like fish eggs, nutrients, and pollution between estuaries and the open ocean, or in coastal regions with complex geometry in general (Chadwick and Largier, 1999; Fujiwara et al., 1994; Brown et al., 2000; Amoroso and Gagliardini, 2010; Ford et al., 2010; Vouriot et al., 2019). The exchange process results from an asymmetry in the flow field between the ebb and flood phase of the tide (Stommel and Farmer, 1952; Wells and van Heijst, 2003). Flow asymmetry may occur when the tidal current interacts with a topographic constriction like a strait or an inlet. When entering the constriction the flow arrives from all directions and speeds up in order

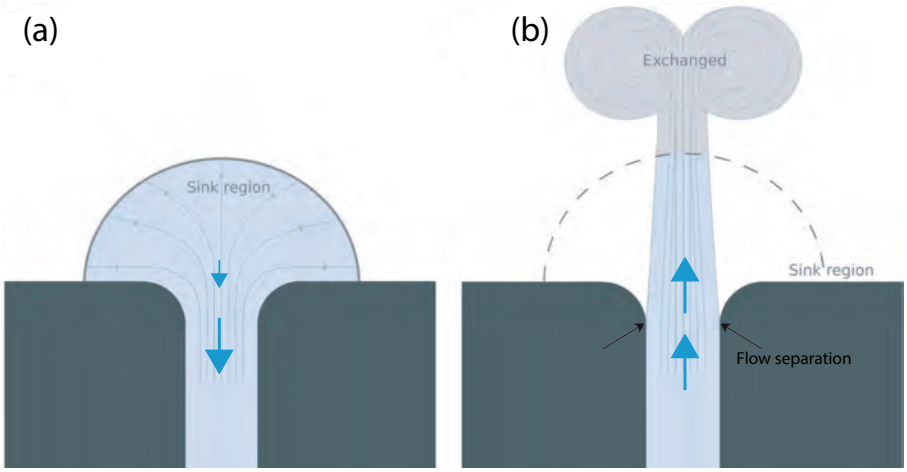

Figure 1. A sketch of the processes at play in water exchange by tidal pumping. a) southward inflow to the strait. b) northward outflow from the strait.

to conserve volume, as illustrated by Fig. 1a. The area covered by the volume that enters the strait is called the sink region (Fig. 1a). The acceleration is associated with a pressure force towards the constriction which acts to lower the water level in the centre of the constriction. Contrary, when the flow reverses and the flow exits the strait, the cross-sectional area increases and the sea surface rises downstream of the constriction. Here, both friction and pressure forces work to decelerate the flow, which is a necessary condition for flow separation (Kundu, 1990). Since friction and pressure now works in the same direction, the flow is likely to come to a halt near the coastline where the friction is strongest. When this happens, the flow separates from the coastline as illustrated by Fig. 1b (Kundu, 1990; Signell and Geyer, 1991). When the flow separates a vortex forms at the point of separation. If the flow separates at both sides of the exit, two vortices of opposite sign will form with a separation distance roughly equal to the width of the strait. The strength of the vortices and the distance between them determine whether they will interact and form a self-propagating dipole. The dipoles capture and transport water ejected from the strait away from the opening and possibly out of the sink region. At flow reversal, the dipole will either be drawn back into the strait or continue moving away and escape. If the dipole escapes the return flow it will contribute to a considerable water exchange (Fig. 1b).

The propagation of dipoles has been studied for more than 100 years (Lamb, 1916; Batchelor, 1967; Kundu, 1990), and the velocity of a self propagating dipole is typically represented as

$$U_{dip} = \frac{\Gamma}{2\pi b}. \tag{1}$$

Here b is the distance between the vortex centers, and Γ is the magnitude of the circulation in each of the two vortices, assuming they are of equal strength. Equation 1 is valid as long as the distance between the two vortices is large compared to their core radius (Yehoshua and Seifert, 2013; Delbende and Rossi, 2009; Habibah et al., 2018). Habibah et al. (2018) show that a correction to the velocity given by Eq. 1 occurs in the 5th order of a/b where a is the core radius of the vortices. In cases where a/b increases, the vortices becomes elliptical and the dipole propagation velocity decreases (Delbende and Rossi, 2009).

Equation 1 describes the propagation velocity of a dipole moving by self-propagation in an otherwise non-moving ocean. It is unclear whether this is valid for a dipole formed in a tidal strait, where the background flow is clearly non-zero. Also, dipoles propagating away from the strait often remain attached to the strait via a trailing jet (Fig. 1b), which provides a pathway of mass, momentum and vorticity from the strait into the dipole (Wells and van Heijst, 2003; Afanasyev, 2006). As the dipole accumulate vorticity the circulation in the dipole increases, and the propagation velocity should therefore accelerate according to Eq. 1. However, this is not necessarily true. In a lab experiment investigating dipole formation by a steady channel jet Afanasyev (2006) found that the dipole propagated with constant speed, even though the dipole continuously accumulated vorticity fed by a trailing jet.

The circulation of the dipole vortices is an important parameter for determining the propagation velocity, and to determine the circulation it is vital to know the source of vorticity. A common assumption is that the vorticity is created in the viscous boundary layer (Wells and van Heijst, 2003; Nicolau del Roure et al., 2009; Bryant et al., 2012). Another possible source is the flow discontinuity resulting when the flow separates from the coastline (Kashiwai, 1984a, b). Kashiwai (1984a, b) and Wells and van Heijst (2003) both assume that all vorticity generated in the strait accumulates in the dipole vortices. The circulation can then be expressed as $\Gamma \propto U^2 T$, where T is the tidal period and U is a characteristic velocity scale for the strait (Kashiwai, 1984b; Wells and van Heijst, 2003). However, Afanasyev (2006) showed that the vorticity is divided between the dipole and the trailing jet. In addition, Afanasyev (2006) introduced a new time-scale, which he called the "startup time", t_s. The startup time indicates the moment when the dipole starts translating after an initial period of growth, where the jet is injected into the dipole.

The net tracer transport through a tidal strait is commonly classified by the nondimensional Strouhal number, S_t, defined as (Kashiwai, 1984a; Wells and van Heijst, 2003; Nicolau del Roure et al., 2009)

$$S_t = \frac{W}{UT}, \tag{2}$$

where W is the strait width, T is the tidal period and U is the velocity scale characterising the velocity in the strait. W can also be seen as a characteristic spatial scale of a dipole formed at the strait exit, and in this case S_t is a measure of the ratio between linear and non-linear acceleration terms. The center of the dipole vortices are pressure minima, and the non-linear acceleration associated with the azimuthal velocity of the vortices is balanced by pressure forces. Thus, for a dipole vortex to exist, $S_t \ll 1$ is a necessary condition.

Net tracer transport by tidal pumping is associated with $S_t < S_{tc}$, where S_{tc} is a threshold value of S_t (Kashiwai, 1984a; Wells and van Heijst, 2003). The threshold value of the Strouhal number arrives from a kinematic consideration of the dipole movement over one tidal period, and separates between dipoles who escape the return flow and the dipoles that returns to the strait during the subsequent phase of the tide (Kashiwai, 1984a; Wells and van Heijst, 2003). Dipoles escaping the return flow contribute to net water exchange through the strait. A treshold value $S_{tc} = 0.13$ was found by (Wells and van Heijst, 2003) and this value is later confirmed by (Vouriot et al., 2019) in a numerical study of idealized tidal lagoons.

In this study, our aim is to understand how the geometric constraint of a tidal strait influences the effectivity of tidal pumping. We systematically perform 164 numerical simulations in an idealized tidal strait, varying the width and length of the straits

as well as the amplitude of the tidal forcing. Although 3D processes may affect vortex flows (van Heijst, 2014; Albagnac et al., 2014), we believe a 2D depth averaged approach will give valuable new insight into tidal strait flows. A 2D approach is therefore used in this study. The results of the simulations are analysed with focus on flow separation, dipole formation and propagation and net water exchange. Finally, we derive a simple kinematic model for net tracer transport that fits well to the results from the simulations and brings understanding to the process of water exchange through a tidal strait.

2 Modelling

2.1 The model

We use the Finite Volume Community Ocean Model (FVCOM) (Chen et al., 2003). FVCOM has been used in numerous studies of coastal and estuarine waters (Lai et al., 2015, 2016; Sun et al., 2016; Li et al., 2018; Chen et al., 2021) and also globally and in the Arctic Ocean (Chen et al., 2016; Zhang et al., 2016). FVCOM uses an unstructured triangular grid in the horizontal and terrain-following σ-coordinates in the vertical (Chen et al., 2003). The model solves the equations for momentum and mass conservation as well as the equations for temperature, salinity and density. In our case, we set temperature, salinity and density to constant values and FVCOM then solves the following equations

$$\begin{aligned}
\frac{\partial u}{\partial t}+u\frac{\partial u}{\partial x}+v\frac{\partial u}{\partial y}+w\frac{\partial u}{\partial z}-fv&=-\frac{1}{\rho_0}\frac{\partial p}{\partial x}+\frac{\partial}{\partial z}\left(K_m\frac{\partial u}{\partial z}\right)+F_u\\
\frac{\partial v}{\partial t}+u\frac{\partial v}{\partial x}+v\frac{\partial v}{\partial y}+w\frac{\partial v}{\partial z}+fu&=-\frac{1}{\rho_0}\frac{\partial p}{\partial y}+\frac{\partial}{\partial z}\left(K_m\frac{\partial v}{\partial z}\right)+F_v\\
\frac{\partial u}{\partial x}+\frac{\partial v}{\partial y}+\frac{\partial w}{\partial z}&=0\\
\frac{\partial p}{\partial z}&=-\rho_0 g.
\end{aligned} \tag{3}$$

x, y and z are the Cartesian coordinates in east, north and vertical directions, respectively, u, v and w are the x, y and z components of velocity, respectively; p is pressure; ρ_0 is the constant density; f is the Coriolis parameter; g is the acceleration of gravity; K_m is the eddy diffusion coefficient and F_u and F_v are the diffusion terms for horizontal momentum in x and y directions, respectively. The calculation of K_m is done with the Mellor and Yamada (1982) level 2.5 turbulent closure scheme, modified by Galperin et al. (1988). F_u and F_v are calculated using the eddy parameterization method by Smagorinsky (1963). The diffusion coefficient within F_u and F_v is given by

$$A_m=0.5C\Omega\sqrt{(\frac{\partial u}{\partial x})^2+0.5(\frac{\partial v}{\partial x}+\frac{\partial u}{\partial y})^2+(\frac{\partial v}{\partial y})^2}, \tag{4}$$

where C is a constant, set to 0.1 in our case, and Ω is the grid cell area.

The surface boundary conditions are

$$\left.\begin{aligned}
K_m\left(\frac{\partial u}{\partial z},\frac{\partial v}{\partial z}\right)&=\frac{1}{\rho_0}(\tau_{sx},\tau_{sy})\\
w&=\frac{\partial \zeta}{\partial t}+u\frac{\partial \zeta}{\partial x}+v\frac{\partial \zeta}{\partial y}
\end{aligned}\right| z=\zeta(x,y,t), \tag{5}$$

where τ_{sx} and τ_{sy} are the surface stress in x and y directions, respectively, and ζ is the surface elevation. The bottom boundary conditions are

$$\left.\begin{array}{c} K_m\left(\frac{\partial u}{\partial z}, \frac{\partial v}{\partial z}\right) = \frac{1}{\rho_0}(\tau_{bx}, \tau_{by}) \\ w = -u\frac{\partial H}{\partial x} - v\frac{\partial H}{\partial y} \end{array}\right| z = -H(x,y), \tag{6}$$

where τ_{bx} and τ_{by} are the bottom stresses in the x and y direction, respectively and H is the bottom depth. The bottom stresses are given by

$$(\tau_{bx}, \tau_{by}) = \rho_0 C_d \sqrt{u^2 + v^2}(u, v), \tag{7}$$

where the drag coefficient

$$C_d = max\left(\frac{\kappa^2}{ln(\frac{z_b}{z_0})^2}, 0.0025\right). \tag{8}$$

Here, κ is von Karmans constant (~ 0.4), z_0 is the bottom roughness set to be 0.001 m and z_b is height above bottom of the lowest horizontal velocity level.

2.2 Setup of simulations

The model domain is bounded by a semi-circled open ocean and a straight coastline on the eastern side (Fig. 2). The full domain is 500 km in the north-south direction and up to 250 km in the east-west direction. At the center of the eastern boundary, we place a peninsula and an island separated by a strait. The strait is the focus of our study. The idea behind this configuration is that the pressure difference over the length of the strait is set by the tidal wave travelling in the open ocean and not by the flow through the strait. In this way, the flow through different strait geometries will be forced similarly. The setup can be seen as an idealized representation of the Lofoten peninsula in northern Norway.

Surface stress (Eq. 5) is set to zero, and the only forcing of the simulations is a northward propagating Kelvin wave specified at the semi-circled western boundary

$$\zeta_{obc} = A_t e^{\frac{(x-x_c)}{R_d}} sin(ky - \omega t). \tag{9}$$

Here, $\omega = 2\pi/T$, T is the M2 tidal period (12.42 hours), $k = \omega/\sqrt{gH}$, x_c is the constant position along the x-axis of the straight eastern coast (ignoring the peninsula) and R_d is the Rossby radius of deformation. Equation 9 describes a classical Kelvin wave moving northward with the coast to the right (Gill, 1982). The Coriolis parameter corresponds 70°N latitude and the depth $H = 100$ m, giving a Rossby radius $R_d \simeq 230$ km. The surface elevation given by Eq. 9 is specified at the boundary nodes. The velocities in FVCOM is located in the center of each triangular cell, and not directly at the boundary. The velocities in the open boundary cells are calculated based on the assumption of mass conservation (Chen et al., 2003, 2011).

In order to investigate the geometric effects on the tidal pumping, we vary the width of the strait, W, from 1 km to 12 km, and the length of the strait, L, from 4 km to 22 km. The curvature of the coastline at the strait entrance and exit is equal and

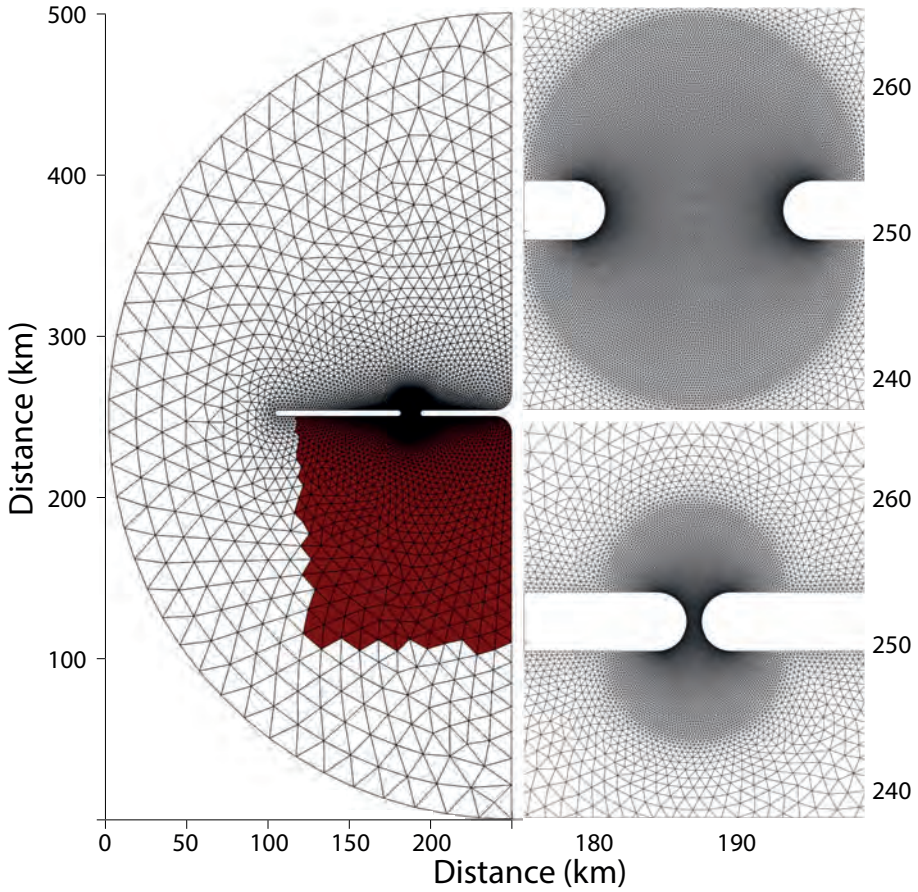

Figure 2. Left panel: The entire model domain with the peninsula attached to the eastern coast and the island located west of the peninsula. The red color marks the area with initial tracer concentration equal $1m^{-3}$. Right panel: The mesh near the strait with 12 km width (top) and 1 km width (bottom).

shaped as a quarter of a circle with a radius of $R = 2$ km. The strait is directed north-south, and the geometry and coordinates used in the study is shown in Fig. 3b. In total we conduct 164 idealized simulations using 82 different strait geometries and two different amplitudes of the tidal forcing ($A_t = 1$ and $A_t = 0.5$, see Eq. 9).

We simulate a homogeneous ocean over a flat bottom of 100 m depth. To avoid unwanted effects of boundary layers near a vertical wall, we use a sloping bottom at the innermost 600 m from the coastline inside the strait (Fig. 3a). The minimum depth is 5 m. Because our tracer model requires vertical layering, we divide the water column into two layers in the vertical. However, the analysis of results are done using vertically averaged velocities and this work can therefore be regarded as a 2D barotropic study. z_b is roughly equal to a quarter of the total depth resulting in a slightly increased drag coefficient over the shallow depths near the sides of the strait (Eq. 8). $z_b = 1$m gives $C_d = 0.0034$ while $C_d = 0.0025$ for $z_b > 2.8$m.

Inside the strait the resolution is 50 m along the coastline. Inside the focus region surrounding the strait the resolution linearly coarsens to 200 m with distance from the coast. The focus region is, in addition to the strait itself, the semi-circle (radius $= W/2 + 2R$) of high resolution at both sides of the strait entrances (Fig. 2). Outside the focus area, the resolution coarsens further to 2 km both at the western tip of the island and at the coastline to the east. At the western open boundary the resolution is 20 km.

The simulations are run for a total of 20 days. First, a 10 days spin-up, before we introduce a passive tracer, which is simulated using the Framework for Aquatic Biogeochemical Models (Bruggeman and Bolding, 2014, FABM) coupled to FVCOM. The initial concentration of the tracer is set to 1 m^{-3} inside a rectangular box south of the strait, and 0 m^{-3} elsewhere (left panel in Fig. 2). The northern edge of the initial tracer release is at the center of the strait. This configuration of the initial concentration restricts the tracer exchange in the north-south direction to be through the strait only.

3 Overview of model results

By visual inspection we see that vortices form in all the different strait configurations. However, only a fraction of the straits produces self-propagating dipoles. Figure 4 provides an overview of all the simulations and the straits where self-propagating dipoles are visually observed. The dipole formation clearly depends on the strait geometry, where narrow and short straits favor dipole formation. Additionally, with stronger tidal forcing ($A_t = 1.0$ m) dipoles form in wider and longer straits compared to when the tidal forcing is weak ($A_t = 0.5$ m). In this section, we present an overview of the results illustrated by the temporal evolution of the tracer and vorticity distribution in three representative simulations.

We choose to show three examples where the tidal forcing and the strait length are equal ($A_t = 1$ m and $L = 4$ km), and the strait widths are $W = 1$ km, $W = 4.5$ km and $W = 12$ km, respectively. The difference in strait width results in different temporal evolution of the tracer distribution and the vorticity fields. We show the results from the first half of the tidal cycle, which we define to start at slack tide after ebb. The first six hours (t = 0-6 hours) are during flood tide and the tidal current is directed northward. All three examples have flow separation and vortex formation at the strait exit, but only in the two former do the vortices connect into self-propagating dipoles.

In the narrowest strait ($W = 1$ km, Fig. 5), the flow separates and vortices form 1.5 hours after slack tide. At this point the flow is dominated by two separated shear layers with negative (right) and positive (left) vorticity. The separated shear layers are connected via a trailing jet to the two initial vortices, which now form a self-propagating dipole. The dipole at this stage consists of two intense vortex cores filled with water having tracer concentration near 1. After 3 hours, the dipole has increased in size and the vortex cores are somewhat less intense. The outer part of the dipole now consists of water with near zero vorticity and near zero tracer concentration. The streamlines indicate that this low concentration water has not come through the strait but is entrained into the dipole at the northern side of the strait. The dipole continues to grow while moving northward, fed by the trailing jet and by entrainment of low vorticity water. Since the dipole is formed early in the tidal cycle, the dipole has time to propagate far northward before the flow reverses.

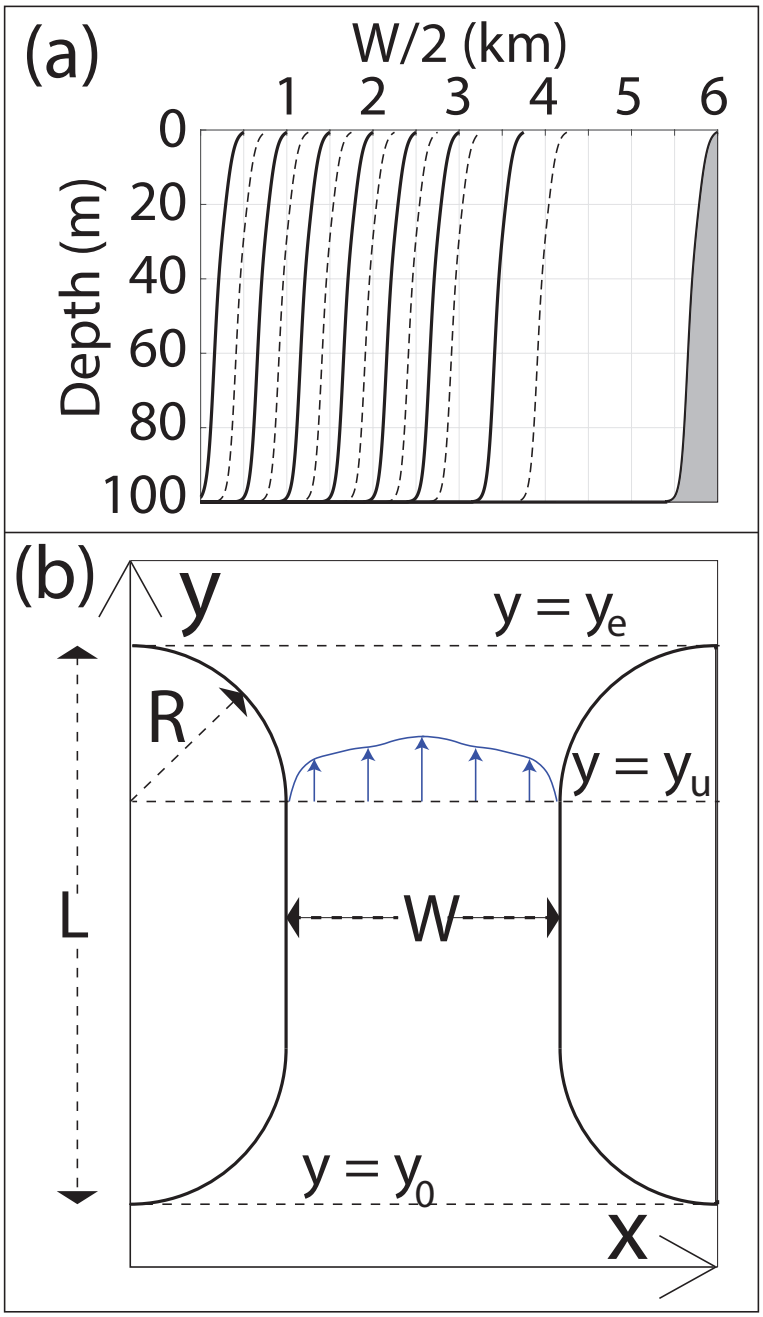

Figure 3. a) Vertical cross-section of bottom topography from the strait center to the eastern coastline for the different strait widths. The solid and dashed lines are used to more easily differentiate between the different strait widths. b) The coordinate system of the strait configuration.

In the 4.5 km wide strait (Fig. 6) the time period from slack tide till flow separation and dipole formation is longer than in the 1 km wide strait. At 1.5 hours separation has not yet occurred. The vorticity is confined to the narrow viscous boundary

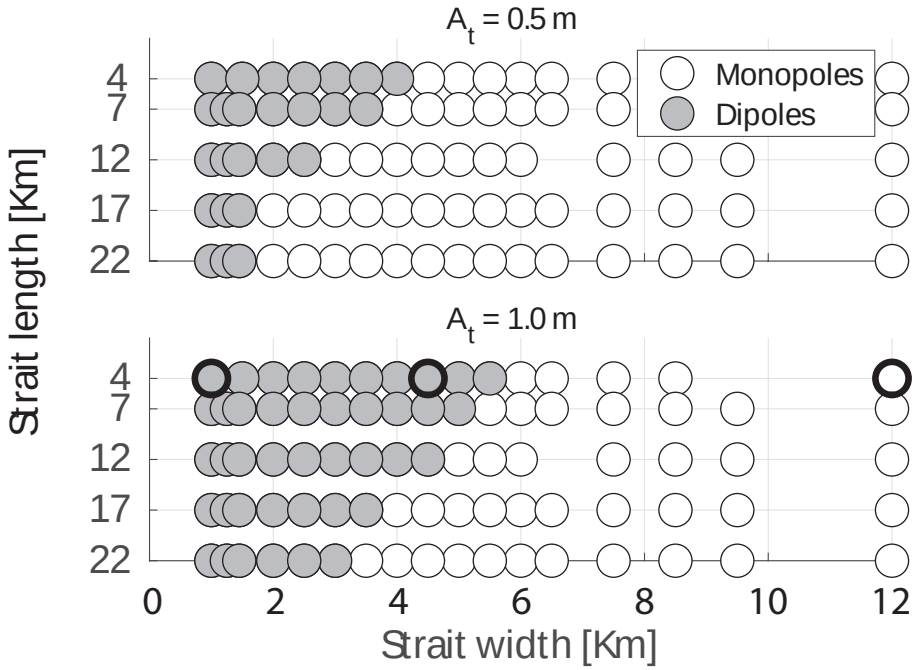

Figure 4. Overview of all simulations performed in this study. Gray color marks simulations where self propagating dipoles are formed. The upper and lower panel displays simulations forced with a tidal wave height amplitude of $A_t = 0.5$ m and $A_t = 1$ m, respectively. The three black thick circles mark the three simulations shown in Fig. 5 to 7

.

layers, while the tracer has started to exit the strait. The width of the two boundary layers is similar to the 1 km strait. However, since the strait is wider, the boundary layers occupy a smaller fraction of the strait. Most of the water flowing through the strait therefore has near zero vorticity. At 3 hours, a dipole has formed and grows while moving northward during the tidal period. The vorticity is mainly located inside the vortex cores and most of the dipole consist of water with near zero vorticity. An obvious difference from the 1 km wide strait (Fig. 5) is that much of the near zero vorticity water in the dipole has come through the strait and contains tracer. This leads to a pattern where the tracer covers a larger area than the vorticity. The dipole barley detaches from the coastline before the flow reverses, and no proper trailing jet is formed. Instead, we observe a continuous vortex shedding from the separated shear layer at the strait exit, which to some degree interact and merge with the stronger initial vortices.

In the widest strait ($W = 12$ km) we observe a continuous vortex shedding from the boundary layer similar to the 4.5 km wide strait (Fig. 7). However, the vortices never interact across the width of the strait to form a dipole. In addition to a larger separation distance between the counter-rotating vortices, the flow also separates later than in the two former examples. The first vortices observed at the exit, three hours after slack tide, are advected through the strait and not formed at the northern exit during the ongoing tidal phase. First after almost four hours, are the first vortices shed from the separated boundary layer.

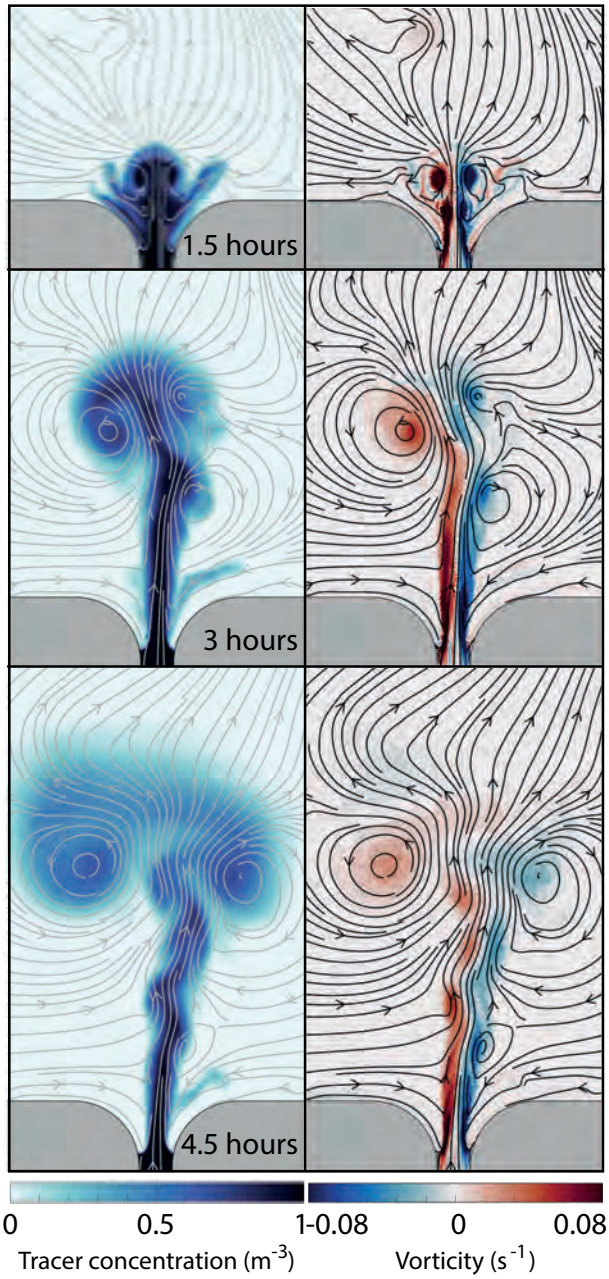

Figure 5. The temporal tracer and vorticity fields, with the corresponding stream-function, is displayed for a 1 km wide and 4 km long strait in the left and right panel, respectively. The experiment is forced with a tidal wave of amplitude $A_t = 1$ m. The upper, middle and lower panels shows a snapshot in time of the tracer and the vorticity fields at 1.5 hours, 3 hours and 4.5 hours after slack tide, respectively.

These vortices do not interact across the strait to form a dipole, but rather seem to interact and merge with other co-rotating

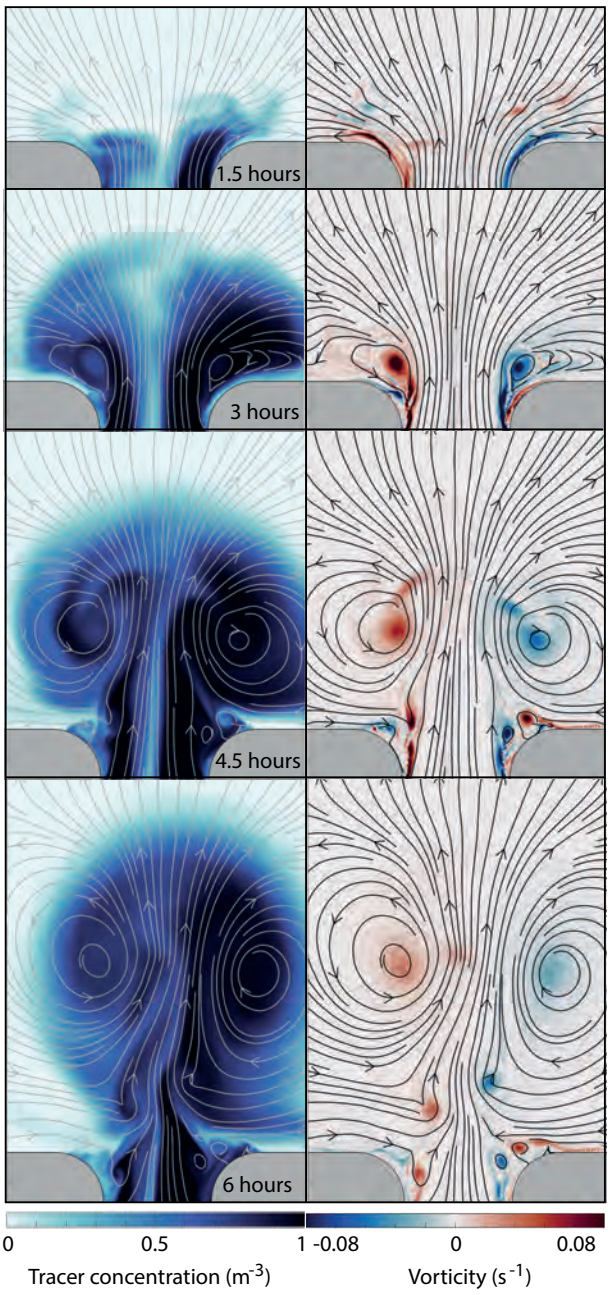

Figure 6. The temporal tracer and vorticity fields, with the corresponding stream-function, is displayed for a 4.5 km wide and 4 km long strait in the left and right panel, respectively. The experiment is forced with a tidal wave of amplitude $A_t = 1$ m. The upper, middle and lower panels shows a snapshot in time of the tracer and the vorticity fields at 1.5 hours, 3 hours and 4.5 hours after slack tide, respectively.

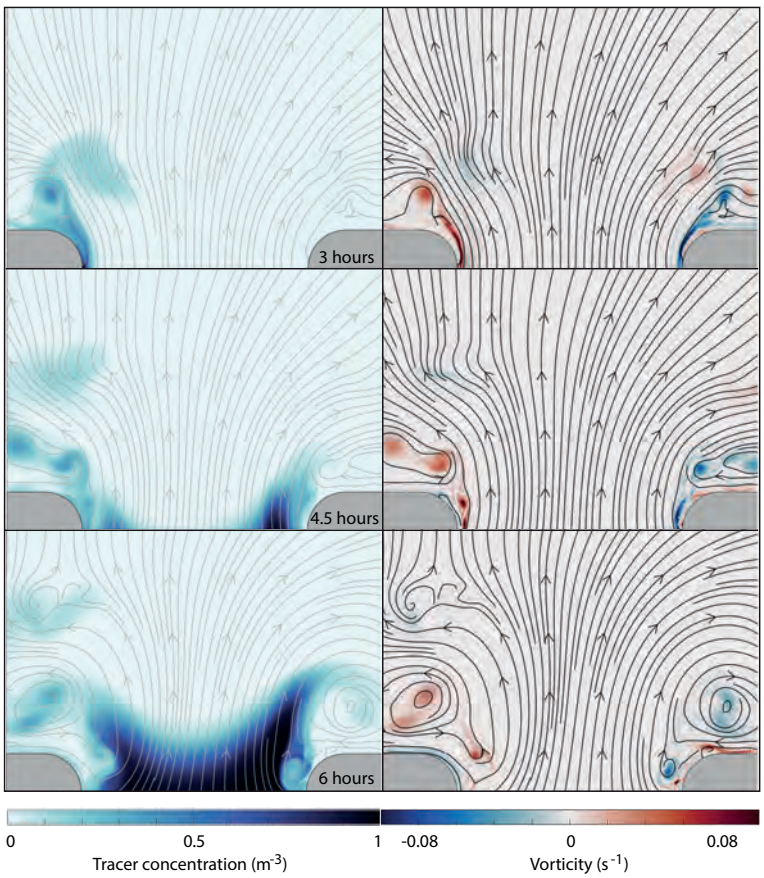

Figure 7. The temporal tracer and vorticity fields, with the corresponding stream-function, is displayed for a 12 km wide and 4 km long strait in the left and right panel, respectively. The experiment is forced with a tidal wave of amplitude $A_t = 1$ m. The upper, middle and lower panels shows a snapshot in time of the tracer and the vorticity fields at 1.5 hours, 3 hours and 4.5 hours after slack tide, respectively.

vortices at the same side of the strait. Since no self-propagating dipoles are formed, the vortices do not escape the return flow and the net tracer transport through the strait is near zero.

The three examples shown in Fig. 5 to 7 all have the same channel length, but they illustrate the process of dipole formation and dipole transport properties. These processes are similar for all channel lengths, although the channel length influences channel flow and thereby whether dipoles form or not. In general, longer straits require narrower strait widths for dipoles to form (Fig. 4), and flow separation and vortex formation occurs later in the tidal cycle.

In the following, we go into the details of flow separation, vortex formation and dipole properties. These topics are important for the understanding of how strait geometry affects flow dynamics and water exchange through narrow tidal straits.

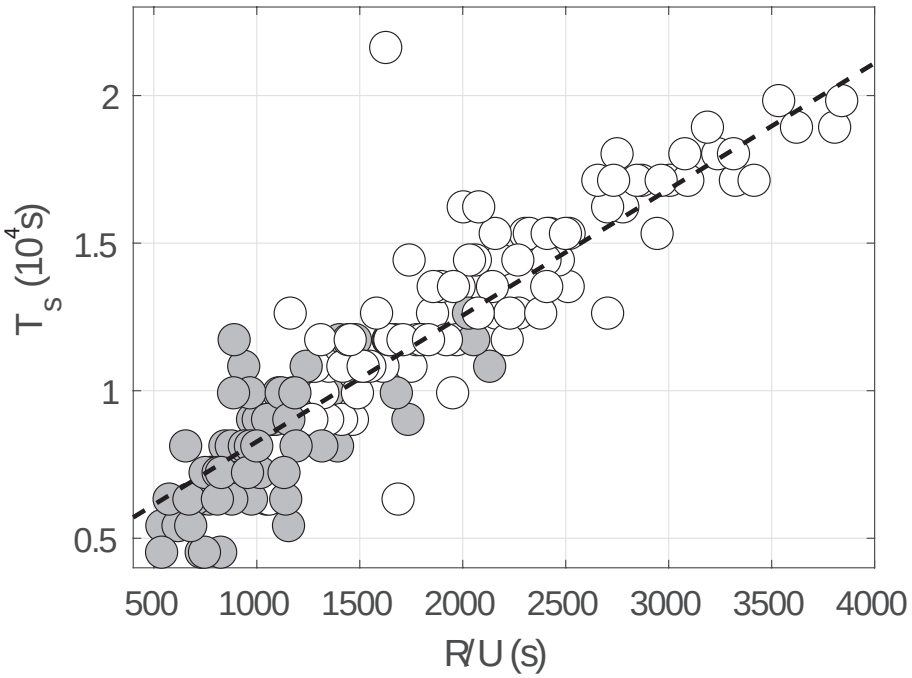

Figure 8. Separation-time (T_s) plotted against (R/U). The dashed line is the best linear fit $T_s = 4.3R/U + 3998$. Straits with self propagating dipoles are marked gray.

4 Flow separation and vortex formation

The timing of flow separation depends on the flow dynamics at the strait exit. Here the balance between non-linear advection and pressure forces leads to an adverse pressure gradient caused by the widening of the strait. The flow separates from the coastline when the adverse pressure gradient acts in the same direction as the friction and brings the velocity in the viscous boundary layer to zero (Signell and Geyer, 1991; Kundu, 1990). Since the adverse pressure gradient results from the nonlinear advection, the separation time can be related to the ratio of local acceleration to nonlinear advection, also called the Keulegan-Carpenter number (K_c) (Signell and Geyer, 1991). Flow separation can occur when

$$K_c = \frac{UT^*}{R} > 1, \tag{10}$$

where T^* is the timescale where the flow dynamics become non-linear and R is the length scale of the strait exit (Fig. 3b). From here and through the rest of the paper, the velocity scale U is given by the tidal velocity amplitude. This is calculated as the maximum in time of the cross-strait average at $y = y_u$ (Fig. 3 for coordinate definitions). Assuming the time of separation, T_s, can be related to T^* and that K_c must obtain a certain value for separation to occur, then T_s should be proportional to R/U. This relation is confirmed when plotting T_s against R/U (see Fig. 8). Here, T_s is the separation time obtained from the model results (details of how T_s is obtained are given below). Corresponding values of K_c lay mainly between 5 and 15.

The formation of starting vortices and self-propagating dipoles occurs when the flow separates. The vorticity needed to form these vortices originates from the strong velocity front that is formed at the boundary between the newly separated flow and the reversed flow along the coast. At the time of flow separation, the velocity front immediately rolls-up into a vortex. This process is illustrated in Fig. 9, where the flow field near the point of separation is plotted on top of vorticity and surface elevation for the same three simulations shown in Fig. 5 to 7. The vorticity created in the velocity front causes a maximum absolute value of vorticity to occur at separation time. This is shown in Fig. 10 for the same three simulations shown in Fig. 9.

For the simulations with strait widths 1 km and 4.5 km (upper and middle panel of Fig. 9) the two initial vortices interact and form a dipole. In these two straits we see a rapid buildup towards the maximum absolute value in vorticity followed by a decrease (black and green curve in Fig. 10). In the 1 km wide strait the initial vortices remain attached to the strait by a trailing jet, and we observe only one prominent peak in maximum absolute value of vorticity (black curve in Fig. 10). In the 4.5 km wide strait several vortices are shed from the separated velocity front after the initial vortex shedding (see Fig. 6), and several local maximums occurs after flow separation (green curve in Fig. 10). In the widest strait the initial vortices never connect into a dipole, and the maximum absolute value of vorticity is much less prominent compared to the narrower straits (blue curve in Fig. 10). However, also for the widest strait we observe by visual inspection that the maximum absolute value of vorticity coincides with the initial vortex formation due to flow separation, at about 4 hours after slack tide. We find that, for all simulations, the maximum absolute value of vorticity corresponds to the separation time. Therefore, the separation time is estimated from the timing of the absolute value of vorticity within the strait exit ($y_u < y \leq y_e$, see Fig. 3b).

The initial vorticity of the vortices created during flow separation is an important parameter for determining their ability to form a dipole, as well as the propagation velocity of the dipole that forms. Here, the vortices are represented by the radial profiles of Lamb-Oseen (LO) vortices (Lamb, 1916; Leweke et al., 2016),

$$v_\theta = \frac{\Gamma}{2\pi r}(1 - e^{-\frac{r^2}{a^2}}) \tag{11a}$$

$$\xi = \frac{\Gamma}{\pi a^2} e^{-\frac{r^2}{a^2}}, \tag{11b}$$

where ξ is the vorticity, Γ is the circulation of the vortex, a is the radius of the vortex core and r is the distance from the center of the vortex core. Originally a increases with time and depends on viscosity. Equation 11 is a particular solution to the Navier-Stokes equations (Habibah et al., 2018), and is known to show good agreement with experimental data (Leweke et al., 2016). The vortex shape described by Eq. 11 fits well to our modelled vorticity (see Fig. 11). We obtain the core radius a by finding the best fit of Eq. 11 to the modelled vortices, using the maximum and minimum vorticity from the model data.

From the results shown in Fig. 9 we see that the newly formed vortices have nearly equal size, even though the three simulations have very different characteristics. The estimation of core radius for all 164 simulations shows that what is indicated by Fig. 9 is a general result. The estimated core radius at separation time is given by $a(T_s) = 110 \pm 18$ m for all simulations and $a(T_s) = 116 \pm 14$ m for the dipoles (mean $\pm$ one standard deviation, see Fig. 12). This suggests that the vortex core radius is near constant across all simulations, which again suggests that the vorticity should be proportional to the strait velocity. Plotting the maximum absolute value of vorticity against the along-strait velocity at separation time $v(T_s)$ (Fig. 13), suggests

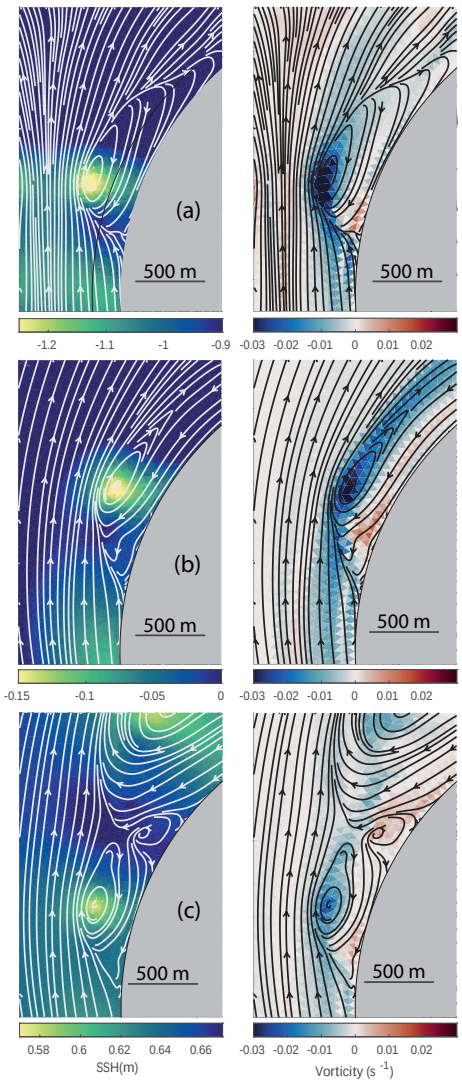

Figure 9. Sea surface height (left) and the vorticity (right), with contours showing the corresponding stream lines, are shown at separation time. We show the fields in the three straits displayed in a) Fig. 5 ($W = 1$ km), b) Fig. 6 ($W = 4.5$ km), and c) Fig. 7 ($W = 12$ km), respectively.

that the maximum absolute value of vorticity can be represented as

$$|\xi(T_s)|_{max} \simeq \frac{|v(T_s)|}{a(T_s)}. \tag{12}$$

245 It must be kept in mind that the simulated values of vorticity is strongly dependent on resolution. However, the important point is that vorticity can be expressed as shown in Eq. 12 and Fig. 13, which is likely to be true also for higher resolution simulations with higher maximum vorticity. The effect of resolution will be discussed in more detail in Section 8.1.

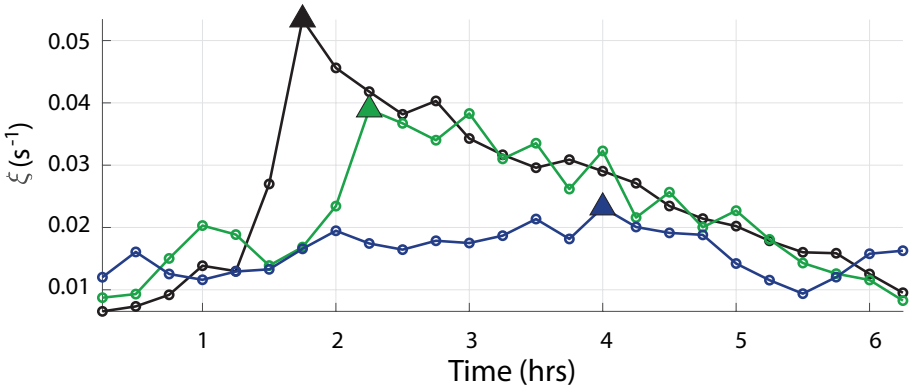

Figure 10. Time-series of the maximum magnitude of vorticity at the strait exit, defined as the area where $y_u < y \leq y_e$. The black, green and blue curves represents the same three simulations shown in Fig. 5 to 7, respectively. The triangles mark the separation time.

We have shown that the flow separation coincides with a maximum in absolute value of vorticity and that the dipole is formed at the time of separation. The vorticity of the initial vortices are given by strait velocity divided by the core radius, and the initial core radius is near equal for all simulations. In the following section, we describe how dipole vortices are recognized and the determination of their propagation velocity.

5 Dipole recognition and tracking

To obtain dipole properties we track the initial vortices from the time of flow separation to the end of the tidal phase. The vortex centers are points of minimum surface elevation as seen in Fig. 9. So, when tracking the vortices, we simply track the minima in surface elevation. Typically, vortices form simultaneously on each side of the strait at separation time, and we start tracking the two minima in surface elevation from this moment. We evaluate the propagation velocity and direction of the two vortices to determine whether they have connected into a dipole or not using two criteria illustrated in Fig. 14.

The criteria are based on two simple principles. The first criterion is that a dipole will propagate normal to the line connecting the two vortices and therefore conserve the distance between them (Leweke et al., 2016). We observe that vortices that do not connect into dipoles tend to be advected to each side of the strait opening, increasing the distance between them. The second criterion is based on the fact that a dipole escaping the returning tidal flow needs to have a propagating velocity over a certain limit. Fitting these two criteria to the results of visual inspection leads to the following formulations used to recognize dipoles in the simulation results (see Fig. 14 for notations),

$$\frac{b_2 - b_1}{2(y_2 - y_1)} < 2.9, \tag{13}$$

and

$$U_{dip} = \frac{y_2 - y_1}{\Delta t} > 0.2 ms^{-1}. \tag{14}$$

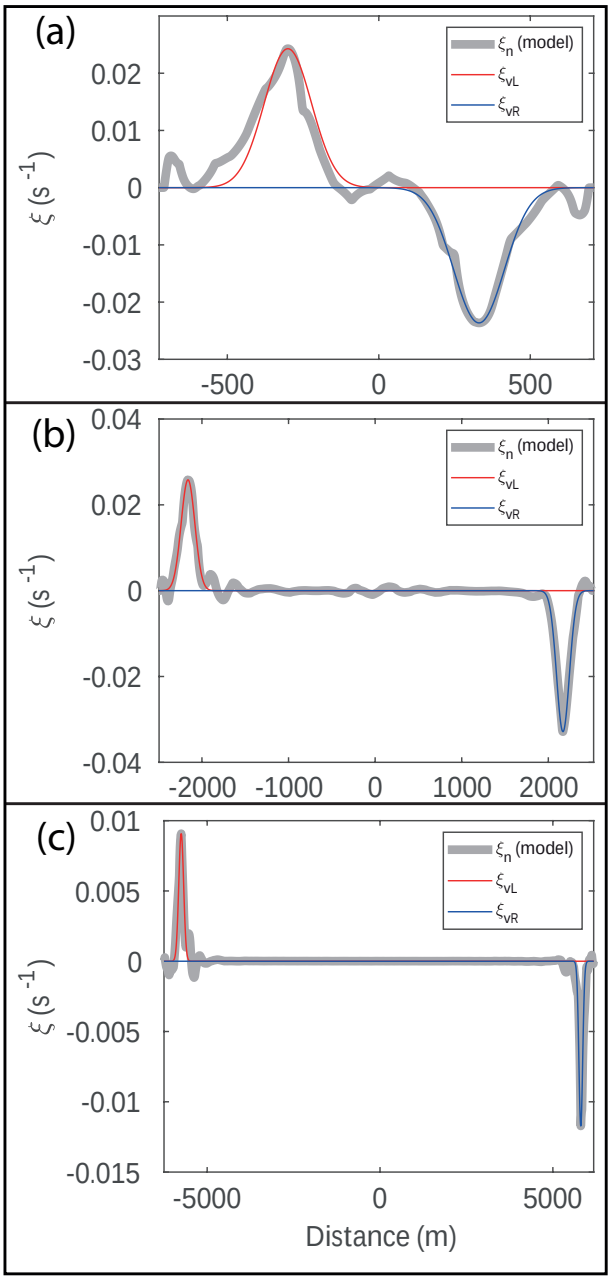

Figure 11. The vorticity distribution along a line intersecting the two vortices at each side of the strait at separation time. a), b) and c) is from the three simulations shown in Fig. 5 to 7, respectively. The gray line shows the vorticity distribution from the model output, while the red and blue lines are calculated vorticity distribution using Eq. 11b, for the left and right vortex, respectively.

The first of these criteria sets a limit to the increase in distance between the vortices compared to northward propagation of the dipole, while the second criterion requires that the dipole have a mean propagation speed larger than 0.2 m/s. Δt is the time

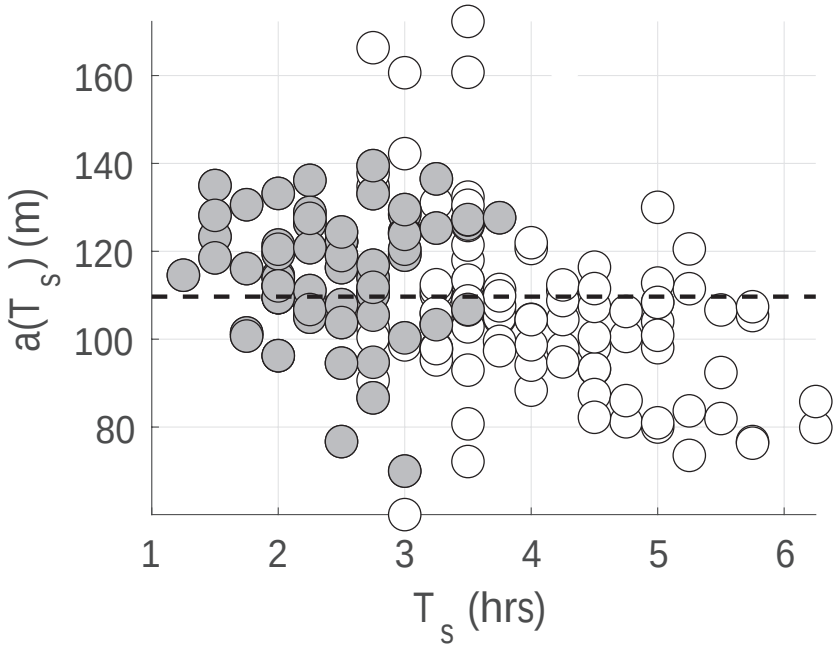

Figure 12. The vortex core radius at separation time, plotted against the separation time. The core radius is the mean radius of the two vortex cores formed at each side of the strait. Straits with self propagating dipoles are marked gray.

between the two dipole positions given by y_1 and y_2. The last criterion is important to rule out dipoles that form late in the tidal cycle and will not escape the strait before the tidal current reverses. These dipoles often are too slow to move out of the strait, and their separation distance is therefore near constant because it is restricted by the coastline. To recognise escaping dipoles, we find that it is necessary to set a lower limit to their propagation velocity and therefore we have introduced the second criterion defined by Eq. 14.

When tracking the vortices we obtain the dipole propagation velocities, which together with the tidal velocity and vorticity distributions, enables us to investigate the vortex properties.

6 Representation of the dipole propagation velocity

Dipole properties, such as core radius (a) and propagation velocity (U_{dip}) determine the net water exchange through the strait (Kashiwai, 1984a; Wells and van Heijst, 2003). Another important parameter is the sink radius (R_s). The water volume within the semi-circle (sink region, Fig. 1a) with radius R_s will be drawn into the strait when the flow reverses at $t = T/2$. If the dipole has travelled a distance larger than R_s it will escape the return flow. Here, we choose to investigate dipole properties inside the sink region.

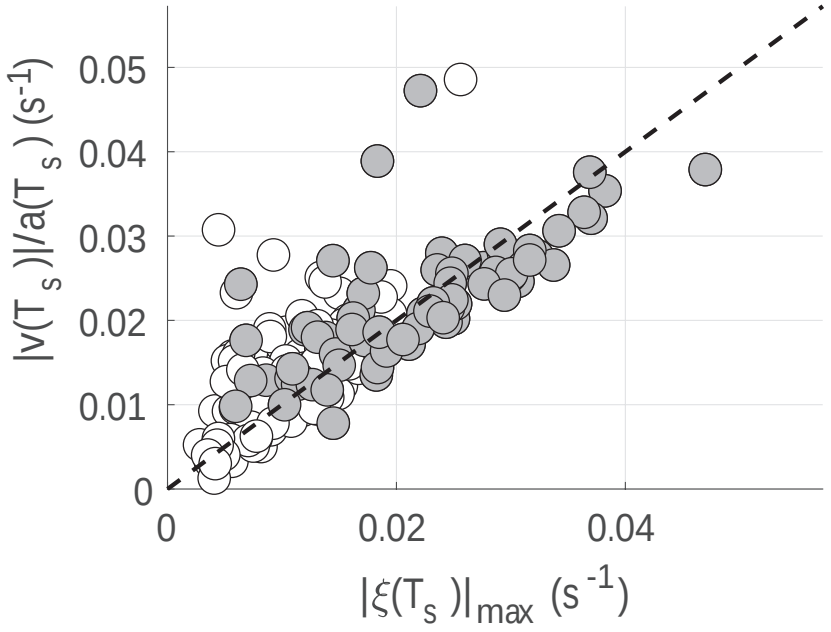

Figure 13. The theoretical velocity shear v/a plotted against the absolute value of the vorticity in the vortices at separation time. Straits with self propagating dipoles are marked gray.

Comparing the tracked dipole velocities to the theoretical velocities obtained from Eq. 1, we find that the dipole propagation velocity given by Eq. 1 is too low. Instead, we get a much better fit when using the sum of the contributions from the two vortices,

$$U_{dip} \simeq \frac{|\Gamma_1| + |\Gamma_2|}{2\pi b}, \tag{15}$$

where Γ_1 and Γ_2 are the circulation of the two vortices respectively. We calculate Γ_1 and Γ_2 from Eq. 11 using the value of maximum vorticity

$$\Gamma = \pi a^2 \xi_{max}, \tag{16}$$

and compare the dipole propagation velocity estimated using Eq. 15 to the tracked velocities. Figure 15 shows the comparison for each time-step in the same two simulations shown in Fig. 5 and 6, and Fig. 16a shows the comparison for dipole velocities averaged within the sink region.

Assuming the two vortices are of equal strength equal gives

$$U_{dip} \simeq \frac{\Gamma}{\pi b}. \tag{17}$$

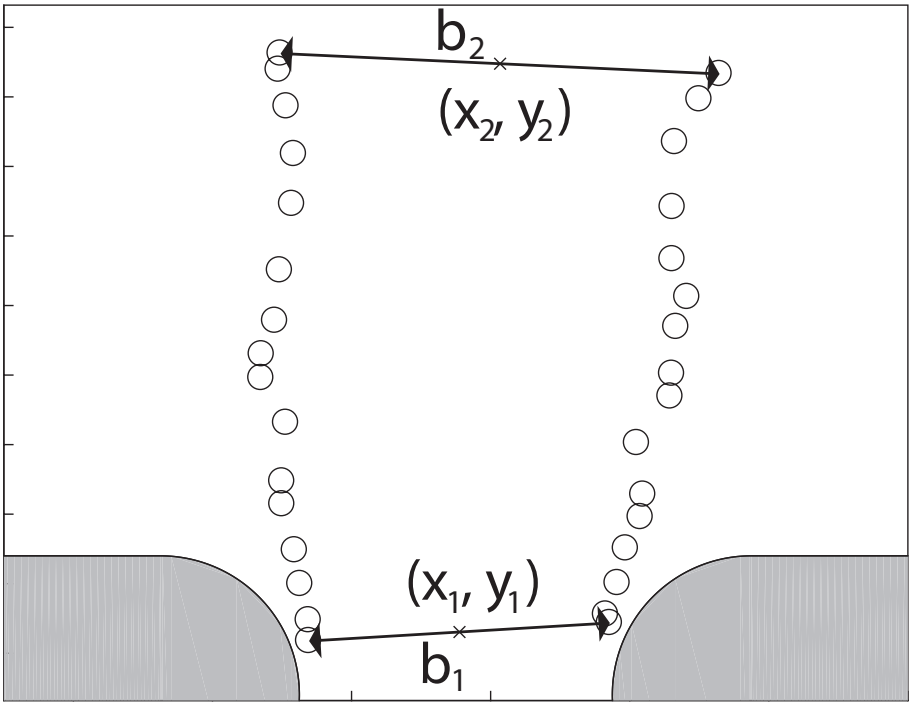

Figure 14. A sketch illustrating the dipole tracking. x_1 and y_1 is the position of the midpoint between the two vortices, and b1 is the distance between the two vortices at separation time, $t = T_s$. Likewise, x_2, y_2, is the position on the midpoint between the vortices, and b_2 is the distance between the vortices at $t = T_s + \Delta t$.

Since the majority of the vorticity is contained within the core radius, scale analysis gives $\Gamma \simeq \pi a U$, which is obtained by assuming $\xi \simeq U/a$. This suggests that the dipole propagation velocity can be represented as

$$U_{dip} \simeq \alpha U, \tag{18}$$

where $\alpha = a/b$ is the aspect ratio of the vortices. The comparison to tracked velocities (Fig. 16b) shows that Eq. 18 is a good representation of the dipole propagation velocity.

The dipole propagation velocity is crucial when determining the transport properties of the dipole in relation to tidal pumping (Kashiwai, 1984a; Wells and van Heijst, 2003). In the next section we will use the simple relations found here in the search for a parameter describing the net water exchange through the strait.

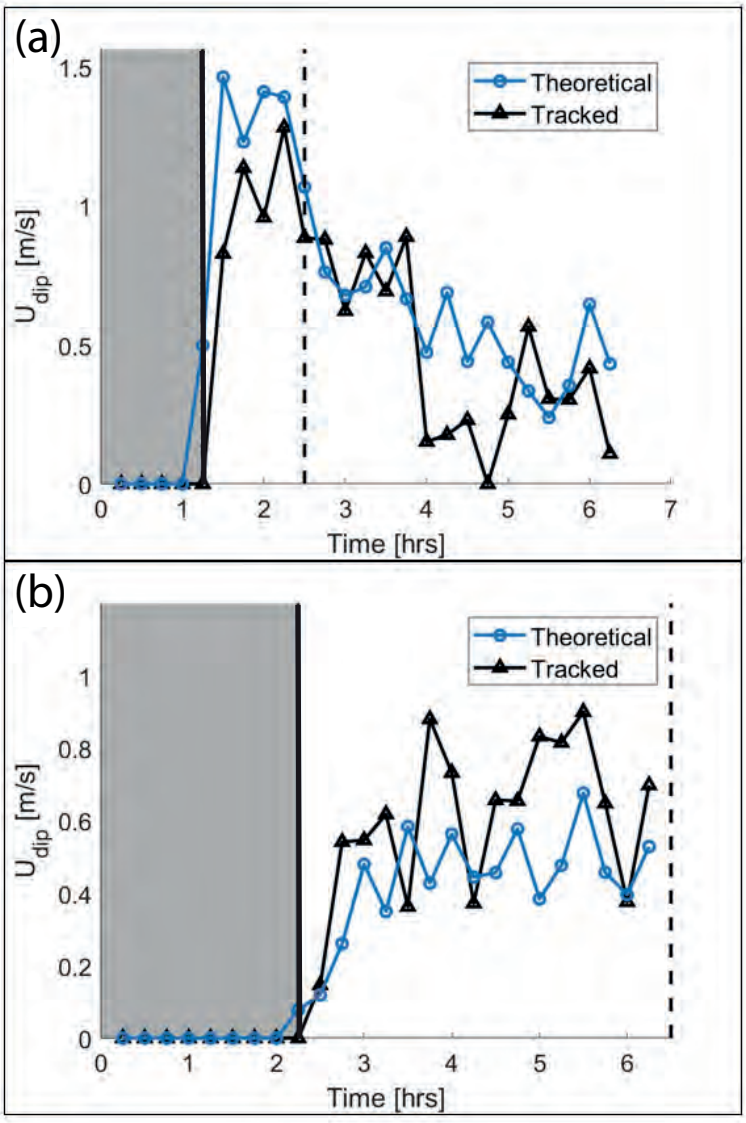

Figure 15. Dipole propagation velocity for a dipole formed in (a) the 1 km wide and 4 km long strait shown in Fig. 5, and (b) the 4.5 km wide and 4 km long strait shown in Fig. 6. The black curves are velocities obtained from dipole tracking, while the blue curves are velocities calculated using Eq. 15. The gray patch indicates the time before flow separation. The dashed black line indicates when the dipole escapes the sink region.

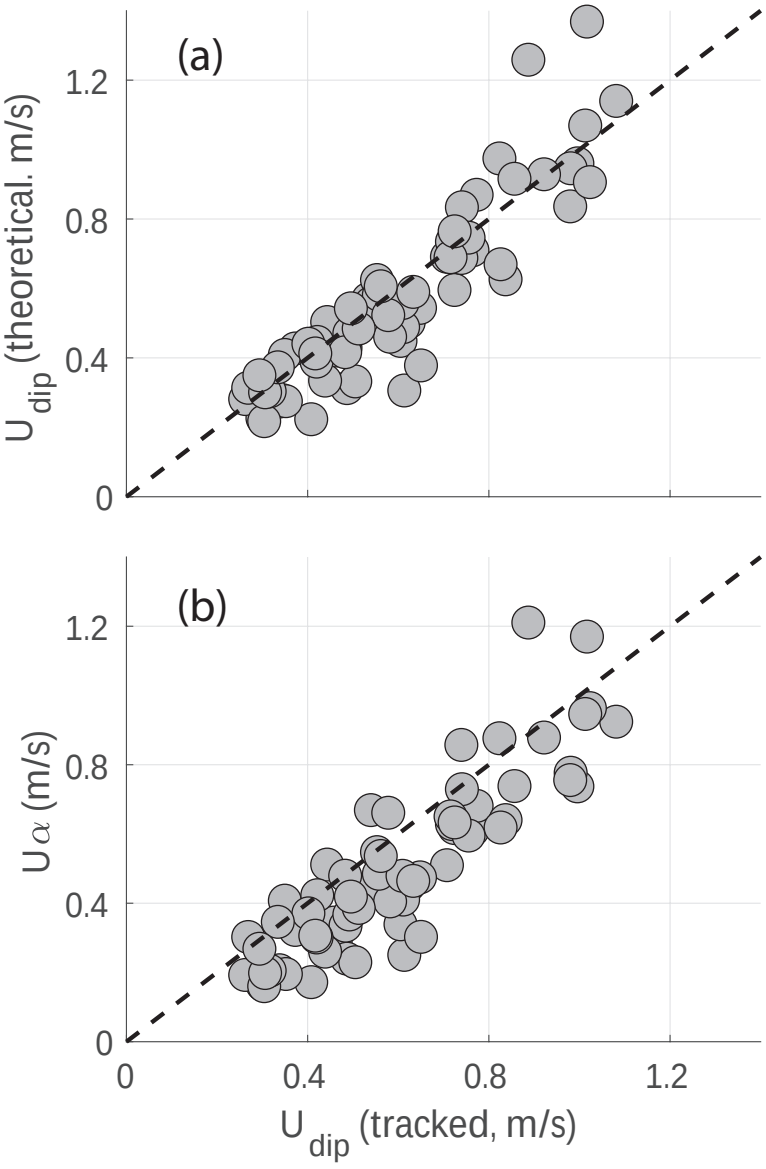

Figure 16. The dipole velocities obtained from tracking (on the x-axis) plotted against a) the theoretical dipole velocities (Eq. 15), and against $U\alpha$ (Eq. 18) in the lower panel. The tracked velocities, theoretical velocities and α are averaged over the time period when the dipole is located inside the sink region.

7 Water exchange through the strait

7.1 Effective tracer transport

To investigate the role of dipole vortices in generating net water exchange, we first quantify the effective tracer transport Q_e,

$$Q_e = \frac{Q_n}{Q_m}. \tag{19}$$

Q_e is the ratio between the net tracer transport Q_n and the maximum potential for net tracer transport through the strait Q_m, over the course of one tidal cycle. Q_n is calculated through a cross-section in the center of the strait ($y = y_e - L/2$) as

$$Q_n = \sum_{t=0}^{T} \sum_{n=1}^{N} c_n v_n dA_n dt. \tag{20}$$

Here v_n is the normal velocity through an area element dA_n, and c_n is the tracer concentration in grid cell n. Q_m is given by

$$Q_m = \sum_{t=0}^{T/2} \sum_{n=1}^{N} c_{max} v_n dA_n dt + \sum_{t=T/2}^{T} \sum_{n=1}^{N} c_{min} v_n dA_n dt. \tag{21}$$

The maximum possible tracer transport occurs when the northward transport consists entirely of water containing tracer concentration $c = c_{max}$, and the southward transport consists entirely of water containing tracer concentration $c = c_{min}$. In our case $c_{max} = 1\ m^{-3}$ and $c_{min} = 0\ m^{-3}$. The effective tracer transport is independent of the volume transport, and is a measure of how efficient water is exchanged through the strait.

7.2 Water exchange by self-propagating dipoles

The ability of the dipole to escape the return flow determines its contribution to water exchange through a strait (Kashiwai, 1984a; Wells and van Heijst, 2003). Both Kashiwai (1984a) and Wells and van Heijst (2003) investigated the dipole position relative to the sink region at flow reversal to evaluate the ability of the dipole to escape. While Kashiwai (1984a) only considered the position of the dipole relative to the sink region, Wells and van Heijst (2003) evaluated the strength of the return flow relative to the dipole velocity at its position. Both approaches resulted in a threshold value of the Strouhal number (St_c) between 0.8 and 0.13, separating the dipoles escaping ($St < St_c$) and dipoles not escaping ($St > St_c$) the return flow.

We follow the approach of Kashiwai (1984a) and investigate the dipole transport potential by evaluating the dipole propagation distance, L_d, relative to the sink radius, R_s, at $t = T/2$.

$$L_d = U_{dip} \left(\frac{T}{2} - T_s \right), \tag{22}$$

and R_s is given by

$$R_s = \sqrt{\frac{2Q}{\pi H}} = \frac{\sqrt{2WUT}}{\pi}, \tag{23}$$

where W is channel width, $Q \simeq WH \int_0^{T/2} v dt = WHUT/\pi$ is the tidal prism, and $v = Usin(\omega t)$ is the along-strait velocity. Here we assume the sink region is formed as a semi-circle, with a radius R_s, and the water depth H is constant inside the domain.

The position of the dipole relative to the sink radius at $t = T/2$ is evaluated by the non-dimensional parameter S_d,

$$S_d = \frac{R_s}{L_d} = \frac{\sqrt{2WUT}}{\pi U_{dip} \left(\frac{T}{2} - T_s \right)}. \tag{24}$$

This expression is formulated in the same fashion as the Strouhal number by Kashiwai (1984a) and Wells and van Heijst (2003), meaning that low numbers favor escaping dipoles and effective water exchange. If $S_d > 1$ the dipole is inside the sink region when the flow reverses, and conversely, if $S_d < 1$ the dipole is outside the sink region and will escape the return flow. S_d considers dipole transport properties only, and shows different behavior for the different strait lengths when plotted against effective tracer transport (Fig. 17a). Values of S_d well below one does not guarantee net tracer transports, as can be seen for some of the longest straits (Fig. 17a). This indicates that we need to consider the strait length in order to describe the effective tracer transport through the strait.

The dipole can only be an important contributor for water exchange if the strait is shorter than the tidal excursion. If the strait is longer than the tidal excursion, the water mass on one side of the strait will not be able to travel through the strait, with zero net tracer exchange as a result. In order to evaluate the effect of strait length we introduce the nondimensional length scale

$$S_L = \frac{L}{L_t} = \frac{\pi L}{U_m T}. \tag{25}$$

Here, $L_t = \int_0^{T/2} v_m dt$ is the tidal excursion and L is the strait length. $v_m = U_m sin(\omega t)$ is the cross-strait maximum tidal current, and U_m is the amplitude of v_m. We choose to use the maximum current in the estimation of L_t because this ensures that the net tracer transport is zero for $S_L > 1$. In this case the tracer front will not propagate through the strait during one half tidal cycle and no tracer will be available for the dipole to capture and transport away from the strait. This is the case for many of the long straits, with zero tracer transport as a result (Fig. 17b). However, similar as for S_d, $S_L < 1$ does not guarantee a net tracer transport.

S_L and S_d can be combined to give the effective tracer transport through the strait. To show this we consider the situation where $S_L < 1$, which assures that tracer will flow through the channel. We apply a simple kinematic model illustrated by Fig. 18. This Fig. shows the tracer distribution at $t = T/2$, where the dark gray represents the tracer in the dipole, the medium gray represents the tracer in the jet following the dipole and the light gray is the tracer inside the channel. All the tracer inside the channel and an unknown fraction of the tracer in the jet and dipole will be drawn back into the channel when the flow turns at $t = T/2$. We assume that the fraction inside the sink region will be drawn back, but this fraction depends on the shape of the dipole and jet, which is not easily estimated. However, to simplify the problem we assume that the dipole/jet is shaped like a rectangle, as illustrated by the green box in Fig. 18. The fraction inside R_s is now given by the lengths L_d, R_s and r_d only. We have introduced the distance r_d to include that parts of the dipole can escape even if $L_d < R_s$.

At $t = 0$ we assume that the tracer front is located on one side of the strait at $y = y_0$, and that the water transported into the strait at $y = y_0$ always has a tracer concentration equal to c_{max}. The tracer transported through the cross-section at $y = y_0$ between $t = 0$ and $t = T/2$ is given by $c_{max} W H L_t$. The tracer distribution at $t = T/2$ is divided between the strait, jet and dipole as illustrated in Fig. 18. This can be expressed as

$$WL_t = WL + WL_d + V_{dip}, \tag{26}$$

where V_{dip} represents the volume with tracer concentrations equal c_{max} in the dipole. H and c_{max} cancels since they appear on both sides of the equation. If the water that is drawn back maintains its tracer concentration c_{max} and the water that originates

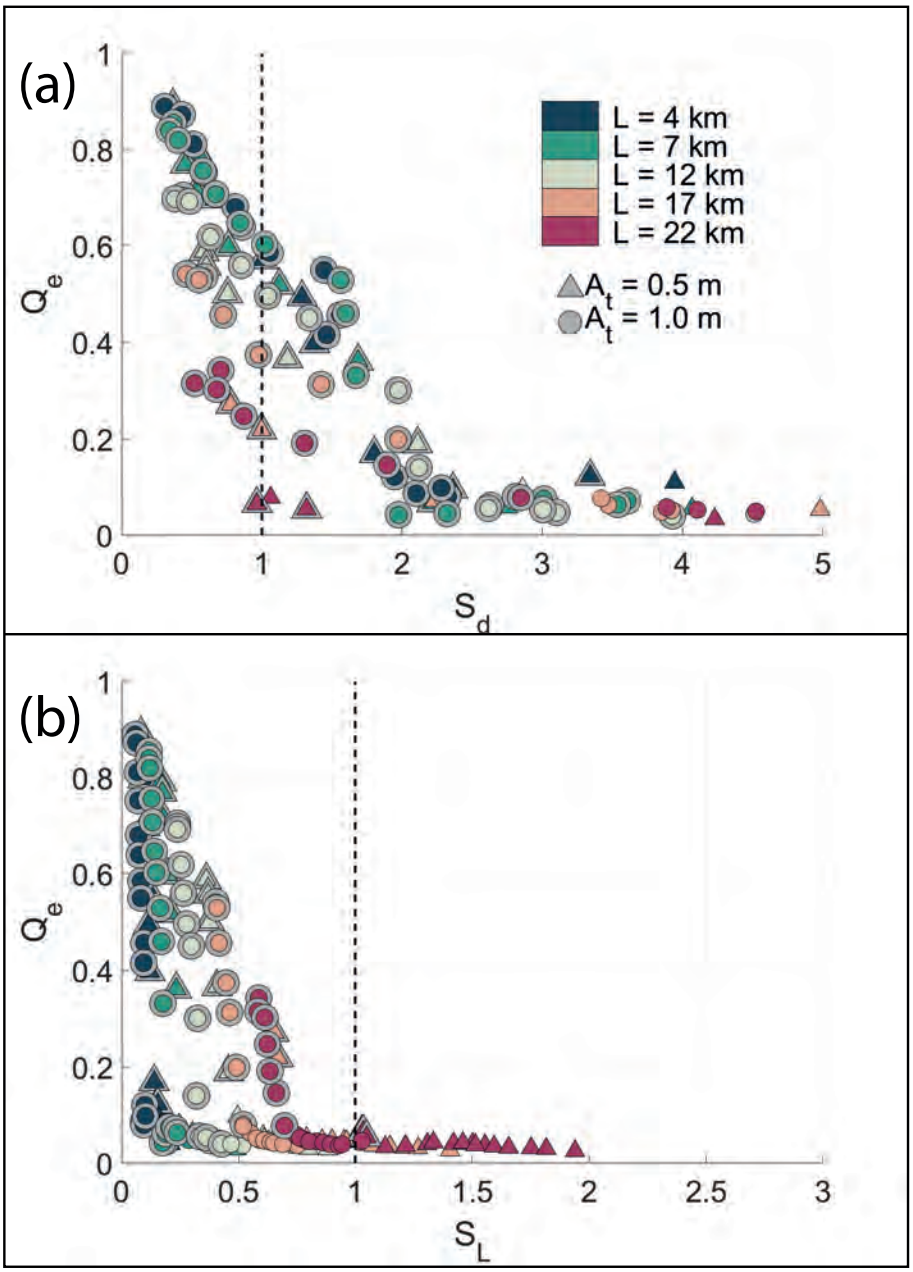

Figure 17. The effective transport, Q_e plotted against the non-dimensional parameters a) S_d and b) S_L. Dipoles, recognized from the criteria given in Section 5, are marked with a gray halo.

on the other side of the strait has a tracer concentration of c_{min}, the net tracer transport can be expressed as

$$q_n = \big(W(L_t - L) - \frac{R_s}{L_d + r_d}(WL_d + V_{dip})\big)c_{max} - \frac{L_d + r_d - R_s}{L_d + r}(WL_d + V_{dip})c_{min}. \quad (27)$$

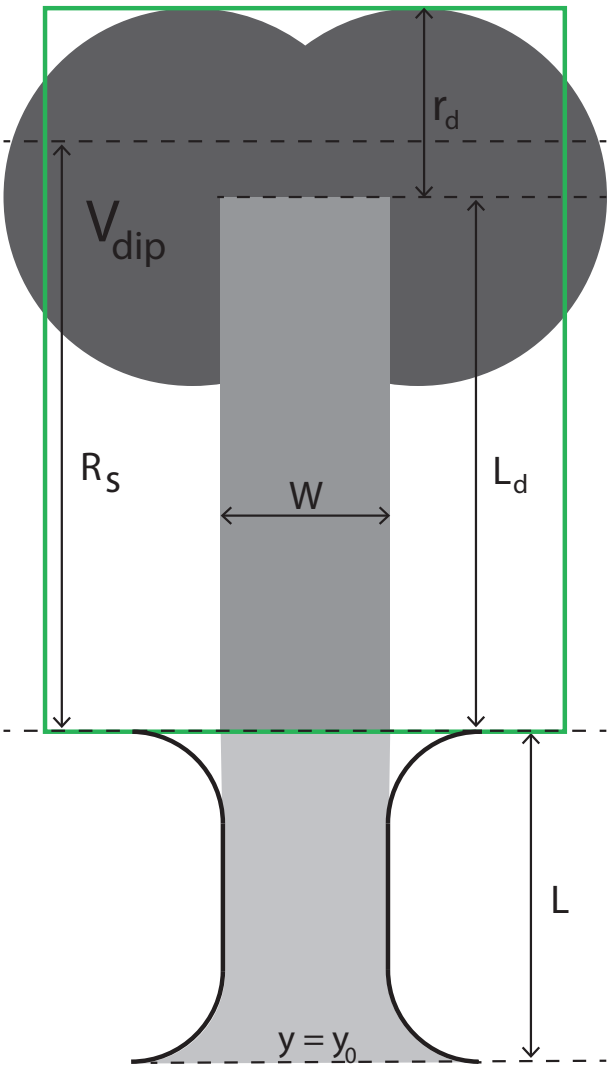

Figure 18. Idealized distribution of tracer at $t = T/2$ between the dipole (dark gray), jet (medium gray) and strait (light gray).

Here, we assume that the net volume flux during one tidal cycle is zero. Combining Eqs. 26 and 27 gives

$$q_n = W(L_t - L)(1 - \frac{R_s}{L_d + r_d})(c_{max} - c_{min}). \tag{28}$$

The maximum potential for tracer transport (see Eq. 21) is

$$q_m = W L_t (c_{max} - c_{min}). \tag{29}$$

Dividing Eq. 28 by q_m gives the effective tracer transport

$$q_e = (1 - S_L)(1 - \frac{S_d}{X_d}), \tag{30}$$

where X_d is given by

$$X_d = 1 + \frac{r_d}{L_d}. \tag{31}$$

Thus, using the simple kinematic model (Fig. 18), we can express the effective tracer transport in a simple combination of S_d and S_L, and the new parameter X_d. The result is shown in Fig. 19, where we plot q_e against Q_e for two different values of X_d. It is clear that X_d, which represent the size of the dipole, is vital to get a good fit between the kinematic model (Fig. 18) and the simulation results. For $X_d = 1$ (Fig. 19a), corresponding to $r_d = 0$, the fit between simulation results and kinematic model is not very good, although the kinematic model captures the main physics. However, using $X_d = 1.67$, collects the simulation results tightly around the line $Q_e = q_e$ (Fig. 19b).

8 Discussion

8.1 Sensitivity to mesh discretization

The resolution of our mesh varies from 50 m in the centre of the strait to 20 km at the outer boundary. The Rossby radius is ~ 230 km, and the northward propagating Kelvin wave should therefore be well represented in the model. The mesh resolution is more critical in the centre of the strait where vorticity and circulation are important parameters for vortex formation and dipole propagation. Vorticity is extremely sensitive to mesh resolution, and it is possible that the processes of separation and vortex formation is affected by the model resolution. In our case, the spatial scale of the initial vortices is close to the smallest scale the model can resolve. It is therefore important to investigate whether our conclusions regarding tracer transport, dipole propagation velocity and separation time are affected by the model resolution?

Vorticity is created in the velocity front formed by flow separation. The simulated vorticity in the velocity front depends strongly on model resolution. However, the total production of vorticity with time is less dependent on resolution. This can be shown by integrating the vorticity over an area containing a segment of the velocity front. During a time t, a velocity front with length Ut is formed, where U is the tidal velocity in the strait. Assuming that the velocity equals U on one side of the front and zero on the other, and that U is directed along the front gives (Kashiwai, 1984b)

$$\iint_{A_v} \nabla \times \boldsymbol{v} dA = \oint_C \boldsymbol{v} \cdot \boldsymbol{dl} \simeq U^2 t. \tag{32}$$

Here A_v is the area enclosing a segment of the front, C is the closed contour encircling A_v, $\boldsymbol{v}$ is the velocity vector and $\boldsymbol{dl}$ is an incremental length segment directed tangential to C. This result suggests that if the model resolution is sufficient to correctly represent the strait velocity and a flow separation, the total vorticity in a segment of the front is likely to be correct and independent of resolution. Since the vortices are formed from segments of the front, the total vorticity in the vortices and the circulation are likely to be similar between models of different resolution. Based on this analysis, we will argue that local vorticity is sensitive to mesh resolution, but the circulation is less sensitive to resolution as long as the model properly represents the strait velocity and a flow separation. Since dipole propagation velocity depends on the circulation of the vortices (Eq. 15), it is probably not very sensitive to mesh resolution.

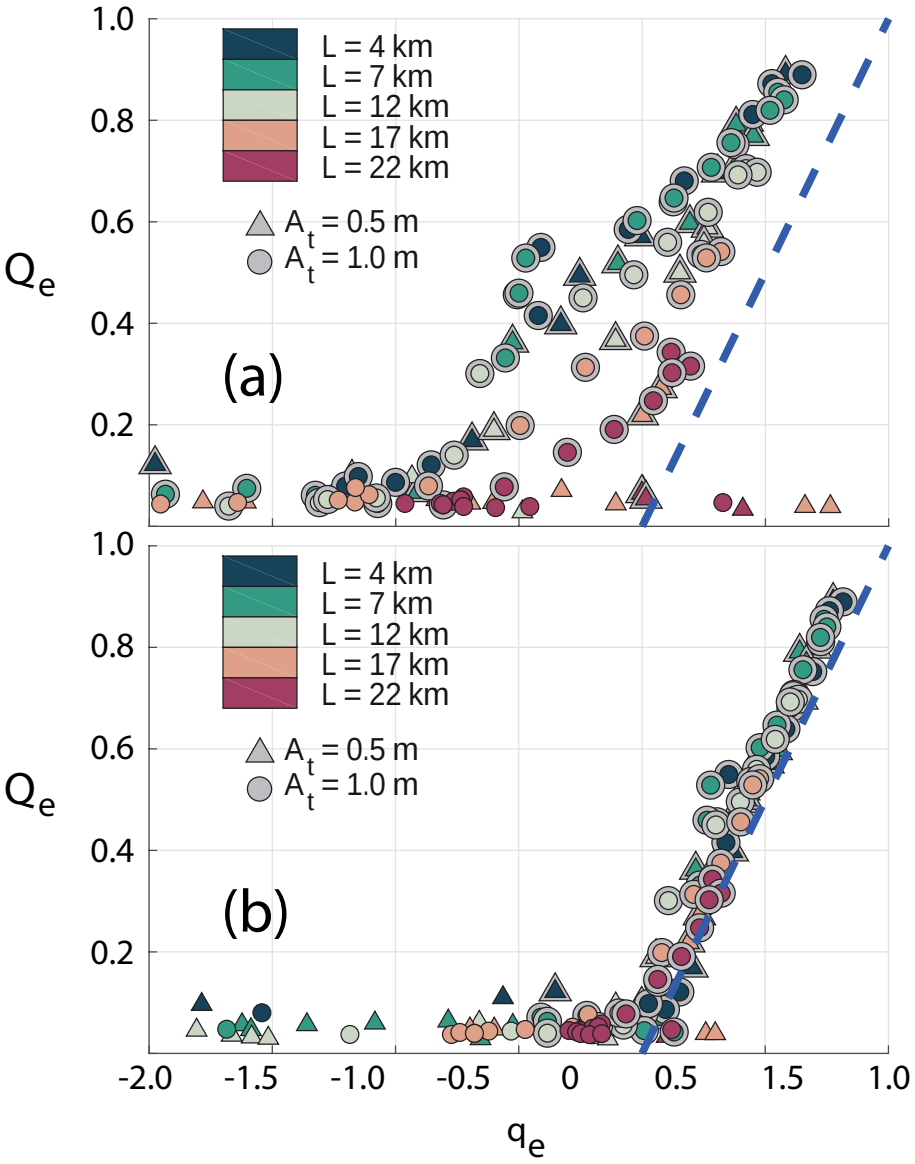

Figure 19. The effective transport Q_e from the simulations (Eq. 19) plotted against the effective transport resulting from the simple kinematic model (Eq. 30) for a) $X_d = 1$ and b) $X_d = 1.67$. The dashed line indicates $Q_e = q_e$. Dipoles, recognized from the criteria given in Section 5, are marked with a gray halo.

To study the effect of resolution, we have repeated a number of the simulations using finer mesh resolution. In the new simulations, the resolution at the coast is set to 10 m inside the strait. The other simulations presented in this paper has 50 m resolution at the coastline (see Section 2.2). We have selected 7 strait configurations which are simulated with higher resolution.

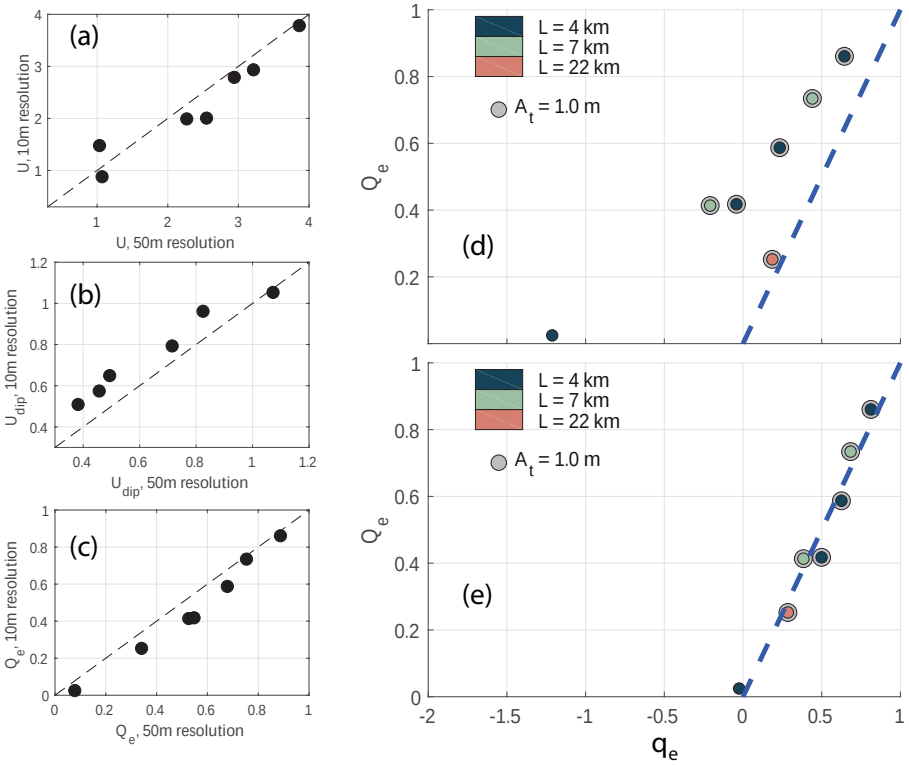

Figure 20. Comparison between 10m and 50m resolution simulations. a), b) and c) shows the comparison in velocity scale U, dipole propagation velocity U_{dip} and effective transport Q_e. d) and e) shows the effective transport Q_e (Eq. 19) from the finer resolution simulations plotted against the effective transport resulting from the simple kinematic model (Eq. 30) for d) $X_d = 1$ and e) $X_d = 1.67$. The dashed line indicates $Q_e = q_e$. Dipoles, recognized from the criteria given in Section 5, are marked with a gray halo.

These are the three simulations shown in Fig. 5 to 7 in the manuscript plus four others of different strait width and length. A comparison with the coarser simulations and final results for the simulations with 10 m resolution are shown in Fig. 20.

The strait velocities, dipole propagation velocities and the effective transports resulting from the high resolution simulations are all similar to the results from the coarser simulations (Fig. 20a-c), although dipole propagation velocities are slightly higher and effective transports are slightly lower for the new simulations. The effective transport shows similar agreement with results from the kinematic model (Fig. 20d and e) as the results from the 50m resolution simulations (Fig. 19). The simulated effective transports fit closely to the kinematic model results for $X_d = 1.67$. This shows that mesh discretization has little influence on the main conclusions of this paper.

Even if the velocity, dipole propagation and tracer transport is not very sensitive to mesh resolution, we clearly see that vorticity in the high resolution simulations reach larger values. Determining the separation time from the time of maximum vorticity is not a reliable method in the high resolution simulations. There is still a significant vorticity increase at the time of separation, but the maximum vorticity now typically occurs at the time of maximum strait velocity. The separation times

are therefore determined by visual inspection, and they are similar to the ones in the 50 m resolution simulations. Another interesting observation is that one side of the dipole may consist of two co-rotating vortices in the high resolution simulations, while it is a single vortex in the coarser simulations. The theoretical dipole propagation velocity (Eq. 15) still fits well to the tracked velocity if the circulation around both of the co-rotating vortices are considered.

8.2 Effect of strait length on flow dynamics

To understand why strait length is a restriction factor for dipole formation (Fig. 4), it is instructive to use the simplified model of Garrett and Cummins (2005). They consider the along strait velocity v as a function of time and position y along the strait. The equation governing the flow is,

$$\frac{\partial v}{\partial t} + v\frac{\partial v}{\partial y} = -g\frac{\partial \eta}{\partial y} - \frac{C_d}{H}|v|v, \tag{33}$$

where η is the surface elevation, C_d is the drag coefficient (Eq. 8) and H is depth. Scaling this equation using the velocity amplitude U as velocity scale, $T/2$ as time scale and the strait length L as length scale gives

$$2\frac{U}{T} + \frac{U^2}{L} \sim g\frac{\delta\eta}{L} - \frac{C_d}{H}U^2, \tag{34}$$

where $\delta\eta$ is the surface elevation difference between the exit and entrance of the strait. Our model setup is designed such that the difference in surface elevation across the strait is set by the tidal wave propagating around the peninsula and not by the strait flow. Due to this, $\delta\eta$ is treated as constant. From Eq. 34 it is clear that the pressure force and non-linear acceleration terms decreases with strait length, while the linear acceleration and friction are both independent of length. For $L < 10km$, the non-linear acceleration dominates the linear and frictional terms. When non-linear acceleration dominates, this will balance the pressure term which gives a velocity scale, $U \sim \sqrt{g\delta\eta}$. However, if either linear acceleration or friction balances the pressure force, the result is a velocity scale that decreases with length. Whether it is friction or linear acceleration that determines the length effect seen in Fig. 4 depends on the relation between these two terms. In our case, where $H = 100m$, $C_d \sim 0.001$ and $T \sim 45000$, the acceleration is about 4 times larger than the friction term for $U = 1m/s$. Therefore, it is mainly the linear acceleration that leads to the length effect seen in Fig. 4. For shallower depths it is likely that friction will cause a significant reduction in strait velocity. Smaller U requires narrower straits to obtain dipole formation, which explains the results shown in Fig. 4.

8.3 Dipole formation and flow separation

The dipole propagation velocity depends on the strength of the vortices set by their vorticity, and it is important to understand how the vorticity is generated. Wells and van Heijst (2003) assume that the vorticity is generated in the viscous boundary layer and injected into the vortices formed at the point of flow separation. Afanasyev (2006) introduces the "startup time", which is the time when the dipole starts propagating after an initial growth period being fed by the jet. Our simulations show a somewhat different picture. The dipole starts moving as soon as it is formed, and we see no initial period of growth (Fig. 15). The dipole is formed at separation time (Fig. 9), and before this we see no sign of vortices in the vorticity field (e.g. upper panel in Fig. 6).

The dipole formation is associated with a maximum in time of the absolute value of vorticity (Fig. 10). In the high resolution simulations presented in Section 8.1, flow separation does not occur at maximum vorticity, but is still associated with a sharp increase in vorticity. This is an interesting phenomenon and the question is whether the vorticity is a consequence of separation or if it plays an active role in causing the separation. Our results suggest that there is a buildup of vorticity before separation (Fig. 10), which indicates that the vorticity plays an active role in the separation process. The decrease in vorticity after separation might be connected to the roll-up of the velocity front creating the initial vortices. We see from our simulations, that the core radius of the vortices increases and the maximum vorticity decreases with time. Assuming it would take time to build up the vorticity before another vortex is formed fits with the picture of maximum absolute value of vorticity occuring at separation time. Buildup and shedding of vorticity is also observed to be important in controlling the separation point location of the flow around a wind turbine blade (Melius et al., 2018).

The velocity front rolls-up immediately after separation and creates the dipole vortices (Fig. 9). That the separated velocity front rolls up into a vortex is commonly observed in studies of flow separation (Délery, 2013), and that the velocity front is the origin of the vorticity was also proposed by Kashiwai (1984a, b). During a time T_* flow separation creates a velocity front of length UT_* and the velocity difference across the front is U. Using the same approach as in Eq. 32, we find that the circulation of the front is $\Gamma \simeq U^2 T_*$ (Kashiwai, 1984b). Using this together with Eq. 17 and 18 the timescale T_* can be expressed as

$$T_* = \frac{a\pi}{U}. \tag{35}$$

In our simulations, U varies between 1 and 4 m/s, and the initial core radius a is about 100 m for all simulations (Fig. 12. This gives a timescale T_* between one and five minutes. Thus, the initial vortices is created within one to five minutes after flow separation. Vorticity is injected into the dipole also after separation and the circulation in the dipole increases. However, the order of magnitude of the total increase in the circulation is roughly similar to the circulation in the initial vortices. Therefore, the circulation of the dipole is well below the maximum possible given by $\Gamma_{max} \approx U^2(\frac{T}{2} - T_s)$, which occurs if all vorticity created in the separated velocity front is injected into the dipole.

8.4 Dipole propagation velocity

As shown by Fig. 15 and 16, Eq. 15 is a good representation of the dipole propagation velocity. However, Eq. 15 gives a velocity that is twice as large as estimates obtained using Eq. 1. The aspect ratio of our simulated dipoles are mostly small ($\alpha \ll 1$) and the absolute maximum is about 0.5. For these aspect ratios Eq. 1 should be in good agreement with the simulated dipole velocities (Delbende and Rossi, 2009; Habibah et al., 2018), but instead the dipole propagation velocities are consistently twice as large. Recent work (Habibah et al., 2018) expresses the solution to the Navier Stokes equation in form of a power series in the aspect ratio. To first order the propagation velocity is given by our Eq. 1, and a correction to this only appears in the fifth order of the aspect ratio. In our case this correction should be small. Also, from Delbende and Rossi (2009) it appears that the propagation velocity actually decreases for increasing aspect ratio. Equation 1 gives the propagation velocity of a dipole moving in a non-moving ocean with no external forces acting on the dipole. These approximations are probably not valid in a

tidal strait, where a strong background flow is present and vorticity and momentum are injected into the dipole by the trailing jet. We suspect that this is the reason for the discrepancy between Eq. 1 and the tracked dipole velocities.

A derivation of propagation velocity for a dipole connected to a jet is presented by Afanasyev (2006). The budget of volume and momentum in the dipole leads to a propagation velocity equal to half the channel/jet velocity, in good agreement with observations. Afanasyev (2006) investigated a steady jet, but the mechanisms of momentum input from the jet to the dipole will apply also in our case of an oscillating tidal jet. We don't know the aspect ratio of the dipole studied by Afanasyev (2006), but it is not unlikely that it is around 0.5 and that his result therefore is in agreement with our result (Eq. 18). Equations 15 and 18 do not have a clear theoretical basis, but show good fit to our large ensemble of numerical simulations. Further studies of dipoles formed in tidal straits are needed to fully understand the propagation of these dipoles.

9 Summary and conclusion

In this study, we have performed a total of 164 numerical simulations of an ideal tidal strait, investigating flow separation, dipole formation and water exchange for different widths and lengths of the strait. We show that dipoles form and start propagating at the time of flow separation. The vorticity of the dipole vortices originates from the velocity front created by flow separation. The simulated dipole propagation velocity is twice as large as the propagation velocity derived for vortex pairs with no background flow (Lamb, 1916; Delbende and Rossi, 2009; Habibah et al., 2018) (Eq. 1). This is probably caused by injection of momentum into the dipole by the tidal jet (Afanasyev, 2006).

We derive two parameters S_d and S_L. S_d (Eq. 24) is given by the ratio between sink radius and distance travelled by the dipole, while S_L (Eq. 25) is given by the ratio between strait length and tidal excursion. For $S_L > 1$, the tracer will be contained within the strait through the whole tidal cycle and net transport is zero. For $S_d > 1$, the center of the dipole will be inside the sink region when the flow turns at $t = T/2$. However, since the dipole is of finite size a fraction of the dipole may still escape the return flow causing net tracer transport. From a simple kinematic model we show that the effective tracer transport can be expressed by S_d, S_L and a parameter X_d representing the dipole size relative to the sink region (Eq. 30 and 31). $1/X_d$ acts as a weight to S_d. Setting the value of X_d such that effective transports are zero for values of the weighted S_d larger than one, gives a remarkable good fit between the simple kinematic model and the numerical simulations (Fig. 19).

The kinematic model (Eq. 19) provides an understanding of the processes creating a net tracer transport through a tidal strait. In our idealized straits, the sink region is described by a half circle, the coastline curvature at the strait exit is kept constant and the strait is of uniform width. Along an irregular coast in the real world this will be different, but the physical processes will still be valid. An interested continuation of this study will be to derive S_d, S_L and X_d for a real coastline and investigate how well we can describe net tidal transports through straits.

Code availability. Model code is available at http://fvcom.smast.umassd.edu/fvcom/

Author contributions. Both authors have contributed equally

Competing interests. No competing interest are present

Acknowledgements. We thank P. E. Isachsen for constructuve scientific discussions and comments on the manuscript. E. Børve is funded by VISTA – a basic research program in collaboration between The Norwegian Academy of Science and Letters, and Equinor (project no. 6168). This work was supported by the Research Council of Norway (project no. 308796).

References

Afanasyev, Y. D.: Formation of vortex dipoles, Physics of Fluids, 18, https://doi.org/10.1063/1.2182006, 2006.

Albagnac, J., Moulin, F. Y., Eiff, O., Lacaze, L., and Brancher, P.: A three-dimensional experimental investigation of the structure of the spanwise vortex generated by a shallow vortex dipole, Environmental Fluid Mechanics, 14, 957–970, 2014.

Amoroso, R. O. and Gagliardini, D. A.: Inferring complex hydrographic processes using remote-sensed images: turbulent fluxes in the patagonian gulfs and implications for scallop metapopulation dynamics, Journal of Coastal Research, 26, 320–332, 2010.

Batchelor, G. K.: An introduction to fluid dynamics, 1967.

Brown, C. A., Jackson, G. A., and Brooks, D. A.: Particle transport through a narrow tidal inlet due to tidal forcing and implications for larval transport, Journal of Geophysical Research: Oceans, 105, 24 141–24 156, 2000.

Bruggeman, J. and Bolding, K.: A general framework for aquatic biogeochemical models, Environmental Modelling & Software, 61, 249–265, https://doi.org/10.1016/j.envsoft.2014.04.002, 2014.

Bryant, D. B., Whilden, K. A., A., S. S., and Chang, K.-A.: Formation of tidal starting-jet vortices through idealized barotropic inlets with finite length, Environmental Fluid Mechanics, 12, 301–319, https://doi.org/10.1007/s10652-012-9237-4, 2012.

Chadwick, D. B. and Largier, J. L.: The influence of tidal range on the exchange between San Diego Bay and the ocean, Journal of Geophysical Research: Oceans, 104, 29 885–29 899, 1999.

Chen, C., H., L., and Beardsley, R. C.: An Unstructured Grid, Finite-Volume, Three-Dimensional, Primitive Equations Ocean Model: Application to Coastal Ocean and Estuaries, Journal of Atmospheric and Oceanic Technology, 20, 159–186, http://dx.doi.org/10.5670/oceanog.2006.92, 2003.

Chen, C., Huang, H., Beardsley, R. C., Xu, Q., Limeburner, R., Cowles, G. W., Sun, Y., Qi, J., and Lin, H.: Tidal dynamics in the Gulf of Maine and New England Shelf: An application of FVCOM, Journal of Geophysical Research: Oceans, 116, 2011.

Chen, C., Gao, G., Zhang, Y., Beardsley, R. C., Lai, Z., Qi, J., and Lin, H.: Circulation in the Arctic Ocean: Results from a high-resolution coupled ice-sea nested Global-FVCOM and Arctic-FVCOM system, Progress in Oceanography, 141, 60–80, 2016.

Chen, C., Lin, Z., Beardsley, R. C., Shyka, T., Zhang, Y., Xu, Q., Qi, J., Lin, H., and Xu, D.: Impacts of sea level rise on future storm-induced coastal inundations over Massachusetts coast, Natural Hazards, pp. 1–25, 2021.

Delbende, I. and Rossi, M.: The dynamics of a viscous vortex dipole, Physics of Fluids, 21, 073 605, 2009.

Délery, J.: Three-dimensional separated flow topology: critical points, separation lines and vortical structures, John Wiley & Sons, 2013.

Ford, J. R., Williams, R. J., Fowler, A. M., Cox, D. R., and Suthers, I. M.: Identifying critical estuarine seagrass habitat for settlement of coastally spawned fish, Marine Ecology Progress Series, 408, 181–193, 2010.

Fujiwara, T., Nakata, H., and Nakatsuji, K.: Tidal-jet and vortex-pair driving of the residual circulation in a tidal estuary, Continental Shelf Research, 14, 1025 – 1038, https://doi.org/https://doi.org/10.1016/0278-4343(94)90062-0, 1994.

Galperin, B., Kantha, L., Hassid, S., and Rosati, A.: A quasi-equilibrium turbulent energy model for geophysical flows, Journal of the atmospheric sciences, 45, 1988.

Garrett, C. and Cummins, P.: The power potential of tidal currents in channels, Proceedings of the Royal Society of London A: Mathematical, Physical and Engineering Sciences, 461, 2563–2572, 2005.

Gill, A. E.: Atmosphere-ocean dynamics, Int. Geophys. Ser., 30, 662p, 1982.

Habibah, U., Nakagawa, H., and Fukumoto, Y.: Finite-thickness effect on speed of a counter-rotating vortex pair at high Reynolds numbers, Fluid Dynamics Research, 50, 031 401, 2018.

Kashiwai, M.: Tidal Residual Circulation Produced by a Tidal Vortex. Part 1. Life-History of a Tidal Vortex, Journal of the Oceanographical Society of Japan, 40, 279–294, 1984a.

Kashiwai, M.: Tidal residual circulation produced by a tidal vortex. Part 2. Vorticity balance and kinetic energy, Nippon Kaiyo Gakkai-Shi, 40, 437–444, 1984b.

Kundu, P. K.: Fluid Mechanics, Academic Press, 1990.

Lai, Z., Ma, R., Gao, G., Chen, C., and Beardsley, R. C.: Impact of multichannel river network on the plume dynamics in the Pearl River estuary, Journal of Geophysical Research: Oceans, 120, 5766–5789, 2015.

Lai, Z., Ma, R., Huang, M., Chen, C., Chen, Y., Xie, C., and Beardsley, R. C.: Downwelling wind, tides, and estuarine plume dynamics, Journal of Geophysical Research: Oceans, 121, 4245–4263, 2016.

Lamb, H.: Hydrodynamics (706 pp.), 1916.

Leweke, T., Le Diz'es, S., and Williamson, C. H. K.: Dynamics and Instabilities of Vortex Pairs, Annu. Rev. Fluid Mech., 48, 1–35, https://doi.org/10.1146/annurev-uid-000000-000000, 2016.

Li, C., Huang, W., Chen, C., and Lin, H.: Flow Regimes and Adjustment to Wind-Driven Motions in Lake Pontchartrain Estuary: A Modeling Experiment Using FVCOM, Journal of Geophysical Research: Oceans, 123, 8460–8488, 2018.

Melius, M. S., Mulleners, K., and Cal, R. B.: The role of surface vorticity during unsteady separation, Physics of Fluids, 30, 045 108, 2018.

Mellor, G. L. and Yamada, T.: Development of a turbulence closure model for geophysical fluid problems, Reviews of Geophysics, 20, 851–875, 1982.

Nicolau del Roure, F., Socolofsky, S. A., and Chang, K.-A.: Structure and evolution of tidal starting jet vortices at idealized barotropic inlets, Journal of Geophysical Research, 114, https://doi.org/10.1029/2008JC004997, 2009.

Signell, R. P. and Geyer, R.: Transient Eddy Formation Around Headlands, Journal of Geophysical Research, 96, 2561–2575, 1991.

Smagorinsky, J.: General circulation experiments with the primitive equations: I. The basic experiment, Monthly weather review, 91, 99–164, 1963.

Stommel, H. and Farmer, H. G.: On the nature of eustarine circulation, techreport 52-88, 131, WHOI, 1952.

Sun, Y., Chen, C., Beardsley, R. C., Ullman, D., Butman, B., and Lin, H.: Surface circulation in Block Island Sound and adjacent coastal and shelf regions: A FVCOM-CODAR comparison, Progress in Oceanography, 143, 26–45, 2016.

van Heijst, G.: Shallow flows: 2D or not 2D?, Environmental Fluid Mechanics, 14, 945–956, 2014.

Vouriot, C. V., Angeloudis, A., Kramer, S. C., and Piggott, M. D.: Fate of large-scale vortices in idealized tidal lagoons, Environmental Fluid Mechanics, 19, 329–348, 2019.

Wells, M. G. and van Heijst, G.-J. F.: A model of tidal flushing of an eustary by dipole formation, Dynamics of Atmospheres and Oceans, 37, 223–244, https://doi.org/10.1016/j.dynatmoce.2003.08.002, 2003.

Yehoshua, T. and Seifert, A.: Empirical Model for the Evolution of a Vortex-Pair Introduced into a Boundary Layer, AerospaceLab, pp. p. 1–12, https://hal.archives-ouvertes.fr/hal-01184646, 2013.

Zhang, Y., Chen, C., Beardsley, R. C., Gao, G., Lai, Z., Curry, B., Lee, C. M., Lin, H., Qi, J., and Xu, Q.: Studies of the Canadian Arctic Archipelago water transport and its relationship to basin-local forcings: Results from AO-FVCOM, Journal of Geophysical Research: Oceans, 121, 4392–4415, 2016.

Paper II

II

Rectified tidal transport in Lofoten-Vesterålen, Northern Norway

Eli Børve, Pål Erik Isachsen and Ole Anders Nøst
Ocean sciences, *in review*
doi:10.5194/os-2021-41

https://doi.org/10.5194/os-2021-41
Preprint. Discussion started: 26 May 2021

Ocean Science Discussions

Rectified tidal transport in Lofoten-Vesterålen, Northern Norway

Eli Børve[1,2], Pål Erik Isachsen[1,3], and Ole Anders Nøst[4,5]

[1]Department of Geosciences, University of Oslo, 0315 Oslo, Norway
[2]Akvaplan-niva AS, 9296 Tromsø, Norway
[3]The Norwegian Meteorological Institute, 0371 Oslo, Norway
[4]Faculty of Biosciences and Aquaculture, Nord University, 8026 Bodø, Norway
[5]Akvaplan-niva AS, 7462 Trondheim, Norway

Correspondence: Eli Børve (elb@akvaplan.niva.no)

Abstract. Vestfjorden in Northern Norway, a major spawning ground for the Northeast Arctic cod, is sheltered from the continental shelf and open ocean by the Lofoten-Vesterålen archipelago. The archipelago, however, is well known for hosting strong and vigorous tidal currents in its many straits, currents that can produce significant time-mean tracer transport from Vestfjorden to the shelf outside. We use a purely tidally-driven unstructured-grid ocean model to look into nonlinear tidal dynamics and the associated tracer transport through the archipelago. Of particular interest are two processes: tidal pumping through the straits and tidal rectification around islands. The most prominent tracer transport is caused by tidal pumping through the short and strongly nonlinear straits Nordlandsflaget and Moskstraumen near the southern tip of the archipelago. Here tracers from Vestfjorden are transported tens of kilometers westward out on the outer shelf. Further north, weaker yet notable tidal pumping also takes place through the longer straits Nappstraumen and Gimsøystraumen. The other main transport route out of Vestfjorden is south of the island of Røst. Here the transport is primarily due to tracer advection by rectified anticyclonic currents around the island. There is also an anticyclonic circulation cell around the islands of Mosken-Værøy, and both cells have have flow speeds up to 0.2 m/s, magnitudes similar to the observed background currents in the region. These high-resolution simulations thus emphasize the importance of nonlinear tidal dynamics for transport of cod eggs and larvae in the region.

1 Introduction

Increased industrial activity along the Norwegian coast rises concern about potential impacts on the marine ecosystem. To properly assess risks involved, we need to understand oceanic dynamics in near-shore regions and its associated transport of nutrients and pollutants. Together with wind and freshwater run-off, tides often dominate the flow dynamics in coastal regions. While strong tidal currents are known to cause efficient vertical mixing of the ocean, important for bringing up nutrients to the surface and ventilating the coastal seas, their contribution to net horizontal transport is often underestimated due to their oscillating nature. However, when strong tidal currents interact with complex topography in shallow waters, nonlinear flow dynamics can produce significant time-mean lateral transport (Huthnance, 1973; Parker, 1991).

https://doi.org/10.5194/os-2021-41
Preprint. Discussion started: 26 May 2021

In this study we will investigate nonlinear tidal dynamics around Lofoten-Vesterålen in Northern Norway (Figure 1), a major spawning ground for the Northeast Arctic cod (Hjermann et al., 2007). Spawning of this species takes place all along the middle and northern Norwegian coast, but as much as 40 percent of the cod spawns in Vestfjorden southeast of the Lofoten-Vesterålen archipelago (Ellertsen et al., 1981; Sundby and Bratland, 1987). The cod eggs and larvae spend the first five months drifting with the ocean currents from Vestfjorden to nursing grounds in the Barents Sea (Ådlandsvik and Sundby, 1994), and the survival rate during this initial pelagic drift is crucial for the recruitment of the fish stock (Hjort, 1914; Houde, 2008). Therefore a good understanding of drift and spreading patterns of the cod eggs and larvae is important for identifying particularly vulnerable regions and factors controlling the recruitment of the Northeast Arctic cod.

The majority of studies on transport of Northeast Arctic cod eggs and larvae have focused on flow dynamics on the Norwegian shelf where the Norwegian Coastal Current (NCC) and Norwegian Atlantic current (NwAC) quickly transport the cod larvae northeastward and into the Barents Sea (e.g. Ådlandsvik and Sundby, 1994; Vikebø et al., 2007; Opdal et al., 2008). The transport out of Vestfjorden itself has been reported to mainly take place around the southern tip of the Lofoten-Vesterålen archipelago (Vikebø et al., 2007; Opdal et al., 2008), following the larger-scale background currents, notably the NCC, and currents that respond to sporadic wind events. But by including stokes drift by wind-generated surface gravity waves, Röhrs (2014) and Röhrs et al. (2014) found that particles were transported closer to the coast and that the many straits which cut through the archipelago might be of larger importance than previously assumed.

The straits are well known for hosting strong and vigorous tidal currents. This includes a set of narrow and relatively long straits along the northern half of the archipelago, but even more so 2–3 wider but short straits over the shallow ridge southwest of Lofotodden (Moe et al., 2002). Here, near the southern tip of Lofoten, Moskstraumen is situated, also called the Lofoten maelstrom and famous for its vigorous and deadly currents. For the interested reader, tales, stories and observations of the Lofoten maelstrom can be traced all the way back to the medieval ages (see Gjevik et al., 1997). It seems clear that the vigorous tidal transport and dispersion around Moskstraumen in particular, but also in other straits of Lofoten, can impact the net exchanges between Vestfjorden and the shelf outside. Existing studies have focused on quantifying tidal dispersion rates (Lynge et al., 2010) and on establishing a link between tidal dispersion and transport by time-mean currents (Ommundsen, 2002). There has, however, been less attention put on identifying and quantifying the underlying non-linear dynamics responsible for tidal dispersion and transport. Two such nonlinear processes that are likely to be important in our region, and will therefore be the focus of the present study, are tidal pumping and tidal rectification.

Tidal pumping in a strait is a Reynolds flux of properties caused by a temporal asymmetry in circulation patterns between the flood and ebb phases of the tide (Geyer et al., 2001). The process can be explained using the simple model by Stommel and Farmer (1952), who were the first to investigate this phenomenon. When tidal currents enter a strait, say from the open ocean side, we expect them to behave roughly as potential flow and be steered by the coastline into the opening. So waters from a wide region around the opening, the 'sink region', is pulled into the strait. In contrast, when the flow exits the strait during the subsequent phase of the tide, the joint effect of friction and an adverse nonlinear pressure gradient as the strait opens up might cause the flow to separate from the coastline (Kundu et al., 2016). If there is such flow separation, the exiting water will continue straight ahead as a tidal jet. The areas covered by the sink region and the tidal jet are equally large, but they clearly

https://doi.org/10.5194/os-2021-41
Preprint. Discussion started: 26 May 2021

Ocean Science
Discussions
Open Access
EGU

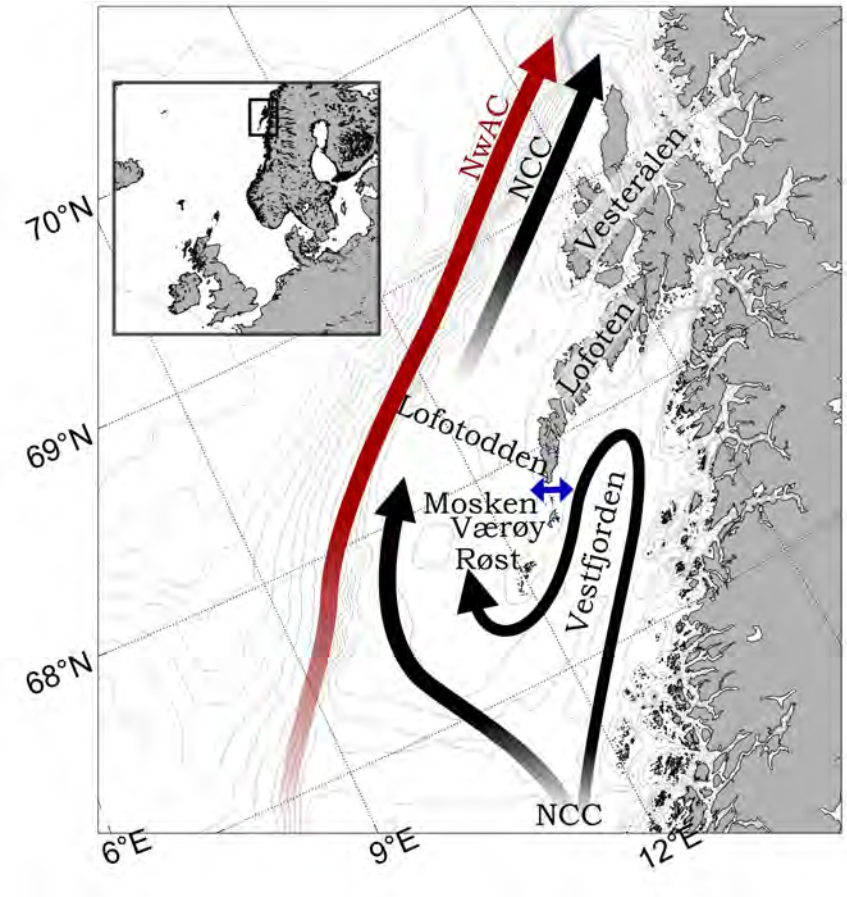

Figure 1. The general ocean surface circulation in the Lofoten-Vesterålen region. Black arrows show the Norwegian Coastal Current (NCC) and the red arrow shows the Norwegian Atlantic Current (NwAC). The blue two-headed arrow show the location of Moskstraumen, situated between Lofotodden to its north and the small island Mosken to its south.

take on different shapes. Some regions are overlapping while others are not. The existence of non-overlapping regions will cause some difference in what waters flow into and out of the strait. More recent studies have found that the presence of a tidal jet on outflow from a strait is intimately related to the formation of self-propagating dipoles at the strait exit (Wells and van Heijst, 2003; Afanasyev, 2006; Nøst and Børve, 2021). The dipoles emerge from vortices that form at the points where the flow separates from the coastline, one at each side of the strait exit. The vortices become a self-propagating dipole when the strait is narrow enough for the two to interact, so that the velocity field of one vortex begins to advect the vorticity of the other. This self-propagating dipole is then trailed by the tidal jet. As it turns out, most of the water that exits the strait is injected into the dipole and its trailing jet (Nøst and Børve, 2021). Therefore, if the dipole avoids being drawn back into the strait during the subsequent potential flow phase of the tide, the result will be a net property exchange through the strait (Kashiwai, 1984; Wells and van Heijst, 2003; Nøst and Børve, 2021).

https://doi.org/10.5194/os-2021-41
Preprint. Discussion started: 26 May 2021

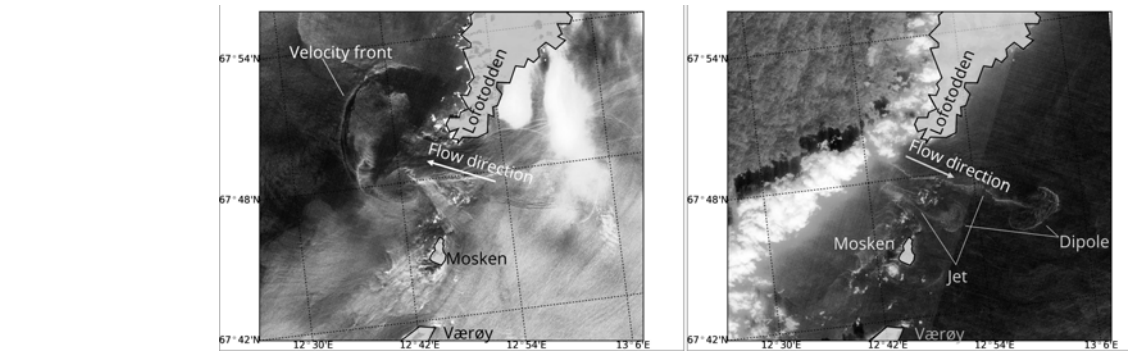

Figure 2. Satellite images from Copernicus Sentinel-II missions showing the surface currents in Moskstraumen and Nordlandsflaget.The Sentinel-II missions satellites carry a multi-spectral instruments with 13 spectral channels in the short wave infrared and visible/near infrared spectral range, whereas this image is collected from band B4 (664.6 nm). The satellite imagery was assessed and processes using data from the Norwegian National Ground Segment for Sentinel data (Halsne et al., 2019, pers. comm. Trygve Halsne).

The second process, rectification of oscillating currents around isolated islands and banks, has been observed in several regions where cross-slope tidal currents are prominent. The phenomenon can be explained as a response to a nonlinear momentum transport convergence by the oscillating currents (Huthnance, 1973; Loder, 1980) or, alternatively, a net cross-slope vorticity flux by the same oscillations (Zimmerman, 1978; Robinson, 1981). The generation of a net vorticity flux can be understood by imagining following a water column that moves periodically up and down the topographic slope of a bank, driven by a large-scale tidal potential (Zimmerman, 1978, 1981). In the northern hemisphere, the column attains negative vorticity on its way up the slope and positive vorticity on its way down due to vortex squeezing and stretching, respectively. Bottom friction then removes some negative vorticity from the column over shallow regions and some positive vorticity over deep regions. A sustained oscillation, driven by the large-scale tidal potential, will hence be associated with a positive vorticity flux from shallow to deep regions. In a quasi-steady state, the vorticity flux from many such columns may be balanced by bottom friction acting on a time-mean anti-cyclonic circulation around the bank. Additionally, a net vorticity flux across a sloping bottom can be generated by differential bottom friction acting on water columns that are made to oscillate *along* the sloping bottom (Zimmerman, 1978; Loder, 1980; Pingree and Maddock, 1985; Maas et al., 1987). In this case the direction of the vorticity flux will depend on the orientation of the tidal ellipses relative to topography, but the end result will also be time-mean currents around island and banks.

Indication of large dipole vortices associated with tidal currents have been observed in satellite images from Moskstraumen (see e.g. Figure 2), indicating that at least tidal pumping may be of importance in the Lofoten-Vesterålen region. The rectification of tidal currents has not, to our knowledge, been observed or studied before in this region. But strong tidal oscillations around the islands of Mosken, Værøy and Røst off the southern tip of the archipelago suggest that this is a process worth investigating. In the presence of interactions with smaller-scale non-conservative flow dynamics, such time-mean circulation

https://doi.org/10.5194/os-2021-41
Preprint. Discussion started: 26 May 2021

cells may very well act as 'gears' that transport cod eggs and larvae, as well as nutrients and pollutants, between Vestfjorden and the outer shelf.

In this paper we will isolate these two potential transport mechanisms by conducting and analysing a purely tidally-forced numerical simulation of the region. Modeling non-linear tidal dynamics in such a complex region is challenging. Lynge et al. (2010) found that modelled tidally-driven transport through Moskstraumen is highly dependent on the model grid resolution and that a horizontal resolution down to 50–100 m is required to resolve key non-linear dynamics and thus obtain realistic transport estimates. This resolution in much higher than what is typically used in e.g. operational transport models of the region. Our approach to this practical problem is to use an unstructured grid model which allows very high resolution in straits where nonlinear tidal dynamics is thought to be important. At the same time the flexible mesh allows us to reduce resolution away from complex geometry, thus enabling us to run simulations over a large enough domain to provide a good representation of the northward propagating tidal waves. The model setup and a validation against available observations are summarized in section 2. The two dynamical processes are then discussed separately in section 3. Finally, a brief summary of results in section 4 wraps up the study.

2 Model description

We use the Finite Volume Community Ocean Model (FVCOM Chen et al., 2003), for modelling tidal flows in the Lofoten-Vesterålen region. FVCOM is a prognostic, free-surface, three-dimensional primitive equation ocean model which solves the integral form of the equations on an unstructured triangular horizontal grid and a terrain-following vertical grid. For this study of lateral transport dynamics we used a two-dimensional version of FVCOM, leaving out buoyancy effects. The model calculates momentum advection using a second-order accuracy flux scheme (Chen et al., 2013; Kobayashi et al., 1999), horizontal diffusion of momentum by the Smagorinsky closure scheme (Smagorinsky, 1963) and quadratic bottom friction using a depth-dependent drag coefficient. The governing equations are integrated in time using a modified explicit forth-order Runga-Kutta time stepping scheme (Chen et al., 2013).

The model domain, with coastline and bottom depths, is shown in Figure 3. The unstructured triangular grid enables us both to resolve small-scale nonlinear flow dynamics near land as well as the large-scale behavior of the tidal waves. Along the coast the grid resolution is as high as 30–50 meters, which provides us with a minimum of five grid cells across the narrowest cross-sections inside straits and inlets. Most straits are, however, resolved with more that five grid cells, as illustrated by Nappstraumen in the right panel of Figure 3. Such high resolution near land allows us to model flow separation and the development of eddies, which are important processes for generating nonlinear tidal transports. The grid resolution decreases monotonically away from land and steep topography, down to around 5 km along the open boundary away from the coastline.

Along the open boundary, we force the model with prescribed sea surface height (SSH) anomalies due to northward-propagating tidal waves. We obtain the SSH forcing fields from the TPXO 7.2 assimilated tidal model (Egbert and Erofeeva, 2002) from which we include all major constituents. The surface elevation is specified at the boundary nodes. Velocities in FV-

https://doi.org/10.5194/os-2021-41
Preprint. Discussion started: 26 May 2021

Ocean Science
Discussions
Open Access
EGU

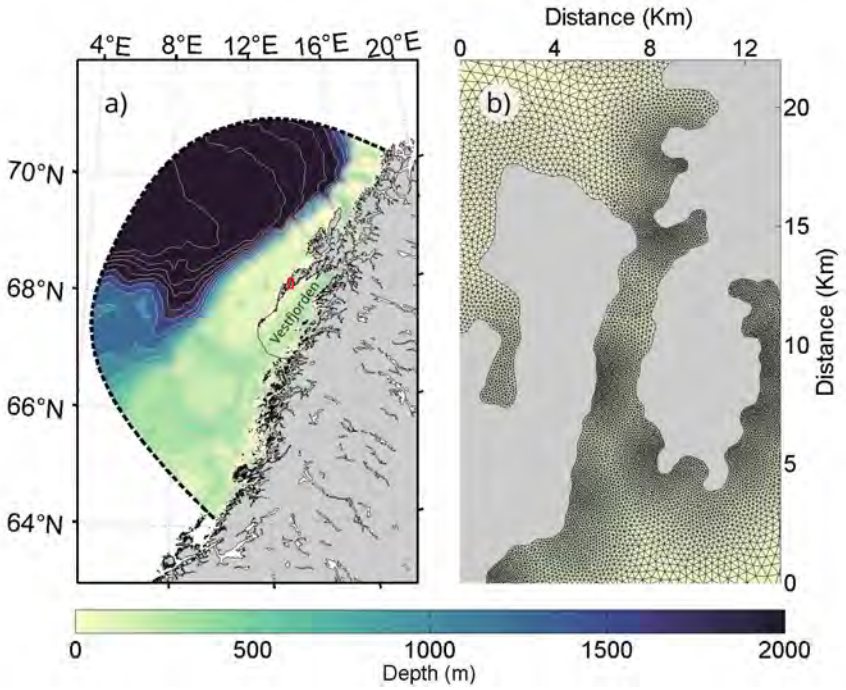

Figure 3. The model domain for the unstructured-grid modeling. The left panel a) shows the bathymetry inside the model domain. The dotted thick black line shows the outer open boundary of the model. The thin black line bordering Vestfjorden outlines the boundary of the region where we release a tracer. The right panel b) shows an example of the varying triangular grid resolution near Nappstraumen, highlighted by the red rectangle in the left panel.

COM are calculated in the center of each triangular cell, and not directly at the boundary. The velocities in the open boundary cells are calculated based on the assumption of mass conservation (Chen et al., 2003, 2011).

We spin the dynamics of FVCOM up for six months before analyzing the model fields. In order to investigate tidal transport dynamics, we couple FVCOM with a passive tracer module, the Framework for Aquatic Biogeochemical Models (FABM Bruggeman and Bolding, 2014). After the six-month spin-up period, we release a passive tracer of concentration $1\ \mathrm{m}^{-3}$ inside Vestfjorden (bounded by the thin black lines shown in the left panel of Figure 3). The tracer concentration is set to zero outside. After this initial tracer release, we run the coupled model for another two more months to ensure that we capture effects of the the spring-neap cycle.

2.1 Model validation

The large-scale behavior of the M2 and K1 tidal waves and associated currents are shown in Figure 4. The semi-diurnal M2 wave (left panels) is the dominating constituent in the region. The wave is scattered and deflected around the Lofoten archipelago. The fraction of the wave that enters Vestfjorden slows down and the SSH amplitude increases towards the head

https://doi.org/10.5194/os-2021-41
Preprint. Discussion started: 26 May 2021

of the fjord due to the geometry of the fjord. In contrast, the fraction of the wave that passes west of the archipelago speeds up along the narrowing shelf. The result is a small phase shift and a large difference in SSH amplitude between Vestfjorden and the outer side of the archipelago. This generates strong tidal currents in the straits (lower left panel). Particularly strong currents are found over the narrow and shallow ridge south of Lofotodden.

The K1 wave is the dominating diurnal constituent (right panels), but its amplitude in SSH is only about one tenth of the M2 amplitude. The K1 wave behaves similarly to the M2 wave inside Vestfjorden, and a gradient in SSH across the archipelago produces strong diurnal tidal currents as well through the straits (lower right panel). Interestingly, along the narrow outer shelf vest of the archipelago we observe that the K1 tidal current amplitude increases northward, particularly west of Vesterålen. For comparison, the M2 tidal current amplitude decreases in the same area. This prominent amplification of the diurnal tidal component, K1, has been attributed to the generation of diurnal continental shelf waves by Ommundsen and Gjevik (2000) and Moe et al. (2002).

The large-scale behavior of both M2 and K1 waves in our model corresponds well with results reported earlier by Gjevik et al. (1997) and Moe et al. (2002). Furthermore, the sea surface height and phase from the model fit reasonably well with observations from five stations provided by the Norwegian Mapping Authority, Hydrographic Service (2021), as shown in Figure 5. One notable exception is the phase of the K1 tide which is too small in the model compared to observations from Andenes, Kabelvåg and Harstad. The modeled tidal current amplitudes also agree well with observations (also shown in Figure 5c). Here we also observe that the K1 tidal current dominates in station 8, Sortlandssundet, which corresponds to the enhanced current velocities for the diurnal K1 tide in Vesterålen seen in the lower right panel of Figure 4. In general, we find that the overall performance of our FVCOM tidal simulation is acceptable, providing a good foundation for investigating tidal transport dynamics in the region.

3 Tidally-driven tracer transport in Lofoten

Figure 6 shows a three-day average of the tracer concentration near the end of the simulation period. We observe a pronounced net tracer exchange between Vestfjorden and the shelf outside, particularly south of Lofotodden. Water with tracer concentration exceeding $0.3\,\mathrm{m}^{-3}$ is transported tens of kilometers westward on the outer shelf from this southernmost region. We also observe notable tracer transports through the longer straits Nappstraumen (4) and Gimsøystraumen (5) somewhat further north. In contrast, only a very small amount of tracer appears to be transported through the long and narrow Raftsundet (6) and Tjeldsundet (7) even further to the northeast.

A visual comparison with Figure 4 suggest that the transport scales roughly with the intensity of tidal currents, but here we will have a closer look at the actual dynamics at play. As outlined above, the focus will be on two processes. The first is essentially a Reynolds 'pumping' of a passive tracer through straits, stemming from a correlation between fluctuations in the tidal velocity and fluctuations in tracer concentration. The the second is the generation of rectified currents around islands. We set out to clarify and summarize key theoretical aspects of each process as well as check their applicability in Lofoten-Vesterålen.

https://doi.org/10.5194/os-2021-41
Preprint. Discussion started: 26 May 2021

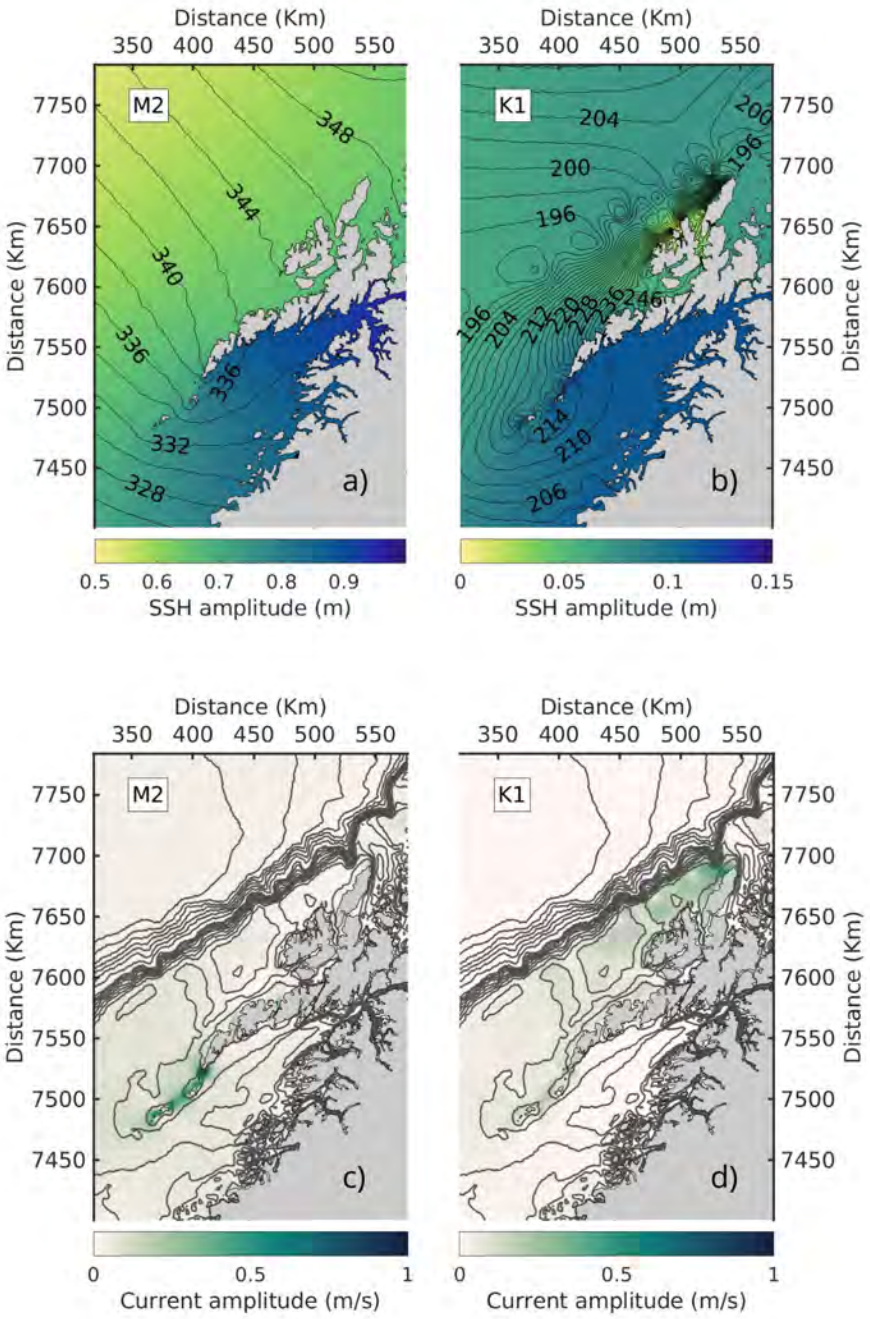

Figure 4. The M2 (left panels) and K1 (right panels) tide in the model. The upper panels show the amplitude (color) and phase (contours) of SSH for the two constituents. The lower panels show the magnitude of the major axis of tidal currents (colors) and bottom topography (contours).

https://doi.org/10.5194/os-2021-41
Preprint. Discussion started: 26 May 2021

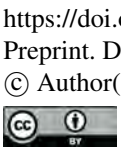

Ocean Science
Discussions
Open Access
EGU

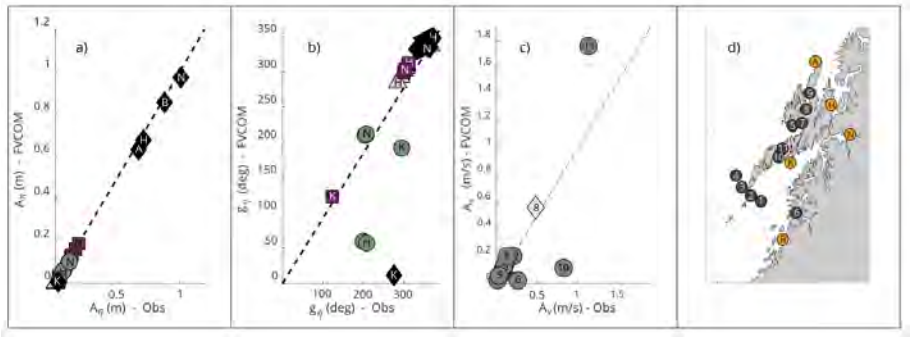

Figure 5. Comparison between modelled and observed tidal properties in Lofoten. Comparisons for the SSH tidal amplitude A_η and phase shift g_η are displayed in panel a) and in panel b), respectively, for five stations in Lofoten: Andenes (A), Harstad (H), Kabelvåg (K), Narvik (N) and Bodø (B), shown as orange markers in the right panel d). The different tidal constituents considered are M2 (black diamonds), K1 (green circles), N2 (purple squares) and S2 (gray triangles). The observations of SSH are collected from the Norwegian Mapping Authority, Hydrographic Service (2021). Panel c) shows the comparison between tidal current amplitude in the model and from observations collected from table 3 of Moe et al. (2002). In total we compare 11 stations in the Lofoten-Vesterålen region, shown as dark gray markers in the right panel d). We display the M2 tidal current amplitude from all stations, and in addition the K1 tidal current amplitude from station 8 (diamond) in Sortlandssundet, since this latter station is in a region where the diurnal tidal current (K1) is known to dominate.

3.1 Tidal pumping

Tidal pumping through a strait is a property exchange associated with zero net mass transport (i.e. a Reynolds flux) caused by a temporal asymmetric flow field between the ebb and the flood tide (Stommel and Farmer, 1952). The flow asymmetry arises where inflow to a strait takes the form of a broad potential flow whereas outflow is concentrated in a jet generated after flow separation. When the tidal current exits a strait, the flow decelerates as the cross-sectional area increases. If the deceleration is rapid enough for nonlinear dynamics to dominate, there will be a dynamic low pressure in the strait and high pressure outside the opening. In that case both the pressure gradient and bottom friction acts against the flow direction, and currents near the coast where friction is strongest might be brought to halt and even reverse, resulting in flow separation (Kundu et al., 2016; Signell and Geyer, 1991). Flow separation and corresponding flow asymmetry are typically present in straits that have strong tidal currents and abrupt openings. As also pointed out in the introduction, the generation of a tidal jet on outflow through an abrupt strait opening is intimately tied to the presence of a self-propagating dipole.

Before making quantitative estimates we take a look at the flow field in two of the straits. Figure 7 shows the flow and tracer field in Nappstraumen (4) through one tidal cycle. The various panels give time slices at 3 and 4.5 hours into the flood after slack tide and 3 and 4.5 hours into the ebb after the next slack tide (which corresponds to 9 and 10.5 hours after the first slack tide). At 3 hours we see that the northward-flowing tidal current has separated from the coast near the abrupt opening in the north. The separation has created two oppositely-signed vortices that are trailed by a jet, in line with previous studies (Afanasyev, 2006; Nøst and Børve, 2021). The vortices form a self-propagating dipole pair and grow in time, as can be seen at

https://doi.org/10.5194/os-2021-41
Preprint. Discussion started: 26 May 2021

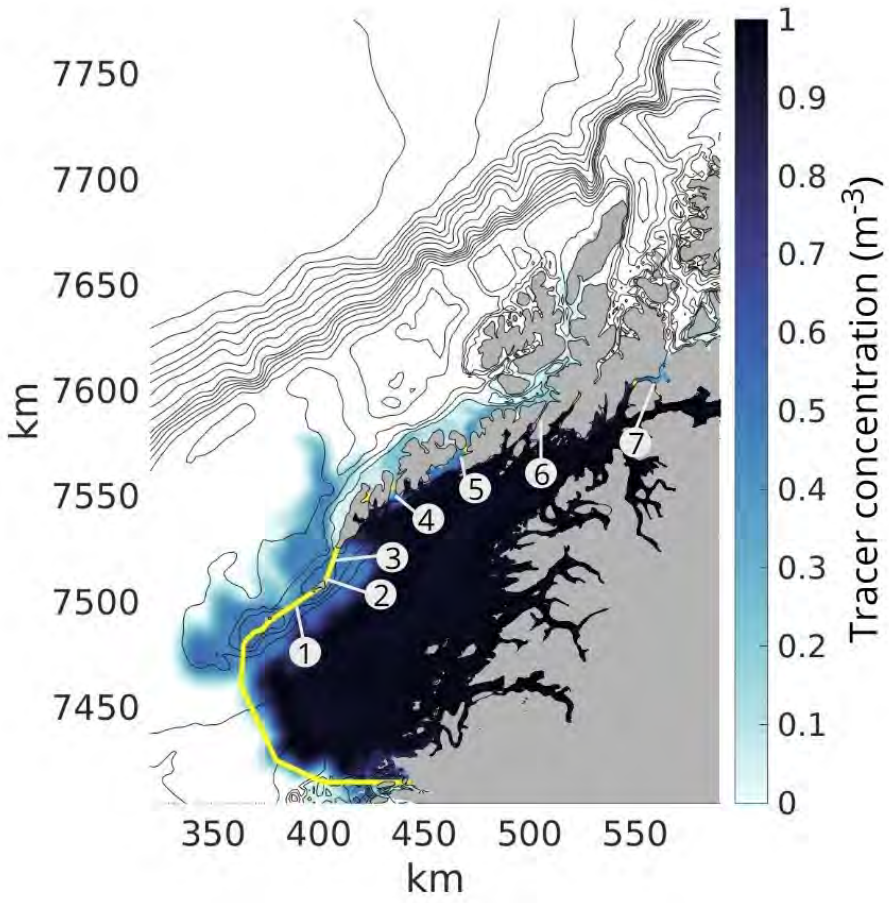

Figure 6. 72-hour average tracer concentration, two months after initial tracer release. The yellow line shows the boundary of the initial tracer release area. Inside the yellow boundary the initial tracer concentration was one, while everywhere else the tracer concentration was zero. The contours show the bottom topography.The main straits through the archipelago which will be investigated in this study are: (1) Røsthavet, (2) Nordlandsflaget, (3) Moskstraumen, (4) Nappstraumen, (5) Gimsøystraumen, (6) Raftsundet and (7) Tjeldsundet. Note that the numbering do not correspond to the numbering of the stations given in Figure 5.

https://doi.org/10.5194/os-2021-41
Preprint. Discussion started: 26 May 2021

Ocean Science
Discussions
Open Access
EGU

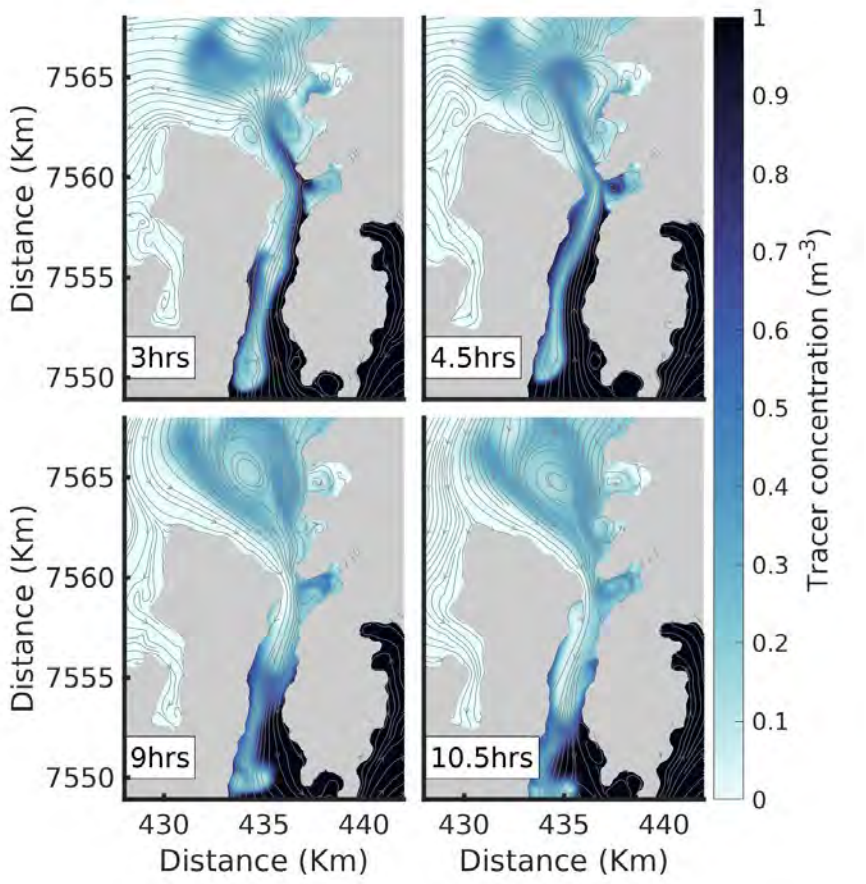

Figure 7. Tracer distribution in Nappstraumen (4) during the first full tidal cycle in the simulation. The time is given in hours after slack tide after ebb.

4.5 hours. The vortices clearly capture and transport waters with high tracer concentration northward as they propagate away from the strait during flood tide, as expected from theory.

The ebb tide (9 and 10.5 hours in the figure) returns water to the northern opening as potential flow, following the shape of the coastline. The flow paths are thus distinctly different compared to those during flood tide, and waters with low tracer concentration are drawn back in, particularly along the western flanks of the strait. In this particular strait the self-propagating dipole, formed during flood, is strong enough to escape the return flow. The bulk of the tracer captured by the two vortices therefore remains at the northern side, contributing significantly to the net tracer transport through Nappstraumen over the course of the full tidal cycle. At the more gradual southern opening of the strait, there is much less indication of flow separation. There is suggestion of a small and weak vortex pair forming along the south-western flank, but the net tracer transport appears to be limited.

https://doi.org/10.5194/os-2021-41
Preprint. Discussion started: 26 May 2021

Ocean Science
Discussions
Open Access
EGU

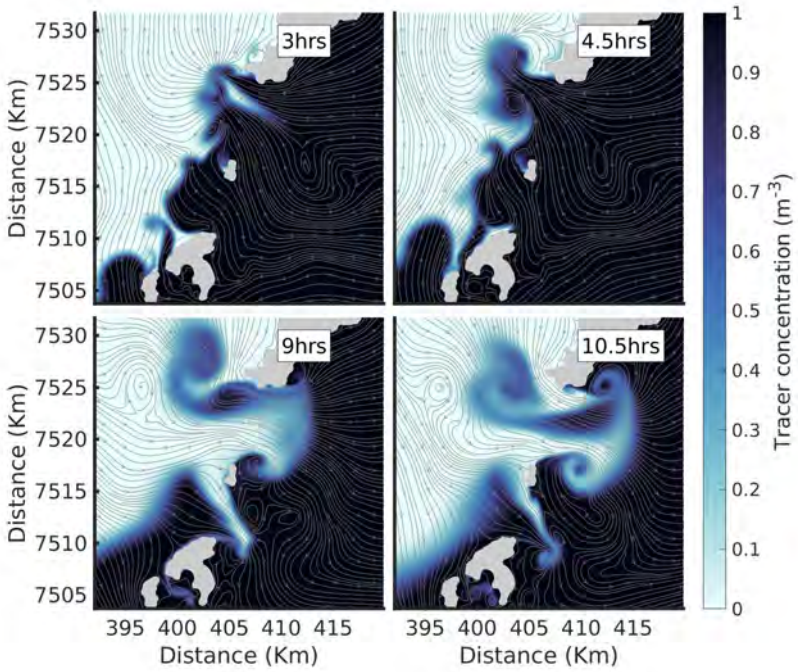

Figure 8. Same as Figure 7, but for Moskstraumen (3) and Nordlandsflaget (2).

The situation is somewhat different in Moskstraumen (3) between Lofotodden and the island of Mosken, as show in Figure 8. Here there is flow separation, dipole and jet formation at both exits during flood and ebb tide, respectively. A closer inspection shows that the dipoles form later in the tidal cycle compared to the generation at the northern exit in Nappstraumen, and their propagation distance is somewhat shorter when the flow reverses. Even so, their propagation speed is strong enough that the bulk of the dipoles avoid being transported back into the strait by the return flow. The inflow to Moskstraumen, in contrast, also primarily takes the form of potential flow, drawing fluid into the strait from all directions. The result is a large net tracer transport which is clearly seen in Figure 6. A dipole with a trailing jet is also observed to form during ebb tide (10.5 hours) in Nordlandsflaget (2) a few kilometers to the south-west between the islands of Mosken and Værøy. This flow feature brings low-concentration waters into Vestfjorden, but the net effect appears to be somewhat dwarfed by the pumping that takes place in Moskstraumen.

3.1.1 Parameters controlling tidal pumping

According to Nøst and Børve (2021), the net transport of a tracer through a tidal strait depends primarily on two non-dimensional length scales. The first parameter is a purely kinematic one, namely the ratio of the tidal excursion L_t (the expected travel distance of a particle transported by the tidal current) and the length L_{xs} of the strait:

$$L^* = \frac{L_t}{L_{xs}}. \tag{1}$$

https://doi.org/10.5194/os-2021-41
Preprint. Discussion started: 26 May 2021

If the tidal excursion is shorter than the strait ($L^* < 1$), a net transport of properties is not possible. The second non-dimensional length scale reflects the dynamics at play, namely the travel distance of the self-propagating dipole relative to the extent of the sink region:

$$L_s = \frac{L_d}{R_s}, \tag{2}$$

where L_d is the dipole travel distance during one half tidal period and R_s is the sink radius (a measure of the region covered by potential flow on inflow to the strait). L_s corresponds roughly to the nondimensional Strouhal number used by Kashiwai (1984) and Wells and van Heijst (2003). If $L_s < 1$, the dipole is inside the sink region and will be affected by the potential flow back into the strait. Depending on the self-propagation velocity of the dipole relative to the sink velocity at its positions, a smaller or larger fraction of the dipole will be pulled back into the strait.

While the first non-dimensional parameter, L^*, is relatively easy to estimate in our study, the second parameter, L_s, is more complicated to work with in a realistic setting. L_s depends on the dipole properties and the shape of the sink regions, both of which are affected non-trivially by the kind of complex bathymetry and coastlines present in Lofoten. Therefore, instead of tracking dipole travel distances and estimating sink radii, we here chose to assess the flow asymmetry at the strait openings. In other words, we set out to investigate the extent to which the inflow through a strait opening behaves as potential flow whereas the outflow takes the form of a jet. As such, this relationship is more in line with the original model of Stommel and Farmer (1952) and follows the procedure recommended by Signell and Butman (1992).

To reiterate, the formation of a tidal jet during outflow from a strait requires flow separation which is driven, in part, by the build-up of an adverse pressure gradient. The build-up of an adverse pressure gradient, in turn, requires nonlinear advection of momentum (Signell and Geyer, 1991). So it makes sense to investigate the relationship between non-linearity and flow asymmetry in the various straits in Lofoten. In a coordinate system where the x-axis points along the strait, a truncated form of the along-strait momentum equation is

$$\frac{\partial u}{\partial t} + u\frac{\partial u}{\partial x} = -g\frac{\partial \eta}{\partial x}, \tag{3}$$

where u is the along-strait velocity, η is the sea surface height and g is the gravitational acceleration. We have ignored cross-strait advection and friction for the arguments to follow (skin friction in our simulations is demonstrably small compared to the time acceleration at tidal frequencies) . An assessment of the importance of non-linearity in a strait opening can be done by comparing the advection term to the time rate of change of momentum. The advection term itself can be estimated from volume conservation as

$$u\frac{\partial u}{\partial x} \sim u_i \frac{u_i}{\Delta x}\left(\frac{A_i}{A_e} \breve{} 1\right), \tag{4}$$

where u_i is the velocity at the inner, narrow, part of the strait, and A_i and A_e are the cross-sectional areas covered by the current at the inner part of the strait and the strait exit, respectively. Finally, Δx measures the distance over which the change in cross-sectional area takes place. If the tidal current is large and the change in cross-sectional area is large and abrupt (meaning $A_e \gg A_i$ and Δx is small), then the nonlinear advection will be strong.

https://doi.org/10.5194/os-2021-41
Preprint. Discussion started: 26 May 2021

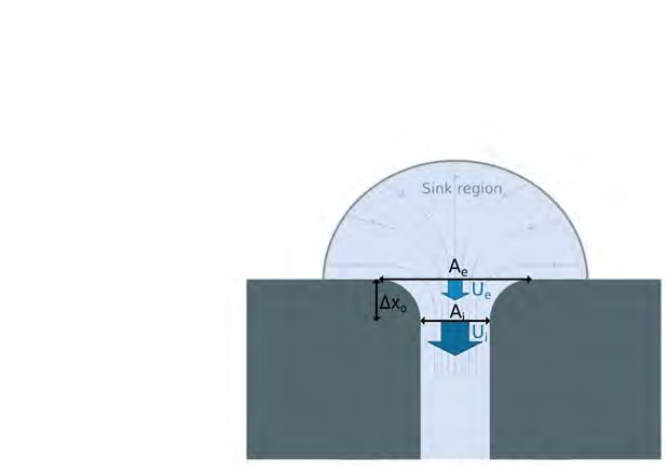

Ocean Science
Discussions
Open Access
EGU

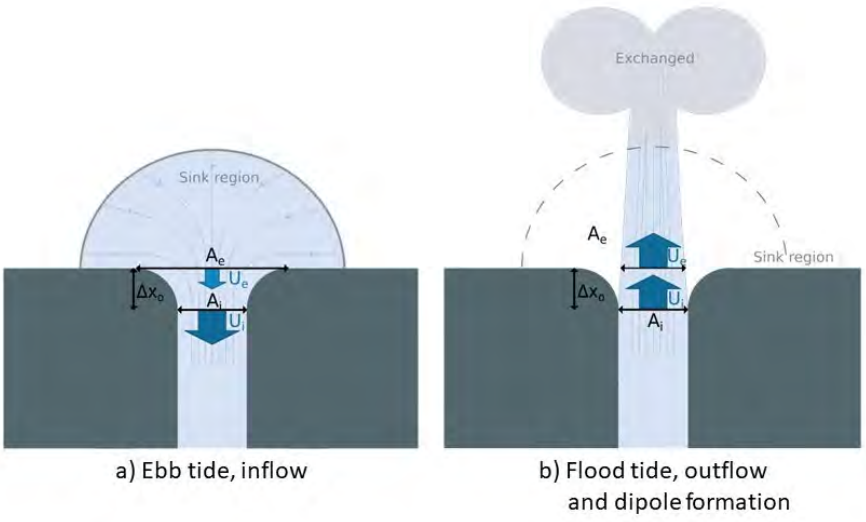

Figure 9. A sketch illustrating flow asymmetry. The left panel a) shows the tidal current entering the strait from all directions during ebb tide. The right panel b) show a tidal current exiting the same strait during flood tide. However, now the flow separates from the coastline and a dipole with a trailing jet has formed and propagated away from the strait. U is the tidal current speed and A is the cross-sectional area. The notations $_i$ and $_e$ corresponds to the inner and outer side of the strait opening, respectively. Δx is the length of the strait opening where we evaluate the flow asymmetry and the nonlinearity of the flow dynamics.

The non-linearity of the flow is then found by dividing (4) by u_i/T, where T is half a tidal period. So we get the non-linearity parameter

$$S_{nl} = \frac{u_i T}{\Delta x}\left(\frac{A_i}{A_e} - 1\right). \tag{5}$$

As shown by the sketch in Figure 9, the area covered by the jet at the strait exit, A_e, can be quite different between inflow and outflow. On inflow the appropriate scale for A_e is the actual width of the strait exit, while on outflow the scale may be that of the jet—if a jet forms. So the *maximum* strength of non-linearity is best measured on inflow, i.e. using values of A_i and A_e gathered from the strait geometry.

To assess flow asymmetry, we will use the model's pressure or sea surface height field. To understand how flow asymmetry will manifest itself in the pressure field, we again return to the sketch in Figure 9. If the inflow takes the form of potential flow while the outflow is in the form of a jet (as indicated in the figure), the non-linear pressure gradient across the strait opening (i.e. over distance Δx) will be larger during inflow than during outflow. This observation suggests that the magnitude of the difference in pressure gradient between inflow and outflow will be a measure of the asymmetry.

We start by forming normalized pressure gradients across each strait openings:

$$\widetilde{\Delta\eta} = \frac{\Delta\,\eta_o/\Delta x_o}{\Delta\eta_s/\Delta x_s}, \tag{6}$$

https://doi.org/10.5194/os-2021-41
Preprint. Discussion started: 26 May 2021

where $\Delta\eta_o/\Delta x_o$ is the pressure gradient across the opening and $\Delta\eta_s/\Delta x_s$ is the corresponding gradient across the entire strait. The latter should primarily reflect the large-scale pressure gradient, so normalizing by this will help isolate the nonlinear contribution to the pressure gradients around the strait exits. The flow asymmetry around a given strait exit is then measured by the magnitude of the difference between $\widetilde{\Delta\eta}$ at flood and ebb tide:

$$A_{xo} = |\widetilde{\Delta\eta}_{flood} - \widetilde{\Delta\eta}_{ebb}| \tag{7}$$

A small value of A_{xo} should indicate negligible flow asymmetry while a large value should indicate large flow asymmetry and thereby the potential for prominent tidal pumping.

We calculated $\widetilde{\Delta\eta}$ at ebb and flood tide for each M2-tidal cycle at both openings of all the straits shown in Figure 6. Individual estimates for each strait opening and each phase of the tides were then averaged over the whole simulation period. Finally, a mean asymmetry parameter A_{xo} was calculated for each opening. Since we deal with realistic geometries, the definition of the openings is somewhat subjective. But we tried to apply similar criteria to all strait openings, choosing the most obvious outer strait entrance/exit and the corresponding closest narrow cross section inside. The outer opening would typically be where flow separation and dipole formation could potentially occur and contribute to tidal pumping. An example is the northern exit of Nappstraumen, which is defined to start at the narrow cross-section where the flow separates and dipole forms (see Figure 7). Corresponding nonlinearity parameters S_{nl} were also estimated over the same openings for each M2 tidal cycle and averaged over these.

The estimates of A_{xo} and S_{nl} for the seven straits are shown in Figure 10. The calculation reveals considerable scatter but indicates a near-linear relation between the two parameters. This suggests that most straits that have nonlinear flow dynamics also have a flow asymmetry that may be linked to formation of tidal jets. We made estimates for both openings of each strait since the geometries on the two sides may be widely different. Nappstraumen (4) is the most notable example. At its northern opening, the flood exit, abrupt changes in the coastal geometry causes the flow dynamics to be highly nonlinear and asymmetric between flood and ebb. And we saw from Figure 7 that the asymmetry here is closely tied to prominent dipole formation during flood tide. In contrast, at the more gradual opening in the south, non-linearity, dipole formation and asymmetry are much weaker.

The largest nonlinearities and asymmetries are found in the northern opening of Nappstraumen (4), in both openings of Moskstraumen (3) and in the southern (ebb) opening of Nordlandsflaget (2). It is interesting to note that the non-linearity in Røsthavet (1) is comparable to that in the northern (flood) opening of Nordlandsflaget, but that the asymmetry is lower. As it turns out, Røsthavet is the widest strait in the whole region. So although tidal currents are just as large as in Nordlandsflaget and there is actually flow separation here during both phases of the tide (not shown), the vortices formed are too far apart to form a self-propagating dipole and a trailing tidal jet. The longer straits in the north (5–7) all have moderate to low nonlinearities and asymmetries. The reason for this is probably that the overall flow dynamics becomes more linear as the strait length increases (Nøst and Børve, 2021). This brings down the current speeds, and hence the nonlinearity, in these long straits.

https://doi.org/10.5194/os-2021-41
Preprint. Discussion started: 26 May 2021

Ocean Science
Discussions
Open Access
EGU

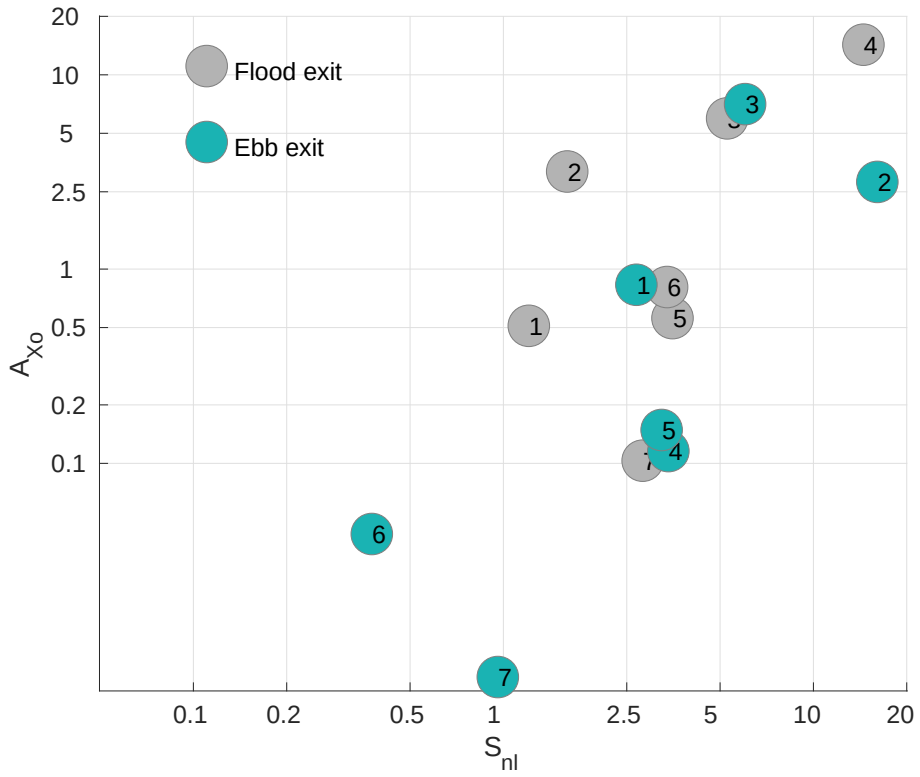

Figure 10. Estimates of the flow asymmetry A_{xo} at the openings of each strait plotted against the non-linearity parameter S_{nl}. Green dots are values at the flood exit (directed out of Vestfjorden) while light gray dots are values at the ebb exits (directed into Vestfjorden). Both parameters are plotted on log scales.

Measuring tidal pumping strength

To finally evaluate the strength of the tidal pumping, we calculate a tracer transport efficiency for each strait. The transport efficiency T_p^* is defined as the actual tracer transport through the strait divided by a 'transport potential' made up of the time-averaged magnitude of the along-strait velocity $|u|$, the time-averaged mean tracer concentration difference between the two strait openings Δc and the strait cross-sectional area A. So

$$T_p^* = \frac{\iint \overline{u'c'}\, dA}{\overline{\Delta c}\,\overline{|u|}\, A}. \tag{8}$$

where overbars indicate the time mean and primes indicate perturbations from that mean, so that $\overline{u'c'}$ is the Reynolds flux of c. The transport efficiency for a given strait is estimated in the same manner as the non-linearity and flow asymmetry, i.e. by calculating a value for each M2 tidal cycle and then averaging over the whole simulation period.

Figure 11 shows T_p^* for all straits plotted against asymmetry parameter A_{xo} and the nondimensional tidal excursion L^*. The asymmetry parameter for a given strait is the average from the two strait openings. As already discussed, and as seen in panel

https://doi.org/10.5194/os-2021-41
Preprint. Discussion started: 26 May 2021

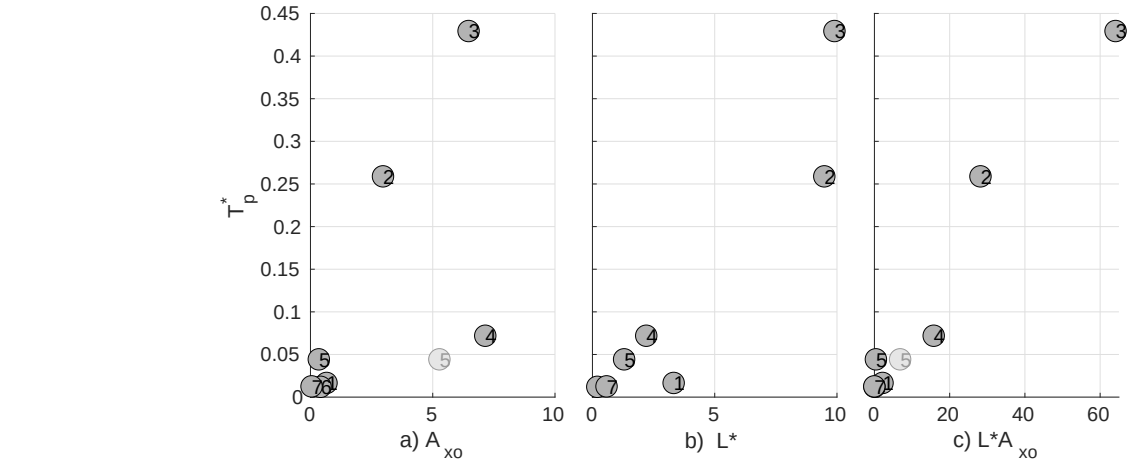

Figure 11. The tracer transport efficiency T_p^* plotted against non-dimensional parameters A_{xo} (a), L^* (b) and $A_{xo}L^*$ (c). Two estimates of A_{xo} are shown for Gimsøystraumen (5).

(a), three straits stand out in terms of flow asymmetry: Nordlandsflaget (2), Moskstraumen (3) and Nappstraumen (4) (where the high value comes from the northern opening). We now see that these are also the three straits with the highest transport efficiency. But even though Nappstraumen has the largest flow asymmetry of all straits, the transport efficiency is notably lower than in Nordlandsflaget and Moskstraumen. The likely reason is tied to the fact that Nappstraumen is a relatively long strait, as can be seen in panel (b). The tidal excursion in Nappstraumen (4) is only twice the strait length, while the excursion in Nordlandsflaget (2) and Moskstraumen (3) is almost ten times longer than the strait length. Hence, just by considering the strait length, we expect the net effect of flow asymmetries in Moskstraumen and Nordlandsflaget to be larger than in Nappstraumen. Røsthavet (1) is also a short strait, where the tidal excursion is much larger than the strait length. However, in this strait the flow asymmetry is weak and we thus expect little tidal pumping. We have at present no underlying theory for tidal pumping efficiency as a function of both A_{xo} and L^*. But since the transport efficiency must depend on both flow asymmetry *and* short strait length compared to the tidal excursion, we plot T_p^* against the product of the two parameters in panel (c). The scatter is now reduced and the data from the various straits roughly follow a linear relationship.

In forming the various estimates above some subjective decisions will impact the results. In particular, the exact value of the asymmetry parameter A_{xo} depends on the location chosen for the inner and outer opening of a strait (to calculate a pressure drop). Complex strait geometries typically make clear-cut choices difficult. Gimsøystraumen (5) is the strait which has the most complex geometry, having two regions where the strait widens in the north (not shown). In Figure 11 we have therefore shown two estimates of A_{xo} for this strait, based on pressure differences taken across these two distinct northern openings. The exercises suggest that A_{xo} for this strait ranges from 0.8 to 5.5, where the latter value begins to approach the asymmetry of Nappstraumen. We take the span of values in Gimsøystraumen as an upper bound for the general uncertainty in A_{xo}. Raftsundet also has a complex opening in the north, however, the length of this strait is the main limiting factor for net transports by tidal pumping, and the result will not change notably due to the nonlinearity parameter. The uncertainty for the other straits, with

https://doi.org/10.5194/os-2021-41
Preprint. Discussion started: 26 May 2021

simpler geometries, is lower. Given this level of uncertainty, we therefore take the above calculations as clear indication that the transport efficiency through the various straits in Lofoten-Vesterålen are closely linked to the level of flow asymmetry caused by flow separation, dipole and jet formation, and to the length of the straits relative to the tidal excursion.

3.2 Rectified tidal currents

The second nonlinear process to be assessed is the rectification of oscillating tidal currents around the islands off the southern tip of Lofoten. Residual tidal currents encircling banks and islands have been observed in various places around the world, like the Norfolk islands and Georges bank (Huthnance, 1973; Loder, 1980). The key process, as outlined in the introduction, appears to be net vorticity fluxes generated by vortex stretching and squeezing by oscillating tidal flow over sloping bottom topography—in the presence of some irreversibility, like bottom friction.

In Lofoten, the distortion of the northward-propagating tidal waves produces particularly strong tidal currents across the shallow ridge south of Lofotodden (Figure 4). Tidal rectification around the islands located here, Mosken, Værøy and Røst, seems likely. And indeed, a zoom in on on this region in Figure 12 reveals time-mean anticyclonic (clockwise) circulation cells around the islands. There are two distinct circulation cells, one around Røst and another around Værøy-Mosken. The circulation cells reach speeds of about 0.2–0.25 m/s, which is similar in magnitude to observed background currents in the region (Mork, 1981). In Moskstraumen, the model's mean current speeds exceed 0.5 m/s, but the strongest flow here is associated with a rectified anticyclone on the inside of that strait—an anticyclone we will return to later. Figure 12 also shows the time-mean tracer field, revealing that the circulation cells advect low-concentration waters into Vestfjorden northeast of the island groups and high-concentration waters out of the fjord on the southwest sides. Much of the net tracer transport is clearly associated with the tidal pumping mechanism investigated above, but transport of tracer out of Vestfjorden south of Røst is clearly mainly tied to the anticyclonic flow around this island.

3.2.1 Vorticity flux and residual currents

Before doing a quantitative analysis of these currents, we will review some of the relevant theory. One useful starting point (following e.g. Zimmerman, 1978, 1981) is the vorticity balance derived from the shallow-water equations:

$$\frac{\partial \xi}{\partial t} + \nabla \cdot \boldsymbol{u}(f+\xi) = -\nabla \times \left(\frac{\boldsymbol{\tau}_b}{H}\right), \tag{9}$$

where $\xi = \nabla \times \boldsymbol{u}$ is relative vorticity, f is the Coriolis parameter, $\boldsymbol{\tau}_b$ is a bottom stress and H is the water depth. We have neglected forcing by a surface wind stress and also, for simplicity, lateral viscosity. In the simplified treatment below we will also only consider linear bottom friction, so that $\boldsymbol{\tau}_b = R\boldsymbol{u}$. Finally, we will ignore the sea surface height contribution to the water column thickness, i.e. apply the rigid lid approximation. Integration of (9) over the area bounded by a closed depth contour s, followed by the use of Stokes' theorem, gives

$$\frac{d}{dt}\oint \boldsymbol{u}\cdot\hat{\boldsymbol{t}}\,ds + \oint \boldsymbol{u}(f+\xi)\cdot\hat{\boldsymbol{n}}\,ds = -\frac{1}{H}\oint R\boldsymbol{u}\cdot\hat{\boldsymbol{t}}\,ds, \tag{10}$$

https://doi.org/10.5194/os-2021-41
Preprint. Discussion started: 26 May 2021

Ocean Science
Discussions
Open Access
EGU

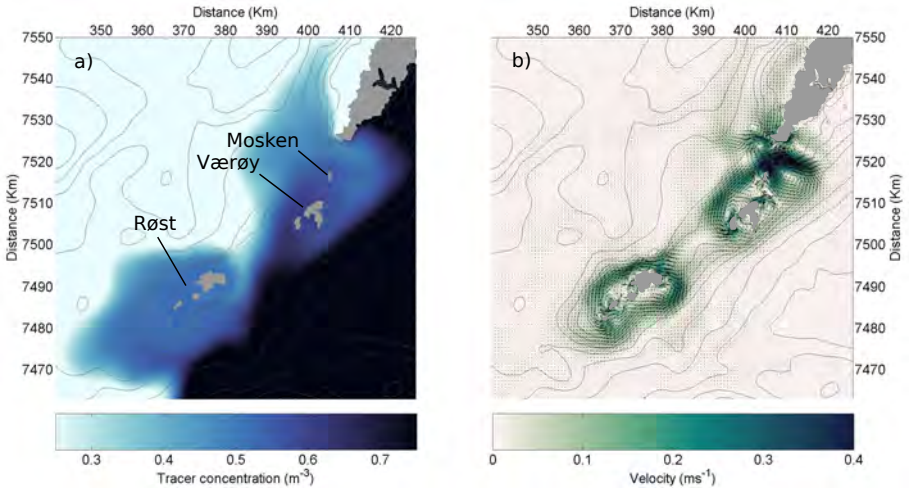

Figure 12. Time-mean tracer concentration (a) and time-mean currents (b) around the southern tip of Lofoten near the end of the simulation. Thin contours show the bottom topography.

where $\hat{\boldsymbol{t}}$ and $\hat{\boldsymbol{n}}$ are unit vectors tangential (positive clockwise) and normal (positive outwards) to the contour. We now apply the Reynolds decomposition to velocity and vorticity, splitting into means over a tidal cycle and perturbations from such means. If considering the Coriolis parameter to be constant (a very good assumption for the scales considered here), then a time average over a tidal cycle gives the approximate balance

$$\frac{d}{dt}\oint \bar{\boldsymbol{u}}\cdot\hat{\boldsymbol{t}}\,ds+\oint \overline{\boldsymbol{u}'\xi'}\cdot\hat{\boldsymbol{n}}\,ds=-\frac{1}{H}\oint R\bar{\boldsymbol{u}}\cdot\hat{t}\,ds, \tag{11}$$

where, as before, overbars indicate the time mean and primes perturbations from that mean. We have ignored a term involving transport of mean vorticity by mean currents since this can be assumed to be small for oscillatory tidal forcing. Note that after the time averaging, the time evolution left in (11) is over scales longer than the fast tidal oscillations. So the expression states that a net Reynolds flux of vorticity out of a closed depth contour will cause an acceleration of anticyclonic flow around the contour (at time scales shorter than $T\sim H/R$) and, eventually, a time-mean anticyclonic flow which balances the vorticity flux with bottom friction.

The total response to arbitrary forcing can be found by Fourier-transforming the above integral equation in time. The expression for each individual Fourier-component becomes

$$\oint i\omega\bar{\boldsymbol{u}}\cdot\hat{\boldsymbol{t}}\,ds+\oint \overline{\boldsymbol{u}'\xi'}\cdot\hat{\boldsymbol{n}}\,ds=-\oint\frac{R\boldsymbol{u}}{H}\cdot\hat{\boldsymbol{t}}\,ds, \tag{12}$$

where, now, velocity and vorticity are functions of frequency rather than time. Depth H is constant along a closed s contour, and if we assume that R is constant as well we get an expression for dynamic response of the mean circulation around the contour:

$$\oint \bar{\boldsymbol{u}}\cdot\hat{\boldsymbol{t}}\,ds=-\frac{\oint \overline{\boldsymbol{u}'\xi'}\cdot\hat{\boldsymbol{n}}\,ds}{R/H+i\omega}. \tag{13}$$

https://doi.org/10.5194/os-2021-41
Preprint. Discussion started: 26 May 2021

Ocean Science
Discussions
Open Access
EGU

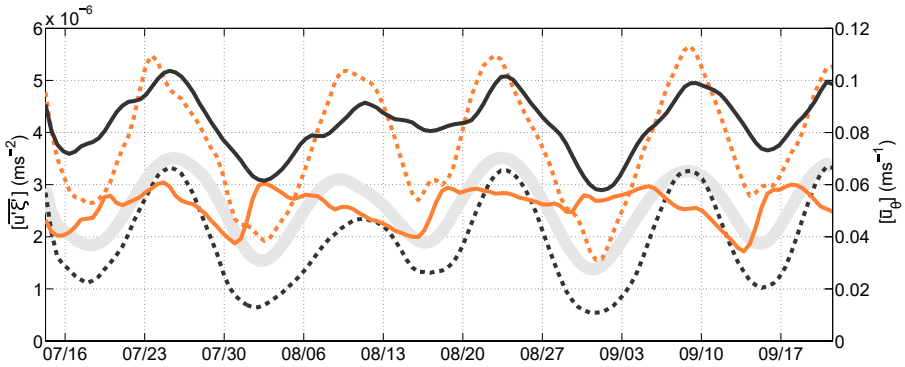

Figure 13. Reynolds vorticity flux ($\overline{u'\xi'}$, dashed lines) out of closed depth contours that wrap around Mosken-Værøy (orange) and around Røst (black), and azimuthal velocity ($\bar{u}_\theta = \bar{\boldsymbol{u}} \cdot \hat{\boldsymbol{t}}$, solid lines), both averaged around the same closed contours. All quantities have been smoothed over four M2 cycles and also averaged over a set of closed contours between 30 and 70 meters. Sea surface height fluctuations (gray thick line) over southern Lofoten are also shown.

So the prediction is a circulation whose magnitude is equal to the integrated vorticity flux scaled by $|R/H + i\omega|$ and whose phase lag is $\phi = \tan^{-1}(\omega H/R)$. The full response to forcing over a range of frequencies can then be found by solving (13) for each frequency, followed by an inverse Fourier transform. The time-dependent problem is essentially an f-plane equivalent to that of wind-driven closed-f/H variability studied by Isachsen et al. (2003), but with wind stress forcing replaced by lateral vorticity fluxes.

The primary slow time scale variation in forcing for our problem is the spring-neap cycle. So $\omega_{sn} = 2\pi/14.75\,\mathrm{rad\,days}^{-1}$. Using a typical value for bottom friction, $R = 10^{-3}\,\mathrm{m\,s}^{-1}$, and a depth $H = 50\,\mathrm{m}$, we expect a spin-up time of approximately 14 hours which corresponds to a phase lag ϕ of about 0.24 radians or 14 degrees. We now test these predictions on the time-mean flow cells observed around the islands near the tip of Lofoten. Figure 13 shows the Reynolds vorticity flux out of closed depth contours that wrap around Mosken–Værøy and around Røst. For each contour, a contour-averaged Reynolds flux has been calculated for each sequential M2 tidal cycle. The resulting time series has then been low-pass filtered using a Hanning filter of width equal to four M2 cycles. Finally, for each island group (Mosken–Værøy and Røst) an average has been made over several such closed contours. The calculation clearly reveals a positive vorticity flux out of the contours (towards greater depths) at all times, and this flux is roughly in phase with the spring-neap variations in sea surface height over the region (also shown). Finally, the figure shows the low-passed azimuthal velocity (tangent to a contour) averaged around the same sets of contours. The circulation is anticyclonic and thereby in agreement with the sign of the vorticity flux.

However, the figure also reveals that the two circulation cells respond differently to the spring-neap cycle. The cell around Røst is nearly in phase with the Reynolds flux forcing, with a phase delay of only about half a day—close to the theoretical prediction. But the flow variability around Mosken-Værøy is more erratic and, on average, lagging the forcing by 9-10 days. The amplitude of the spring-neap flow variations around Mosken-Værøy is also smaller than that around Røst even though the amplitude of the Reynolds flux forcing is larger. Taken together, these results indicate that the theory works well at describing

https://doi.org/10.5194/os-2021-41
Preprint. Discussion started: 26 May 2021

the slowly-evolving anticyclonic circulation around Røst but that additional dynamics must be considered to understand the cell around Mosken-Værøy. We will return to this issue below but will first examine the underlying process that sets up the vorticity flux through these closed depth contours.

3.2.2 The source of the vorticity flux

The direction of the vorticity flux may be understood by following a water column that moves periodically up and down a topographic slope, driven by a large-scale tidal potential (Zimmerman, 1978, 1981). Substituting the shallow-water continuity equation into (9) gives

$$\frac{D(f+\xi)}{Dt} = \left(\frac{f+\xi}{H}\right)\frac{DH}{Dt} - \nabla\times\left(\frac{R\boldsymbol{u}}{H}\right), \tag{14}$$

where $D/Dt = \partial/\partial t + \boldsymbol{u}\cdot\nabla$ is the total (Lagrangian) time rate of change experienced by the moving water column. Applying the rigid-lid and f-plane approximations, assuming $\boldsymbol{\tau}_b = R\boldsymbol{u}$ and splitting up the friction term, gives

$$\frac{D\xi}{Dt} = \left(\frac{f+\xi}{H}\right)\boldsymbol{u}\cdot\nabla H + \frac{R}{H^2}\boldsymbol{u}\times\nabla H - \frac{R}{H}\xi, \tag{15}$$

from which we can see that relative vorticity of the column has two source terms and one sink term. The first term on the RHS is vorticity production due to stretching or squeezing of the water column by flow over uneven bottom topography. If $f+\xi>0$ motion towards deeper (shallower) water induces positive (negative) relative vorticity perturbations. The second term is production of vorticity due to flow along a sloping bottom and often referred to as a bottom friction torque. The last term on the RHS is a loss of vorticity to bottom friction.

If we assume $|\xi| \lesssim f$ (see e.g. Table 1 of Zimmerman, 1978), then the sizes of the two production terms are

$$\begin{aligned}\frac{(f+\xi)}{H}\boldsymbol{u}\cdot\nabla H &\sim \frac{fUh'}{DL},\\ \frac{R}{H^2}\boldsymbol{u}\times\nabla H &\sim \frac{RUh'}{D^2L},\end{aligned}$$

where U is tidal current amplitude, D is mean water depth and h' and L are the height and length scales of the topographic feature. Comparing the magnitude of the two terms, using typical values for Mosken/Værøy and Røst ($D\sim 50\,\mathrm{m}$, $R\sim 10^{-3}\,\mathrm{m\,s^{-1}}$ and $f\sim 10^{-4}\,\mathrm{s^{-1}}$), gives $fD/R\sim 5$. This suggests that vorticity production by flow up and down topography is quite a bit larger than production by bottom friction torque. If $|\xi|>f$ the production term by squeezing and stretching of the water column becomes increasingly larger compared to production of bottom friction torque for the same depth. For simplicity we will therefore neglect the latter term in the following, leaving the approximate expression

$$\frac{D\xi}{Dt} = \left(\frac{\xi+f}{H}\right)\boldsymbol{u}\cdot\nabla H - \frac{R}{H}\xi \tag{16}$$

$$= \left(\frac{\xi+f}{H}\right)\frac{DH}{Dt} - \frac{R}{H}\xi, \tag{17}$$

or, cast in terms of potential vorticity (PV),

$$\frac{D}{Dt}\left(\frac{f+\xi}{H}\right) = -\frac{R}{H}\xi. \tag{18}$$

https://doi.org/10.5194/os-2021-41
Preprint. Discussion started: 26 May 2021

In the absence of bottom friction, PV is conserved, and the relative vorticity of a water column will only be a function of depth (on the f-plane). So as the water column oscillates up and down a sloping bottom, it will gain just as much negative (anticyclonic) vorticity on its way up the slope as it gains positive (cyclonic) vorticity on its way down the slope. The net vorticity transport by the column across a given depth contour will therefore be zero. Crucially, friction changes this since the column will then lose some negative vorticity over shallow waters and lose some positive vorticity over deep waters. Thus, on passing any given depth contour the column will carry an excess of positive vorticity on its way towards deep waters and an excess of negative vorticity on its way towards shallow water. The end result is a transport of positive vorticity towards deep waters. A simple sketch of the rectification process is shown in Figure 14 and a simplified mathematical model is offered in the Appendix.

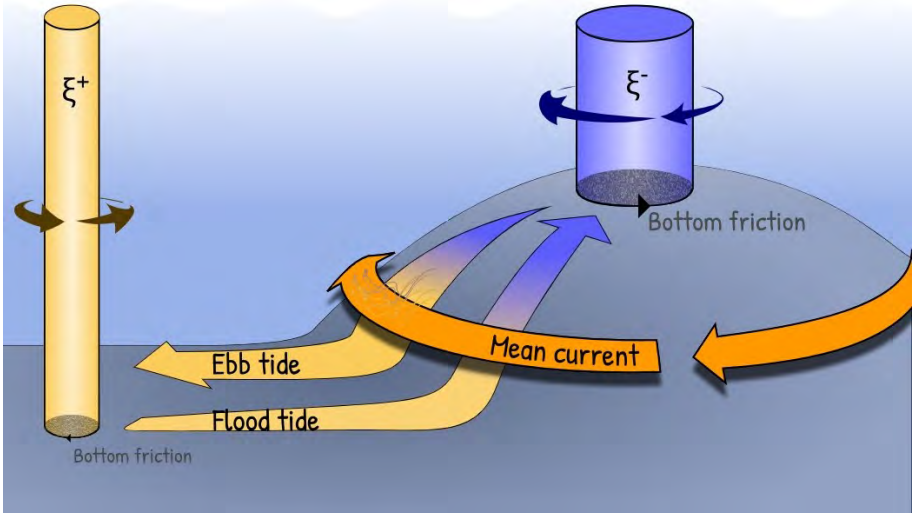

Figure 14. A sketch of mean-flow generation around a bank from oscillating flow across the bank topography. A water column oscillates up and down topography, attaining negative vorticity on its way up the slope and positive vorticity on its way down due to vortex squeezing and stretching, respectively. Bottom friction removes some negative vorticity from the column over shallow regions and some positive vorticity over deep regions. A sustained oscillation, by a large-scale tidal potential, will hence be associated with a positive vorticity flux from shallow to deep regions. The vorticity flux from many such columns is balanced by a mean anti-cyclonic circulation around the bank.

The net effect after integrating over the movement of many such water columns is a positive relative vorticity flux towards deep regions. Hence, (11) predicts anticyclonic currents around a bank or island, and this is indeed what we observe in Figures 12 and 13. It is worth noting that the vorticity flux is down the large-scale background PV gradient $q_s = f/H$. So when we ignore Reynolds transport of layer thickness (in line with the rigid lid approximation), the process is qualitatively consistent with the idea of potential enstrophy dissipation via a down-gradient PV flux (Bretherton and Haidvogel, 1976; Ou, 1999).

The magnitude of the rectified current depends on the steepness of the topographic slope and the strength of the cross-slope tidal oscillations (Zimmerman, 1978; Loder, 1980; Wright and Loder, 1985). From the scaling argument above we found that the main driver of rectification is the generation of relative vorticity by advecting water columns up and down the bottom

https://doi.org/10.5194/os-2021-41
Preprint. Discussion started: 26 May 2021

topography. Thus, by identifying the regions of max potential for generation of relative vorticity by cross-slope tidal currents, we can identify the areas where tidal rectification is to be expected. To look at this we ignore the effect of bottom friction, leaving

$$\frac{D\xi}{Dt} = \frac{f+\xi}{H}\frac{DH}{Dt}. \tag{19}$$

Hence, the relative vorticity change ξ' experienced by a water column forced across variable topography scales as

$$\xi' = \frac{f+\xi_0}{H_0}h', \tag{20}$$

where ξ_0 and H_0 are initial vorticity and depth, respectively, and h' is the topographic variation. If we assume a constant bottom slope α, then $h' = \alpha L$ where L is the lateral excursion of the water column. A topographic length scale can then be defined as that which gives a depth excursion equal to the initial depth, or $H_0 = \alpha L_B$. By (20), such an excursion would produce the maximum relative vorticity deviation and hence the maximum potential for rectified currents. The *actual* lateral excursion experienced by parcels is given by the tidal excursion $L_T = \int \boldsymbol{u}\cdot\hat{\boldsymbol{n}}\,dt$ where, again, $\hat{\boldsymbol{n}}$ points down the topographic gradient and where the integral is taken over half a tidal cycle. Thus, $h' = \alpha L_T$. If $L_T \ll L_B$ then vorticity chances will be small since the full potential for stretching/compression is not utilized. And if $L_T \gg L_B$ then the net vorticity changes integrated over half a tidal cycle will likely also be small due to sign reversals as the column is advected up and down topographic 'bumps'. Intuitively then, and as verified numerically by Zimmerman (1978), one expects that the largest potential for the generation of rectified currents where $L_T \sim L_B$ (see also Loder, 1980; Polton, 2015).

The ratio between time-mean L_T and L_B off the tip of Lofoten is shown in Figure 15. The topographic scale L_B has been calculated from bathymetric data and the tidal excursion L_T has been estimated using the mean M2 tidal current amplitudes across topography. The figure also shows the time-mean flow, and there is clear indication that the rectified currents around Mosken-Værøy and around Røst are most pronounced where $L_B/L_T \gtrsim 1$. We take this as supportive evidence that the rectified currents around these islands are driven by oscillating flows over topography subject to weak bottom friction. Figure 16 shows the strength of the rectified currents around the above-studied closed H-contours as a function of L_T/L_B, where L_T is now allowed to vary as a function of time (i.e. with the spring-neap cycle). Around Røst residual currents attain a maximum for $L_T/L_B \sim 1.75$, with declining strengths for both smaller and larger values of the ratio. This is in agreement with theory. In contrast, the plot does not show any optimal value of L_T/L_B for the flow around Mosken-Værøy. The residual current strength here instead decreases monotonically with larger values of the ratio. As we will see next, the reason for the anomalous behavior around these islands turns out to be finite-amplitude non-linear effects.

3.2.3 Non-linear dynamics around Mosken-Værøy

The sign of the residual currents around Mosken-Værøy is in agreement with the sign of the Reynolds vorticity flux across the closed depth contours there. But, as seen above, the time variability does not correlate trivially with the spring-neap variations in the vorticity flux. So additional dynamically processes must be at play here and, as indicated by Figure 12, a semi-persistent anticyclone southeast of Moskstraumen is likely the culprit. During each ebb tide, when the flow entering Vestfjorden through

https://doi.org/10.5194/os-2021-41
Preprint. Discussion started: 26 May 2021

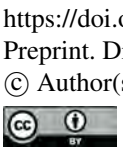

Ocean Science
Discussions
Open Access
EGU

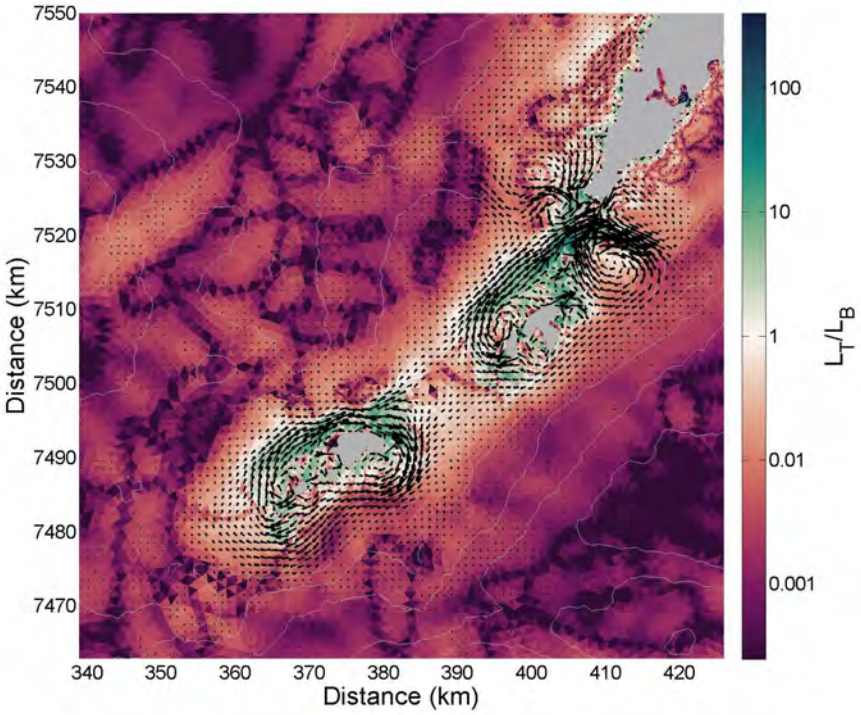

Figure 15. The ratio L_T/L_B around southern Lofoten. Arrows show the time-mean rectified flow while black contours show bottom topography.

Moskstraumen separates from the coastline, a dipole is formed, as seen in Figure 8. After flow reversal, the cyclonic half of the dipole is typically drawn back into Moskstraumen whereas the anti-cyclonic vortex remains on the southeastern side of the strait. The position of the anticyclone varies somewhat over time, but it is consistently strengthened by new vortex formation during each ebb phase.

Figure 17 shows streamlines of the time-mean flow in the vicinity of Mosken-Værøy. The streamlines that wrap around these two islands generally follow depth contours. But the anticyclone east of Mosken is strong enough to break topographic steering in the northeast. Streamlines that encircle the island group detach from topography just north of Mosken to wrap around the anticyclone. The closed depth contours around Mosken-Værøy thus pass through the southwest flank of the anticyclone, so that currents from the vortex are here in the opposite direction compared to the rectified currents along the rest of the contours.

In essence, the strong anticyclone has deformed the geostrophic contours guiding the time-mean flow, and the integral analysis of (13) needs to follow this modified path. Figure 17 shows the vorticity flux and circulation around a streamline that wraps around the island group *and* the anticyclone. Following this modified integration path shows that the circulation cell is indeed in near-phase with the Reynolds flux forcing. The figure also shows the average azimuthal velocity integrated along

https://doi.org/10.5194/os-2021-41
Preprint. Discussion started: 26 May 2021

Ocean Science
Discussions
Open Access
EGU

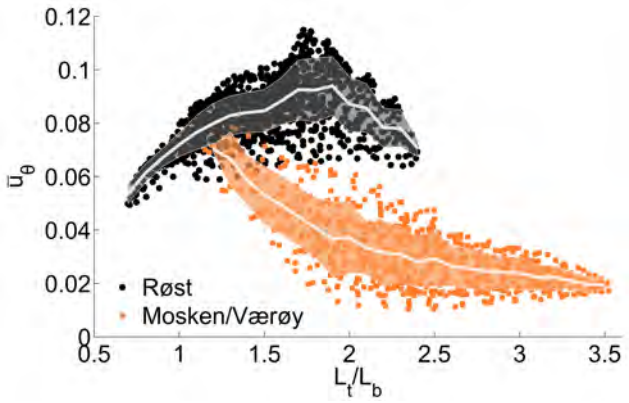

Figure 16. The strength of the rectified tidal currents around Røst (black dots) and around Mosken and Værøy (organge dots) are plotted against the ratio L_T/L_B averaged around closed depth contours. Each dot correspond to a time mean velocity averaged over one tidal cycle. The bright thicker lines show the mean values of the residual tidal current corresponding to a given value of L_T/L_B +/- 0.1. Shading indicates one standard deviation around the mean.

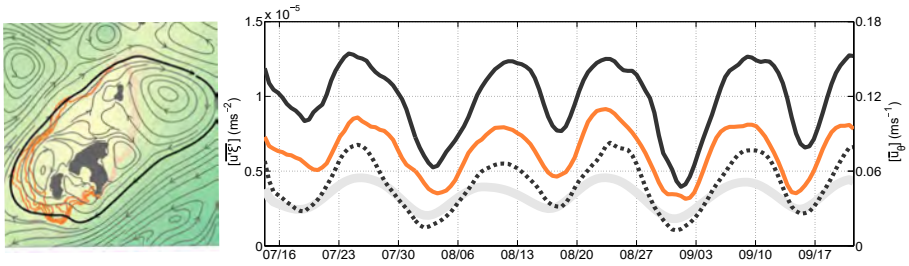

Figure 17. Close-up of the flow field around around Mosken-Værøy. The left panel shows time-mean streamlines (gray contours with arrow heads) as well as a set of depth contours that wrap around the island group (orange contours). The right panel shows the Reynolds vorticity flux (dashed black line) through one closed streamline which wraps around the island group and the anticylone east of Mosken (thick black contour in left panel). Also shown is the circulation around the same contour (solid black line) as well as the circulation along an incomplete depth contour south and west of the island group (orange solid line). The sea surface height variation is shown with thick light gray line.

an incomplete stretch of the original depth contours, south and west of the island group. The flow here is also in near phase with the spring-neap variations. So the circulation cell around the island group is forced by Reynolds vorticity fluxes, by the mechanism outlined above. But the strong nonlinearity in Moskstraumen makes the dynamics more complex than around the
480 island of Røst to the south.

https://doi.org/10.5194/os-2021-41
Preprint. Discussion started: 26 May 2021

4 Summary and conclusions

While the tides in Lofoten-Vesterålen are well known to be strong and vigorous, dominating the short-term ocean dynamics, particularly in straits and around topographic features (Gjevik et al., 1997; Moe et al., 2002), their contribution to long-term transport has gained relatively little attention. The one notable exception is Moskstraumen which is recognized as one of the main transport routes out of Vestfjorden (Ommundsen, 2002; Vikebø et al., 2007; Opdal et al., 2008; Lynge et al., 2010). Our unstructured-grid tidal simulations of the entire Lofoten-Vesterålen region confirms that Moskstraumen and, more generally, the region off the southern tip of the Lofoten archipelago is indeed the primary location for tidal dispersion in this key spawning region for the Northeast arctic cod. The main focus of this study, however, has not been quantification of transport but rather the identification of the underlying nonlinear dynamics responsible for dispersion and transport.

The flexible model grid, and the ability it offers to increase resolution in key regions, allowed us to confirm that tidal pumping, caused by flow separation and vortex dipole formation at the openings of the many straits in Lofoten-Vesterålen, is a near-ubiquitous process here. But not all straits are created equal. Strong non-linearity due to high flow speeds and abrupt strait openings, as well as short strait lengths, appears to be the explanation for why Moskstraumen and Nordlandsflaget have the highest tidal transport efficiencies in the region. The longer straits further north all have lower pumping efficiencies. But notable pumping also takes place in Nappstraumen and Gimsøystraumen.

Our simulation also revealed non-linear rectification of tidal oscillations, leading to the generation of time-mean anticyclonic circulation cells around the island groups of Mosken-Værøy and Røst off the southern tip of the archipelago. From our knowledge, tidal rectification in southern Lofoten has neither been investigated nor recognized before. But the observed rectification in our model seems to be in agreement with well-established theory of vorticity fluxes driven by cross-topographic tidal oscillations in the presence of bottom friction. The model predicted rectified current speeds up to 0.3–0.4 m/s, values that are comparable with observed background currents in this region. The circulation cell around Røst appears to be a particularly important and hitherto unknown mechanism for tracer transport around the southern tip of the archipelago.

The nonlinear tidal dynamics studied here, particularly flow separation and dipole formation, occurs on small spatial scales. In studying idealized model simulations of tidal pumping, Nøst and Børve (2021) found that a grid resolution of 50 m along the coast was necessary to realistically capture flow separation in the viscous boundary layer, but maybe not sufficient to properly resolve the vortices that form at the separation point. More specifically, the study showed that the vortices consistently formed near the smallest scale that could be resolved by that model. Lynge et al. (2010) also found that particle dispersion in realistic model simulations of Moskstraumen was highly sensitive to grid resolution and that a resolution of 50–100 m was needed for obtaining what they reported to be realistic dispersion rates. In our unstructured-grid model most of the straits had a grid resolution of 30–50 m near the coastline, so the underlying mechanisms of flow separation and vortex formation were fairly well resolved. However, due to computational constraints we had to decrease the resolution considerably away from the straits and coastlines. So since the properties and behavior of the dipoles might be influenced by grid resolution along their travel path, we expect our simulations as well to be hampered by resolution issues. Thus, we refrained from making quantitative estimates

https://doi.org/10.5194/os-2021-41
Preprint. Discussion started: 26 May 2021

of transport parameters like relative dispersion and lateral diffusivities, which are known to be sensitive to model resolution (Geyer and Signell, 1992; LaCasce, 2008; Lynge et al., 2010).

Our simulations were also limited by their 2D nature. A 2D configuration was chosen to help isolate nonlinear lateral tidal dynamics, but the model was thus unable to account for baroclinic effects, e.g. the possible generation of hydraulic jumps and vertical mixing around strait openings (Lynge et al., 2010) or the establishment of density fronts around the rectification cells (Ou, 2000). In reality, baroclinic flow dynamics will impact tracer transport, both vertically and laterally. But key features of the model's lateral flow dynamics appears to be robust. Flow separation and dipole formation in Moskstraumen, for example, is largely in agreement with observational evidence, seen e.g. in satellite data (Figure 2). The suggestion that there are anticyclonic time-mean currents around the island groups of Mosken-Værøy and Røst, generated by tidal rectification, is however worthy of a new and dedicated observational study.

Notwithstanding model limitations, the present study supports previous claims that tides are an important contributor to the transports of Northeast Arctic cod eggs and larvae out of Vestfjorden. Even if the main transport routes due to tides coincide with transport routes following the mean flow, i.e. through Moskstraumen and south of Røst, the net transport could potentially be significantly enhanced when nonlinear tidal dynamics are present. In truth, the connectivity between the inner and outer shelf likely relies on the *interaction* between tidal dispersion and transport by the time-mean currents (Ommundsen, 2002). Additionally, our study suggests that tidal pumping through straits further north along the archipelago, in particular Nappstraumen and Gimsøystraumen, could provide alternative transport routes to the shelf. In an on-going study, we analyze 3D unstructured-grid simulations driven by realistic atmospheric, river and lateral boundary forcing. The aim there is to investigate the relative importance of tidally-induced transport of cod eggs and larvae compared to, or in combination with, other transport processes in this region. The more realistic 3D study will hopefully also add to the general understanding of the role of nonlinear tidal dynamics in similar coastal regions, with the ultimate aim of providing more accurate transport estimates of fish eggs and larvae, as well as pollutants, nutrients and other properties that affect the coastal ecosystem.

Data availability. Data is available on request

Appendix A: A one-dimensional model of tidal rectification

We consider the Lagrangian time evolution of a water column subject to linear bottom friction:

$$\frac{D}{Dt}\left(\frac{f+\xi}{H}\right) = -\frac{1}{H}\nabla \times \frac{R\boldsymbol{u}}{H}. \tag{A1}$$

For simplicity we will assume that the RHS is dominated by velocity gradients, giving

$$\frac{D}{Dt}\left(\frac{f+\xi}{H}\right) = -\frac{R}{H^2}\xi. \tag{A2}$$

As formally laid out by e.g. (Zimmerman, 1978), we now consider the situation where the column is forced to move up and down topography by tidal currents that are dictated by remote dynamics. Thus, $H = H(t)$ is specified. The relative vorticity

https://doi.org/10.5194/os-2021-41
Preprint. Discussion started: 26 May 2021


Ocean Science Discussions

ξ however is assumed to be a local response to the vortex compression/stretching by this movement across topography and to the effects of friction.

Equation (A2) can be written out to give a first-order ordinary differential equation:

$$\frac{D\xi}{Dt} - \left(\frac{1}{H}\frac{DH}{Dt} - \frac{R}{H}\right)\xi = \frac{f}{H}\frac{DH}{Dt}. \tag{A3}$$

This takes the form of a forced equation for ξ with damping, where the damping coefficient is non-constant. We now define

$$p(t) = \frac{1}{H}\frac{DH}{Dt} - \frac{R}{H}, \tag{A4}$$

and multiply (A3) by $\exp\left(-\int p(t)\,dt\right) = \exp\left(\int R/H\,dt\right)/H$ before integrating in time. The expression becomes (after applying integration by parts to both sides):

$$\int_0^t \frac{D}{Dt}\left(\frac{\xi}{H}e^{\int R/H\,dt}\right)dt = -\int_0^t \frac{D}{Dt}\left(\frac{f}{H}e^{\int R/H\,dt}\right) + \int_0^t \frac{fR}{H^2}e^{\int R/H\,dt}\,dt, \tag{A5}$$

and the solution is

$$\xi(t) = \underbrace{(\xi_0 + f)\frac{H}{H_0}e^{-\int_0^t R/H\,dt}}_{\text{T-I}} \underbrace{- f\left[1 - RHe^{-\int_0^t R/H\,dt}\int_0^t \frac{1}{H^2}e^{\int_0^t R/H\,dt}\,dt\right]}_{\text{T-II}}, \tag{A6}$$

where ξ_0 and H_0 are the relative vorticity and bottom depth at $t = 0$. Here terms T-I describe an exponentially-decaying adjustment from the initial state, whereas terms T-II describe a part of the solution which achieves statistical equilibrium with the forcing. After a few tidal cycles $\exp\left(-\int_0^t R/H\,dt\right) \to \exp(-rt)$, where r is an inverse time scale for the adjustment from initial to steady state. As seen, this spin-up time scale depends on the friction coefficient and the bottom depth variations experienced by the column.

We now evaluate (A6) numerically for a very simplified configuration consisting of forced flow over a linear topography, i.e. for $H = H_0 - \alpha r(t)$, where α is the bottom slope and $r(t)$ is the cross-slope excursion from $r(t = 0)$ where $H = H_0$. For added simplicity we assume a sinusoidal cross-slope tidal current, $v_r(t) = A\cos(\omega t)$ for tidal amplitude A and frequency ω, so that $H(t)$ also becomes sinusoidal. A solution, for parameter choices $\xi_0 = 0$, $H_0 = 500\,\mathrm{m}$, $\alpha = 0.1$, $A = 0.5\,\mathrm{m\,s^{-1}}$, $\omega = 1.4 \times 10^{-4}\,\mathrm{rad\,s^{-1}}$ (M2) and $R = 0.003\,\mathrm{m\,s^{-1}}$, is shown in Figure A1. The relative vorticity of the water column reaches a statistically-steady state after about 10 tidal periods (about 5 days for M2 tidal forcing), this corresponding to 2–3 e-folding scales. The column then has positive and negative relative vorticity over deep and shallow parts, respectively. The amplitude is largest over deep parts due to the inverse dependence of depth in the friction term (see eqn. A2). Interpolating this vorticity field to mid-depth ($H = H_0$) and taking the product of the velocity gives the Eulerian vorticity flux. The result is shown in Figure A2 for two choices of bottom friction R and five choices of initial vorticity ξ_0. The initial vorticity flux can be up or down the slope, depending on ξ_0. But after the initial adjustment period (which depends inversely on R), the end result is always a positive vorticity flux towards deep water. The magnitude of the flux is linearly proportional to R, as can be deduced from (A6).

https://doi.org/10.5194/os-2021-41
Preprint. Discussion started: 26 May 2021

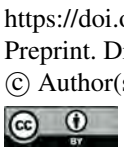

Ocean Science
Discussions
Open Access
EGU

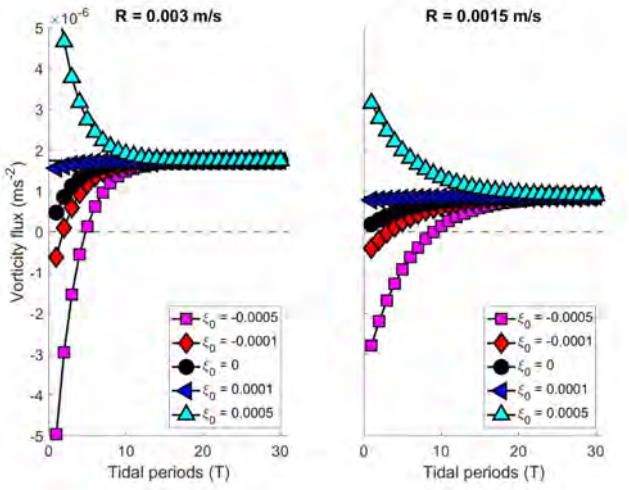

Figure A1. Vorticity evolution of a water column forced to oscillate over a linear bottom slope, for $\xi_0 = 0$, $H_0 = 500\,\mathrm{m}$, $\alpha = 0.1$, $A = 0.5\,\mathrm{m\,s^{-1}}$, $\omega = 1.4 \times 10^{-4}\,\mathrm{rad\,s^{-1}}$ (for M2) and $R = 0.003\,\mathrm{m\,s^{-1}}$. The red line is the transient solution (terms T-I in eqn. A6), the blue line is the statistically-steady solution (terms T-II) and the black line is the full solution.

https://doi.org/10.5194/os-2021-41
Preprint. Discussion started: 26 May 2021

Ocean Science
Discussions
Open Access
EGU

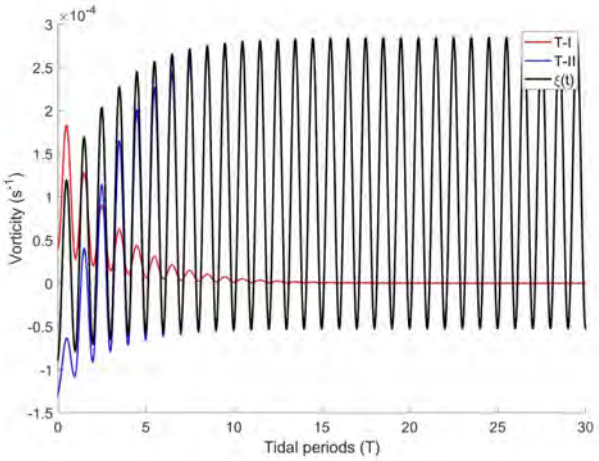

Figure A2. Vorticity flux averaged over an integral number of tidal period as a function of time, for the solution of (A6). Positive values indicate a vorticity flux towards deep waters. The left and right panels show results for $R = 0.003\,\mathrm{m/s}$ and $R = 0.0015\,\mathrm{m/s}$, respectively, starting from five different initial vortices ξ_0. The other parameters are as in Figure A1.

Author contributions. OAN and EB sat up the numerical model. EB conducted the numerical experiments and analyzed the data. All authors contributed in discussing and interpreting the results. EB and PEI wrote the initial paper draft and all authors have been contributing in editing the paper.

Competing interests. No competing interest are present

Acknowledgements. We thank Trygve Halsne for providing the processed satellite images of Moskstraumen and Nordlandsflaget in Figure 2. E. Børve was funded by VISTA – a basic research program in collaboration between The Norwegian Academy of Science and Letters, and Equinor (project no.6168).

https://doi.org/10.5194/os-2021-41
Preprint. Discussion started: 26 May 2021

References

Afanasyev, Y. D.: Formation of vortex dipoles, Physics of Fluids, 18, https://doi.org/10.1063/1.2182006, 2006.

Bretherton, F. P. and Haidvogel, D. B.: Two-dimensional turbulence above topography, Journal of Fluid Mechanics, 78, 129–154, https://doi.org/10.1017/S002211207600236X, 1976.

Bruggeman, J. and Bolding, K.: A general framework for aquatic biogeochemical models, Environmental Modelling & Software, 61, 249–265, https://doi.org/10.1016/j.envsoft.2014.04.002, 2014.

Chen, C., Liu, H., and Beardsley, R. C.: An Unstructured Grid, Finite-Volume, Three-Dimensional, Primitive Equations Ocean Model: Application to Coastal Ocean and Estuaries, Journal of Atmospheric and Oceanic Technology, 20, 159–186, https://doi.org/10.1175/1520-0426(2003)020<0159:AUGFVT>2.0.CO;2, 2003.

Chen, C., Huang, H., Beardsley, R. C., Xu, Q., Limeburner, R., Cowles, G. W., Sun, Y., Qi, J., and Lin, H.: Tidal dynamics in the Gulf of Maine and New England Shelf: An application of FVCOM, Journal of Geophysical Research: Oceans, 116, https://doi.org/10.1029/2011JC007054, 2011.

Chen, C., Beardsley, R. C., Cowles, G., Qi, J., Lai, Z., Gao, G., Stuebe, D., Liu, H., Xu, Q., Xue, P., Ge, J., Hu, S., Ji, R., Tian, R., Huang, H., Wu, L., Lin, H., Sun, Y., and Zhao, L.: An Unstructured Grid, Finite-Volume Coastal Ocean Model: FVCOM User Manual, version 3.1.6, Marine Ecosystem Dynamics Modeling Laboratory, 4 edn., 2013.

Egbert, G. D. and Erofeeva, S. Y.: Efficient Inverse Modeling of Barotropic Ocean Tides, Journal of Atmospheric and Oceanic Technology, 19, 183–204, https://doi.org/10.1175/1520-0426(2002)019<0183:EIMOBO>2.0.CO;2, 2002.

Ellertsen, B., Solemdal, P., Strømme, T., Sundby, S., Tilseth, S., and Westgård, T.: Spawning period, transport and dispersal of eggs from the spawning area of Arcto-Norwegian cod (Gadus morhua L.), Rapp. P.-v. Reun. Cons. int. Explor. Mer, 178, 260–267, 1981.

Geyer, W. R. and Signell, R. P.: A reassessment of the role of tidal dispersion in estuaries and bays, Estuaries, 15, 97–108, 10.2307/1352684, 1992.

Geyer, W. R., Woodruff, J. D., and Traykovski, P.: Sediment transport and trapping in the Hudson River estuary, Estuaries, 24, 670–679, https://doi.org/10.2307/1352875, 2001.

Gjevik, B., Moe, H., and Ommundsen, A.: Sources of the Maelstrom, Nature, 388, 837–838, https://doi.org/10.1038/42159, 1997.

Halsne, T., Ferrighi, L., Saadatnejad, B., Budewitz, N., Dinessen, F., Breivik, L.-A., and Godøy, Ø´.: The Norwegian National Ground Segment; Preservation, Distribution and Exploitation of Sentinel Data, Data Science Journal, 18, 61, https://doi.org/10.5334/dsj-2019-061, 2019.

Hjermann, D. Ø., Melsom, A., Dingsør, G. E., Durant, J. M., Eikeset, A. M., Røed, L. P., Ottersen, G., Storvik, G., and C., S. N.: Fish and oil in the Lofoten-Barents Sea system: synoptic review of the effects of oil spill on fish populations, Marine Ecology Progress Series, 339, 238–299, https://doi.org/10.3354/meps339283, 2007.

Hjort, J.: Fluctuations in the great fisheries of northern Europe viewed in the light of biological research, Conseil Permanent International Pour L'Exploration De La Mer, 1914.

Houde, E. D.: Emerging from Hjort's shadow, Journal of Northwest Atlantic Fishery Science, 41, 53–70, https://doi.org/10.2960/J.v41.m634, 2008.

Huthnance, J. M.: Tidal current asymmetries over the Norfolk Sandbanks, Estuarine and Coastal Marine Science, 1, 89–99, https://doi.org/10.1016/0302-3524(73)90061-3, 1973.

https://doi.org/10.5194/os-2021-41
Preprint. Discussion started: 26 May 2021

Isachsen, P. E., LaCasce, J. H., Mauritzen, C., and Häkkinen, S.: Wind-Driven Variability of the Large-Scale Recirculating Flow in the Nordic Seas and Arctic Ocean, Journal of Physical Oceanography, 33, 2534–2550, https://doi.org/10.1175/1520-0485(2003)033<2534:WVOTLR>2.0.CO;2, 2003.

Kashiwai, M.: Tidal Residual Circulation Produced by a Tidal Vortex. Part 1. Life-History of a Tidal Vortex, Journal of the Oceanographical Society of Japan, 40, 279–294, https://doi.org/10.1007/BF02302521, 1984.

Kobayashi, M. H., Pereira, J. M., and Pereira, J. C.: A conservative finite-volume second-order-accurate projection method on hybrid unstructured grids, Journal of Computational Physics, 150, 40–75, https://doi.org/10.1006/jcph.1998.6163, 1999.

Kundu, P. K., Cohen, I. M., and Dowling, David R. Tryggvason, G.: Fluid Mechanics, Academic Press, sixth edn., 2016.

LaCasce, J. H.: Statistics from Lagrangian observations, Progress in Oceanography, 77, 1–29, https://doi.org/10.1016/j.pocean.2008.02.002, 2008.

Loder, J. W.: Topographic rectification of tidal currents on the sides of Georges Bank, Journal of Physical Oceanography, 10, 1399–1416, https://doi.org/10.1175/1520-0485(1980)010<1399:TROTCO>2.0.CO;2, 1980.

Lynge, B. K., Berntsen, J., and Gjevik, B.: Numerical studies of dispersion due to tidal flow through Moskstraumen, northern Norway, Ocean Dynamics, 60, 907–920, https://doi.org/10.1007/s10236-010-0309-z, 2010.

Maas, L., Zimmerman, J. T. F., and Temme, N. M.: On the exact shape of the horizontal profile of a topographically rectified tidal flow, Geophysical & Astrophysical Fluid Dynamics, 38, 105–129, https://doi.org/10.1080/03091928708210107, 1987.

Moe, H., A., O., and B., G.: A high resolution tidal model for the area around The Lofoten Islands, northern Norway, Continental Shelf Research, 22, 485–504, https://doi.org/10.1016/S0278-4343(01)00078-4, 2002.

Mork, M.: Experiments with theoretical models of the Norwegian Coastal Current, in: The Norwegian Coastal Current, edited by Sætre, R. and M., M., vol. 2, pp. 518–530, University of Bergen, 1981.

Norwegian Mapping Authority, Hydrographic Service: API for water level data, https://api.sehavniva.no/tideapi_en.html, CC BY 4.0, 2021.

Nøst, O. A. and Børve, E.: Flow separation, dipole formation and water exchange through tidal straits, Ocean Science Discussions, 2021, 1–34, https://doi.org/10.5194/os-2021-30, 2021.

Ommundsen, A.: Models of cross shelf transport introduced by the Lofoten Maelstrom, Continental Shelf Research, 22, 93–113, https://doi.org/10.1016/S0278-4343(01)00069-3, 2002.

Ommundsen, A. and Gjevik, B.: Scattering of tidal Kelvin waves along shelves which vary in their lengthwise direction, Preprint series. Mechanics and Applied Mathematics, http://urn.nb.no/URN:NBN:no-28523, 2000.

Opdal, A. F., Vikebø, F. B., and Fiksen, Ø.: Relationships between spawning ground identity, latitude and early life thermal exposure in Northeast Arctic cod, Journal of Northwest Atlantic Fishery Science, 41, 13–22, https://doi.org/10.2960/J.v41.m621, 2008.

Ou, H.-W.: A Model of Tidal Rectification by Potential Vorticity Mixing. Part I: Homogeneous Ocean, Journal of Physical Oceanography, 29, 821–827, https://doi.org/10.1175/1520-0485(1999)029<0821:AMOTRB>2.0.CO;2, 1999.

Ou, H.-W.: A Model of Tidal Rectification by Potential Vorticity Mixing. Part II: Frontal Regime, Journal of Physical Oceanography, 30, 564–571, https://doi.org/10.1175/1520-0485(2000)030<0564:AMOTRB>2.0.CO;2, 2000.

Parker, B. B.: The relative importance of the various nonlinear mechanisms in a wide range of tidal interactions, chap. 13, pp. 237–268, John Wiley and sons, inc., 1991.

Pingree, R. D. and Maddock, L.: Rotary currents and residual circulation around banks and islands, Deep Sea Research Part A. Oceanographic Research Papers, 32, 1, https://doi.org/10.1016/0198-0149(85)90037-8, 1985.

https://doi.org/10.5194/os-2021-41
Preprint. Discussion started: 26 May 2021

Polton, J. A.: Tidally induced mean flow over bathymetric features: a contemporary challenge for high resolution wide-area models, Geophysical & Astrophysical Fluid Dynamics, 109, 207–215, https://doi.org/10.1080/03091929.2014.952726, 2015.

Robinson, I. S.: Tidal vorticity and residual circulation, Deep Sea Research Part A. Oceanographic Research Papers, 28, 195–212, https://doi.org/10.1016/0198-0149(81)90062-5, 1981.

Röhrs, J.: Surface wave effects in theupper ocean and consequences for biologican modeling, Ph.D. thesis, University of Bergen, 2014.

Röhrs, J., Christensen, K. H., Vikebø, F., Sundby, S., Sætra, Ø., and Broström, G.: Wave-induced transport and vertical mixing of pelagic eggs and larvae, Limnology and oceanography, 59, 1213–1227, https://doi.org/10.4319/lo.2014.59.4.1213, 2014.

Signell, R. P. and Butman, B.: Modeling tidal exchange and dispersion in Boston Harbor, Journal of Geophysical Research: Oceans, 97, 15 591–15 606, https://doi.org/10.1029/92JC01429, 1992.

Signell, R. P. and Geyer, R.: Transient eddy formation around headlands, Journal of Geophysical Research, 96, 2561–2575, https://doi.org/10.1029/90JC02029, 1991.

Smagorinsky, J.: General circulation experiments with the primitive equations: I. The basic experiment, Monthly weather review, 91, 99–164, https://doi.org/10.1175/1520-0493(1963)091<0099:GCEWTP>2.3.CO;2, 1963.

Stommel, H. and Farmer, H. G.: On the nature of eustarine circulation. Part I (Chapters 3 and 4), techreport 52–88, Woods Hole Oceanographic Institution MA, 1952.

Sundby, S. and Bratland, P.: Spatial distribution and production of eggs from North-East Arctic cod at the coast of northern Norway 1983–1985, Report series Fisken og Havet., 1, 1987.

Vikebø, F., Jørgensen, C., Kristiansen, T., and Fiksen, Ø.: Drift, growth, and survival of larval Northeast Arctic cod with simple rules of behaviour, Marine Ecology Progress Series, 347, 207–219, https://doi.org/10.3354/meps06979, 2007.

Wells, M. G. and van Heijst, G.-J. F.: A model of tidal flushing of an estuary by dipole formation, Dynamics of Atmospheres and Oceans, 37, 223–244, https://doi.org/10.1016/j.dynatmoce.2003.08.002, 2003.

Wright, D. G. and Loder, J. W.: A depth-dependent study of the topographic rectification of tidal currents, Geophysical & Astrophysical Fluid Dynamics, 31, 169–220, https://doi.org/10.1080/03091928508219269, 1985.

Zimmerman, J. T. F.: Topographic generation of residual circualtion by oscialltory (tidal) currents, Geophysical & Astrophysical Fluid Dynamics, 11, 35–47, https://doi.org/10.1080/03091927808242650, 1978.

Zimmerman, J. T. F.: Dynamics, diffusion and geomorphological significance of tidal residual eddies, Nature, 290, 549–555, https://doi.org/10.1038/290549a0, 1981.

Ådlandsvik, B. and Sundby, S.: Modelling the transport of cod larvae from the Lofoten area, ICES Mar Sci Symp, 198, 379–392, 1994.

Paper III

Diurnal continental shelf waves with a permeable coastal boundary: Application to the shelf northwest of Norway

Jan Erik H. Weber and **Eli Børve**
European Journal of Mechanics / B Fluids, 2021
10.1016/j.euromechflu.2021.05.003

III

European Journal of Mechanics / B Fluids 89 (2021) 64–71

Contents lists available at ScienceDirect

European Journal of Mechanics / B Fluids

journal homepage: www.elsevier.com/locate/ejmflu

Diurnal continental shelf waves with a permeable coastal boundary: Application to the shelf northwest of Norway

Jan Erik H. Weber [a,*], Eli Børve [a,b]

[a] Department of Geosciences, University of Oslo, Norway
[b] Akvaplan-Niva AS, Fram Centre, Tromsø, Norway

ARTICLE INFO

Article history:
Received 25 March 2021
Accepted 7 May 2021
Available online 11 May 2021

Keywords:
Diurnal waves
Lagrangian drift
Permeable boundary
Robin condition

ABSTRACT

Spatially damped continental shelf waves (CSWs) with diurnal tidal frequency outside Lofoten–Vesterålen in north-west Norway are studied theoretically for an idealized shelf topography. Wave damping is caused by the exchange of fluid on the shelf with an inner archipelago through a permeable coastline. This exchange is modelled by the application of a Robin condition at the coastal boundary. It is shown that CSWs with diurnal frequencies are possible in a small wave number range centred around zero group velocity. By calculating the nonlinear radiation stress components in the spatially damped CSWs, we find the time- and depth averaged Lagrangian mean drift current to second order along the coast. We show that the Lagrangian mean drift current is independent of the value of the damping coefficient, however small, as long as it is nonzero. This illustrates the singular behaviour of the Lagrangian wave drift problem for CSWs.

1. Introduction

We study sub-inertial wave motion over variable bottom topography. Longuet-Higgins [1,2] has described how such waves can propagate along a sloping bottom. The focus here is on wave motion along a continental shelf that is limited laterally by a coastal boundary; see e.g. Buchwald and Adams [3]. Such waves have become known as continental shelf waves (CSWs). The classic investigation on how CSWs are generated by the wind is that of Gill and Schumann [4]. We here focus on the shelf west of Norway. Traditionally, wind systems hitting the southwestern part of Norway has a storm track with an oblique angle to the coast. This generates CSWs that propagate northward along the Norwegian continental shelf, see e.g. [5] and [6]. These generation events are more frequent (and stronger) in the autumn and the winter, but they are in all cases sporadic.

A more regular mechanism for the generation of CSWs is the tidal diurnal motion, in particular, strong tidal motion through straits. We here refer to [7–9] for the generation of CSWs along the Australian shelf from tides in the Bass Strait. Even in cases without a strait, CSWs with diurnal tidal frequency may be generated on the shelf slope if the local group velocity is close to zero due to changes in topography; see [10] for the shelf near St. Kilda in the UK, and [11] for the Greenland shelf.

In north Norway, the tidally driven Moskstraumen is a clear parallel to the tidal motion in the Australian Bass strait, pressing water back and forth across the depth contours of the shelf outside Lofoten. The cross-shelf transport has been modelled in [12]. For the interested reader, Moskstraumen is the famously strong Lofoten Maelstrom with written accounts back to mediaeval times; see Gjevik et al. [13]. In Fig. 1 we have inserted a map of the Norwegian coastal area, with special reference to the Lofoten–Vesterålen region.

Usually, in modelling CSWs, the coastline is taken to be a solid wall. However, along the Norwegian coast there are a myriad of small islands and narrow fjords with a lateral scale much smaller than the CSW wavelength, as is evident from Fig. 1. Hence, since CSWs have a velocity component normal to the depth contours, which usually follows the coastline, there will be an exchange of fluid between the shelf and the narrow fjords and small islands. In the fjord system, the dissipation will be considerable. This will remove energy from the CSW, and lead to spatial damping as the wave propagates along the shelf slope. We note that this phenomenon is a clear parallel to the damping of surface waves over a permeable seabed by Reid and Kajiura [14]; see also [15] for surface waves over coral reefs.

We demonstrate that a non-zero velocity normal to the coastline inevitably will lead to a spatial damping of the CSWs. This is done by applying a Robin condition [16,17] at the coastal boundary. The Robin condition is a weighted combination of Dirichlet boundary conditions and Neumann boundary conditions and is common in many branches of physics. The Robin condition, through a small parameter, allows for a small velocity normal to the coastline, which is exactly what happens when we have

* Corresponding author.
E-mail address: j.e.weber@geo.uio.no (J.E. Weber).

https://doi.org/10.1016/j.euromechflu.2021.05.003

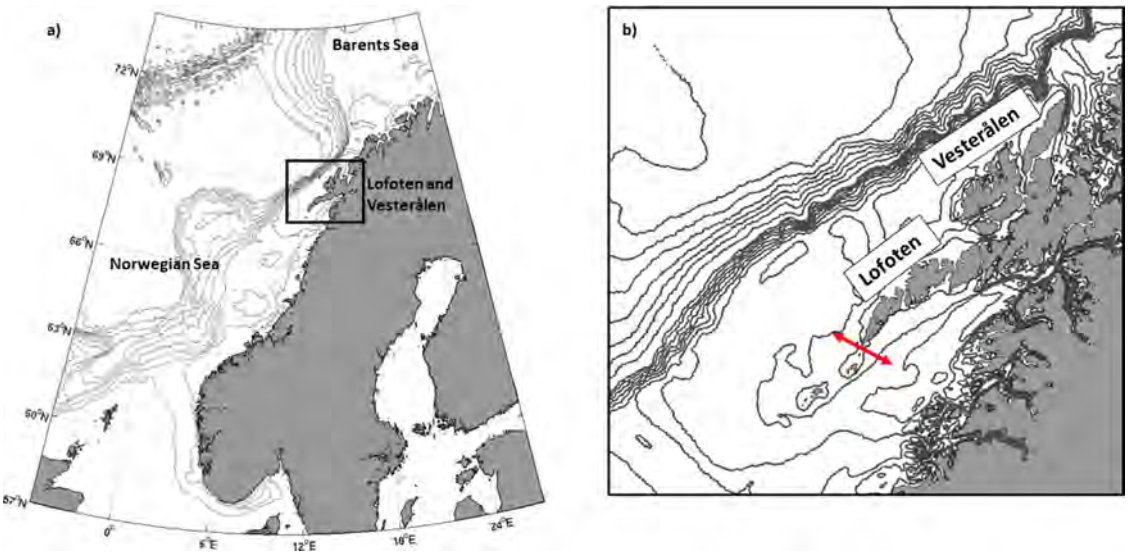

Fig. 1. (a) Map of the Norwegian coastal area with bottom contours. The relevant region here is the narrow shelf outside Lofoten and Vesterålen. (b) Close-up of the Lofoten–Vesterålen region where a red arrow indicates the position of Moskstraumen.

an inner archipelago with narrow fjords and small islands. The damping rate is then obtained as a function of the small Robin parameter.

As pointed out by Phillips [18], the vertically integrated flow between material surfaces (bottom and free surface) yields the Lagrangian volume fluxes. These fluxes are forced by the radiation stresses; see [19]. Weber and Drivdal [20] calculate the Lagrangian mean drift when the wave decay is due to bottom friction, which also affects the mean flow. Similar calculations are made in the present paper, where the wave decay is due to the nonzero flux condition at the permeable coastal boundary. Now the sloping shelf region is taken to be inviscid. This simplifies the calculation of the Lagrangian mean drift current, which is discussed for parameters that are typical for the shelf outside Lofoten.

2. Linear analysis for idealized bottom profiles and an impermeable coastal wall

We first discuss the presences of CSWs with diurnal frequency outside Lofoten–Vesterålen with the usual adoption of a solid coastal wall. In a forthcoming paper [21], it is found from a barotropic numerical model for tidal motion that a distinct amplification of the current speed occurs in the Lofoten–Vesterålen region for the diurnal K_1 tidal component. This is shown in Fig. 2, where the intensity of the red colour marks the areas with prominent K_1 tidal current amplification. The amplification of the K_1 tidal current through Moskstraumen is closely related to the distortion of the northward propagating tidal wave when it interacts with the Lofoten archipelago. The tidal wave is scattered and deflected around the island chain resulting in an east–west pressure gradient in the southern Lofoten, which enhances the tidal flow through Moskstraumen. The tidal flow is forced across the shallow ridge extending southwestward from the archipelago, which further enhances the current speed amplitude. Outside Vesterålen, on the other hand, the amplification in the K_1 tidal current amplitude cannot be explained by topographic features along the narrow and shallow shelf. Here, the K_1 amplification has been attributed to generation/conversion to continental shelf waves with diurnal frequency [22,23].

The places of particular interest here are the steep shelf regions outside Vesterålen; see Fig. 1b. For a closer study, we have chosen three particular transects, depicted in Fig. 3.

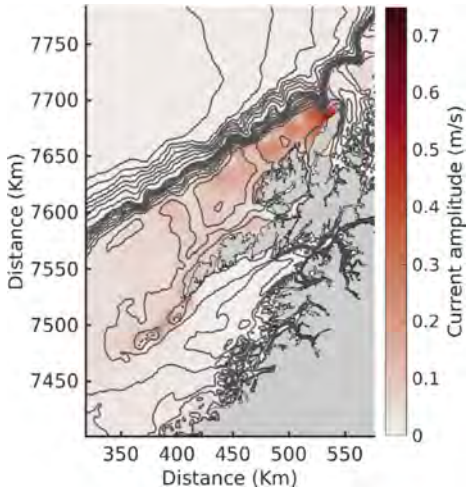

Fig. 2. Current speed amplification for the diurnal K_1 tidal component near Moskstraumen and along the shelf outside Vesterålen, based on Fig. 2 in [21].

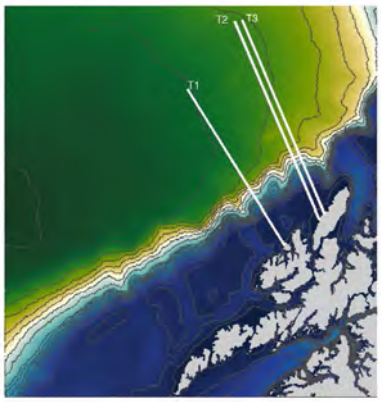

Fig. 3. Positions of transects T1, T2, T3 across the shelf outside Vesterålen.

We idealize the shelf geometry as in [3], but allow for a small flat inner shelf of width D and depth H_0, before the depth

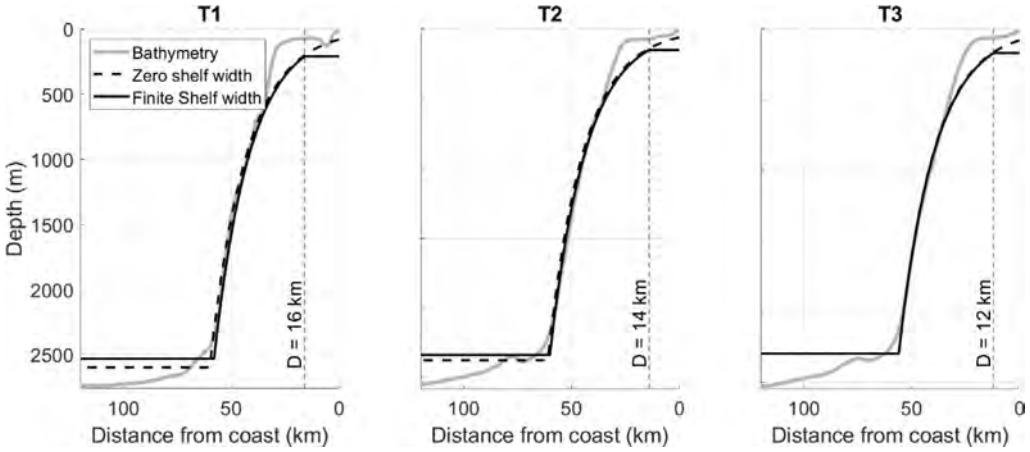

Fig. 4. Bottom profiles in transects T1, T2, T3 in Fig. 3.

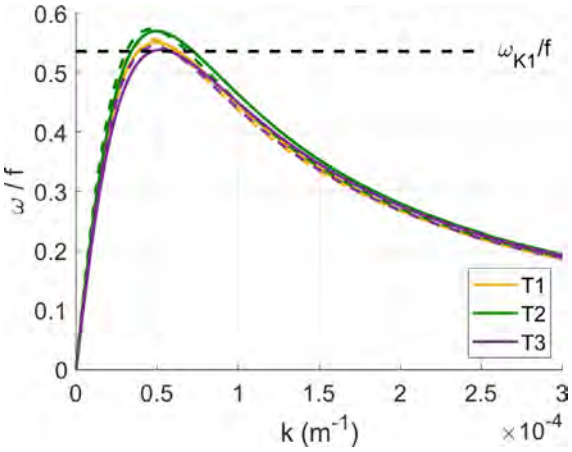

Fig. 5. Dispersion diagrams for transects T1, T2, T3 outside Vesterålen (first mode), showing non-dimensional frequency ω/f *vs* wave number k. Here f is the constant Coriolis parameter. Solid lines represent an inner shelf where $D \neq 0$, and dashed lines the case when $D = 0$. The upper horizontal dashed line is the non-dimensional tidal frequency for the K_1 component.

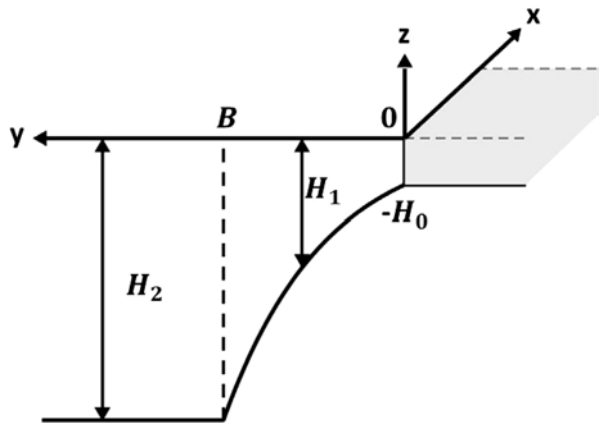

Fig. 6. A diagram showing the configuration with an exponential shelf, continued by a flat deep ocean. The shelf edge is located at $y = B$. The coastline at $y = 0$ is permeable (indicated by grey shading) and modelled by a Robin condition.

increases exponentially towards the deep ocean; see [6] and [11]. We place the x axis along the coast. The y axis is directed towards the sea, and the z axis is vertically upwards. The bottom profile is given by

$$H = \begin{cases} H_0, & -D \le y \le 0 \\ H_1 = H_0 \exp(2by), & 0 \le y \le B \\ H_2 = H_0 \exp(2bB), & y \ge B. \end{cases} \quad (1)$$

Here b is a constant describing the steepness of the slope, and B is the width of the sloping shelf.

Outside Vesterålen the flat part of the shelf is narrow, and we present the bottom profiles in Fig. 4 from transects T1, T2, T3 with a small D (solid black lines), and with $D = 0$ (dashed lines).

We use the analysis in [6] to compute the dispersion diagrams for the idealized exponential bottom profiles in Fig. 4. The results are depicted in Fig. 5.

We note from Fig. 5 that the effect on frequency of a narrow inner shelf is practically negligible in the region outside Vesterålen. More importantly, CSWs with a frequency corresponding to the diurnal K_1 component of the tidal motion are possible, as seen from the intersections with the upper broken line in Fig. 5. Furthermore, we note that at all transects the group velocity is close to zero for the diurnal frequency, which is similar to the findings in [11] for the Greenland shelf. This means that wave energy accumulates in the region, which may explain the current amplification along the shelf in Fig. 2. The existence of short CSWs on the shelf outside Vesterålen with diurnal frequency has also been reported by Moe et al. [22].

3. Linear waves with a robin condition at the coast

Having established that CSWs with a diurnal frequency may form in the Lofoten–Vesterålen region, we proceed to investigate some non-linear properties of these waves. For a solid coastal wall at $y = 0$, this problem has been studied in [20]. However, it is fair to say that the western coast of Norway bordering the continental shelf is far from impermeable. We note from Fig. 1 that this region contains a myriad of narrow fjords and small islands through which the shelf water may intrude. Therefore, we adapt a novel approach, and take that the coastal boundary is partly permeable. This has important consequences for the wave-induced drift, as will be shown in the following sections.

The linear wave problem starts out in a classic fashion [3,4]. We have already shown that the effect of a narrow, flat inner shelf outside Lofoten can be neglected. Our idealized shelf geometry is therefore as in [3] with $D = 0$, see (1), but we now introduce a novel feature at the coast. Here we apply a Robin condition [16, 17] to model a permeable boundary (see Fig. 6).

The Robin condition is a weighted combination of Dirichlet boundary conditions and Neumann boundary conditions, and is common in many branches of physics. In our case, we can write it as

$$rv_y + v = 0, \quad y = 0, \tag{2}$$

where v is the velocity in the y direction and the subscript denotes partial derivation. Here r is a real positive quantity (the Robin parameter) that characterizes the physical conditions at the boundary. For example, if $r = 0$, we have an impermeable coastal wall. If on the other hand $r \to \infty$, then $v_y \to 0$ and there is no hindrance for particles to move through the boundary. In our case we take that r is small. Since v_y always must be finite, this means we now consider a small normal velocity at the coastline. This will be appropriate for an inner region with many narrow fjords and small islands.

In the Lofoten–Vesterålen region the relevant physical parameters typically are $H_2 = 2300\,\text{m}$, $H_0 = 50\,\text{m}$, $B = 60\,\text{km}$ and $b = 3.2 \cdot 10^{-5}\,\text{m}^{-1}$. Furthermore, the Coriolis parameter f is taken to be constant and equal to $1.3 \cdot 10^{-4}\,\text{s}^{-1}$. Using mid-depth as a reference depth, the barotropic Rossby radius a_0 is typically larger than 800 km. Hence, in the shelf region $B^2/a_0^2 \ll 1$. This means that we can make the rigid lid approximation [4]. In fact, a more thorough analysis for the CSW eigen-modes, allowing for a moving surface, shows that the rigid lid approximation is indeed well fulfilled for the Lofoten region; see [6] (their Fig. 5).

Generally, the velocity components in the x, y, z directions over the shelf are u, v, w, and the surface elevation is η. Furthermore, we introduce the notation $H(y) = H_1(y)$ for simplicity. With the rigid lid approximation, the continuity equation allows for the introduction of a stream function ψ such that $\tilde{u}H = -\psi_y$, and $\tilde{v}H = \psi_x$, where a tilde denotes the linear part of the wave field. We assume that the waves are so long that the pressure is hydrostatic in the vertical direction. Neglecting any effects of friction in the shelf region, the linearized momentum equations become

$$-\psi_{ty} - f\psi_x = -gH\tilde{\eta}_x, \tag{3}$$

$$\psi_{tx} - f\psi_y = -gH\tilde{\eta}_y. \tag{4}$$

Here g is the acceleration due to gravity. We now introduce a travelling wave solution [24] by

$$\psi = H^{1/2}\varphi(y)\exp i(\kappa x - \omega t), \tag{5}$$

where κ is the complex wave number (to allow for spatial damping), and ω is the real frequency. Then the governing equations reduce to

$$\varphi'' + l^2\varphi = 0, \tag{6}$$

where the asterisk denote derivation with respect to y, and

$$l^2 = 2fb\kappa/\omega - b^2 - \kappa^2. \tag{7}$$

At the edge of the shelf $y = B$, we must generally have continuity of pressure (here surface elevation) and normal fluxes. Utilizing that the deep ocean has a flat bottom, it easy to show that the continuity conditions imply for the stream function at the shelf edge that

$$\psi_y + \kappa\psi = 0, \qquad y = B, \tag{8}$$

see [20]. In terms of the φ function in (5), the boundary condition becomes

$$\varphi' + (b + \kappa)\varphi = 0, \quad y = B. \tag{9}$$

Writing the solution to (6) as

$$\varphi = H_0^{-1/2}[A\sin l(y - B) + C\cos l(y - B)], \tag{10}$$

we find by applying (9) that $C = -lA/(b + \kappa)$. Hence,

$$\varphi = AH_0^{-1/2}[\sin l(y - B) - (l/(b + \kappa))\cos l(y - B)]. \tag{11}$$

We note right away that if the coastal boundary is impermeable, i.e. $\varphi(0) = 0$ and κ real, (11) yields the familiar relation for the eigen-modes: $\tan(lB) = -l/(b + \kappa)$, as shown in [3]. In terms of φ, we can write (2)

$$r\varphi' + (1 + rb)\varphi = 0, \quad y = 0. \tag{12}$$

Using the solution (11), we then find the complex dispersion relation from (12). It becomes

$$(b+\kappa)\sin lB + l\cos lB = -r[\left(b^2 + l^2 + b\kappa\right)\sin lB - l\kappa\cos lB]. \tag{13}$$

In this paper, we consider spatial damping, i.e.

$$\kappa = k + i\alpha, \tag{14}$$

where α/k is a small quantity. It is then seen from (7) that l is complex. We take that the modified frequency is $\omega = \omega_0 + O(\alpha/k)^2$ (to be verified later). From (7) we then obtain

$$l = l_0(1 + i\delta). \tag{15}$$

Here

$$l_0^2 = 2fbk/\omega_0 - b^2 - k^2, \tag{16}$$

while the small imaginary part is

$$\delta = (\alpha/k)[b^2 + l_0^2 - k^2]/(2l_0^2). \tag{17}$$

Inserting (16) and (17) into (7), we find

$$\omega = \omega_0(1 + \alpha^2/k^2), \tag{18}$$

as anticipated, where ω_0 is determined by (16).

Using (14), and expanding the trigonometric functions appearing in (13), we find from the real part to lowest order that

$$\tan l_0 B = -l_0/(b + k), \tag{19}$$

as in [3]. From the imaginary part, we find to $O(\alpha/k)$ that

$$\alpha/k = [2Bl_0^2\{(b + k)^2 + l_0^2\}/\{\left(b^2 + l_0^2 - k^2\right)L - 2kl_0^2\}]r/B, \tag{20}$$

where $L = b + k + B(b + k)^2 + Bl_0^2$, and r/B is the small non-dimensional Robin parameter. In this problem, we can relate the attenuation coefficient directly to the group velocity $c_g = d\omega/dk$. From [20], eqn. (A.12), we find for CSWs

$$\left(b^2 + l_0^2 - k^2\right)L - 2kl_0^2 = c_g\left(b^2 + l_0^2 + k^2\right)L/c. \tag{21}$$

where $c = \omega_0/k$. By substituting into (20), we arrive at

$$\alpha/k = [2Bl_0^2\{(b + k)^2 + l_0^2\}/\{\left(b^2 + l_0^2 + k^2\right)L\}](c/c_g)(r/B). \tag{22}$$

Since c is always positive (CSWs propagate with shallow water to the right in the northern hemisphere [1]), we note from (22) that the sign of α is entirely dependent on the sign of c_g. For the present case of waves with K_1 frequency outside Lofoten, we notice from Fig. 5 that the wave number span for possible CSWs is rather small. Approximately, we find a permissible region $4 \cdot 10^{-5}\,\text{m}^{-1} < k < 7 \cdot 10^{-5}\,\text{m}^{-1}$, with zero group velocity for a critical wave number $k_c \approx 5.4 \cdot 10^{-5}\,\text{m}^{-1}$. For $k < k_c$, the wave energy propagates northwards, and the non-dimensional damping coefficient is positive. For example, $k = 4 \cdot 10^{-5}\,\text{m}^{-1}$ yields $\alpha/k = 3.0r/B$ from (22). For $k > k_c$, the group velocity is negative, and the energy propagates southwards. In this case,

with $x < 0$, we must have $\alpha < 0$ for damped waves. Taking $k = 7 \cdot 10^{-5}\,\mathrm{m}^{-1}$, we obtain $\alpha/k = -1.7r/B$ from (22).

We note that α/k in (22) becomes infinitely large when $c_g \to 0$ (positive when approached from the smaller wave number side and negative when approached from the larger wave number side). Obviously, our calculations assuming a small damping rate is not valid here, but this singular behaviour indicates that no wave energy escapes in either direction from the point where the group velocity is zero.

For the application in the nonlinear calculations in the next section, we state real parts of the linear velocity components.

$$\tilde{u} = -\psi_y/H = -[AH_0^{-1}\exp(-\alpha x - by)/(b+k)] \times [\left(bF + F'\right)\cos\theta - \delta l_0(bG + G')\sin\theta], \tag{23}$$

$$\tilde{v} = \psi_x/H = -[AH_0^{-1}\exp(-\alpha x - by)/(b+k)] \times [kF\sin\theta + (\alpha F + k\delta l_0 G)\cos\theta], \tag{24}$$

where $\theta = kx - \omega t$ is the phase function, and

$$F = (b+k)\sin l_0(y-B) - l_0\cos l_0(y-B), \tag{25}$$

$$G = (y-B)\left[(b+k)\cos l_0\,(y-B) + l_0\sin l_0(y-B)\right] - d\cos l_0(y-B). \tag{26}$$

Here

$$d = \left(b^3 + bl_0^2 - bk^2 + b^2k - l_0^2k - k^3\right)/[(b+k)(b^2+l_0^2-k^2)]. \tag{27}$$

4. The nonlinear drift problem

As demonstrated in [20], the spatial damping of the CSW field leads to nonzero radiation stresses [19] which drives the mean Lagrangian volume fluxes. In many cases of ocean wave problems, the damping is taken to be the result of bottom friction. For very long wave periods the theory by Charney and Eliassen [25] of vertical pumping in a quasi-steady Ekman bottom layer yields wave damping in the inviscid part of the fluid; see [24] for CSWs. For shorter periods (typically diurnal), the Ekman boundary layer is not properly developed, which makes this modelling dubious [26]. To avoid these problems, the usual approach is to assume a bottom stress that is linear or quadratic in the mean velocity [27].

The new idea of the present paper with a permeable coastal boundary, yields damping of the CSWs without the need to implement bottom friction. Although this makes the calculation of the radiation stress components lengthier due to the more complicated cross-shelf structure of the wave field, it simplifies considerably the derivation of the Lagrangian drift current.

In the previous sections, we considered the linearized equations. In calculating the mean drift, we need the equations to second order in wave steepness. We first define the mean nonlinear fluxes

$$\overline{U} = \overline{\int_{-H}^{\eta} u\,dz}, \quad \overline{V} = \overline{\int_{-H}^{\eta} v\,dz}, \tag{28}$$

where the over-bar denotes average over the wave cycle. These are actually the mean Lagrangian fluxes, since we integrate between material surfaces [18,28]. As before, we take that the waves are long enough to make the hydrostatic approximation. Integrating the inviscid governing equations in the vertical, and utilizing the full nonlinear boundary conditions at the free surface and the sloping bottom, we obtain for the mean quantities, correct to second order in wave steepness [18]:

$$\overline{U}_t - f\overline{V} = -gH\overline{\eta}_x + R^{(x)}, \tag{29}$$

$$\overline{V}_t + f\overline{U} = -gH\overline{\eta}_y + R^{(y)}, \tag{30}$$

$$\overline{\eta}_t = -\overline{U}_x - \overline{V}_y. \tag{31}$$

Here $R^{(x)}$, $R^{(y)}$ are the local radiation stress components; see [20], defined by

$$R^{(x)} = -\frac{1}{2}g(\overline{\tilde{\eta}^2})_x - \left(H\overline{\tilde{u}^2}\right)_x - (H\overline{\tilde{v}\tilde{u}})_y, \tag{32}$$

$$R^{(y)} = -\frac{1}{2}g(\overline{\tilde{\eta}^2})_y - (H\overline{\tilde{u}\tilde{v}})_x - \left(H\overline{\tilde{v}^2}\right)_y. \tag{33}$$

It was pointed out in [20] that since here $B^2/a_0^2 \ll 1$, the surface elevation terms in (32) and (33) are negligible compared to the velocity square terms.

We realize that the system of Eqs. (29)–(31) has time dependent free solutions (when we neglect the forcing from radiation stress terms) in the form of CSWs. These solutions vanish when we average over the wave period. We are here interested in the forced stationary solution to these equations. When $\partial/\partial t = 0$, it is found from the curl of (29) and (30) that

$$2bgH\overline{\eta}_x = R_x^{(y)} - R_y^{(x)}. \tag{34}$$

We note from (32) and (33) that if the waves are not spatially damped, i.e. if the x-derivative of the mean quantities is zero, both sides of (34) vanish, and it is not possible to determine $\overline{\eta}$. In this case, Lagrangian drift velocity along the bottom contours will contain an arbitrary part in geostrophic balance with a mean cross-shore surface tilt [29]. However, for spatially damped waves we find

$$gH\overline{\eta} = (1/(4\alpha b))\,[R_y^{(x)} - R_x^{(y)}]. \tag{35}$$

Hence, from (35)

$$gH\overline{\eta}_y = -(1/(4\alpha b))[2b\left(R_y^{(x)} - R_x^{(y)}\right) - R_{yy}^{(x)} + R_{xy}^{(y)}]. \tag{36}$$

By inserting into (30), we finally obtain for the Lagrangian mean flux

$$\overline{U} = (1/f)[R^{(y)} + (R_y^{(x)} - R_x^{(y)})/(2\alpha) + (R_{xy}^{(y)} - R_{yy}^{(x)})/(4\alpha b)]. \tag{37}$$

From the definitions (32) and (33) it is seen that $R_y^{(x)}$ and $R_{yy}^{(x)}$ are proportional to the small damping rate α. Hence, the Lagrangian mean flux along the shelf is independent of the damping rate (apart from the small amplitude attenuation). Calculation of the terms in (37) by applying (23) and (24), leads to

$$\overline{U} = \left[A^2\exp(-2\alpha x)/\left(fH_0(b+k)^2\right)\right] \times [-2k^2FF' + k^2\left(FF'' + F'^2\right)/(2b) + Q'/4 - Q''/(8b)]. \tag{38}$$

Here

$$Q = 2(bF+F')^2 - [(bF+F')\{F + \left(b^2 + l_0^2 - k^2\right)G/(2l_0)\} - \left(b^2 + l_0^2 - k^2\right)(bG+G')F/(2l_0)]', \tag{39}$$

where F and G are given by (25) and (26), respectively. The corresponding along-shore Lagrangian drift velocity then becomes

$$\overline{u}_L = \overline{U}/H. \tag{40}$$

Since the constant A in the stream function (5) has dimension $\mathrm{m}^3\,\mathrm{s}^{-1}$, we can introduce a dimensional scaling factor u_0 for the drift velocity as

$$u_0 = A^2b^3\exp(-2\alpha x)/(fH_0^2). \tag{41}$$

The Lagrangian mean velocity can then be written

$$\overline{u}_L = u_0[\exp(-2by)/(8b^4\,(b+k)^2)]$$

$$\times\ [-16bk^2FF' + 4k^2\left(FF'' + F'^2\right) + 2bQ' - Q'']. \tag{42}$$

In Fig. 7 we have depicted the non-dimensional Lagrangian drift current (42) for $B = 60$ km, and $b = 3.2 \cdot 10^{-5}$ m^{-1}, which are typical parameter values for CSWs with diurnal frequency outside Lofoten. With reference to Fig. 5, we first consider the region where the group velocity is positive (northward propagating energy) and take $k = 4 \cdot 10^{-5}$ m^{-1}. The corresponding value of the cross-shelf wave number then becomes $l_0 = 4.3 \cdot 10^{-5}$ m^{-1}. Secondly, we compute the Lagrangian drift current for the case when the group velocity is negative (southward propagating energy). In this case we take $k = 7 \cdot 10^{-5}$ m^{-1}, and $l_0 = 4.5 \cdot 10^{-5}$ m^{-1}.

We observe from the figure that the Lagrangian drift velocity is basically located over the shallow part of the shelf with a positive value at the inner 10 km, and a distinct maximum at the coast. Between 10 km and 40 km the drift is negative (southward) with a smaller maximum value. We note that in the case of negative group velocity (dashed curve) the maximum at the coast as well as the southward flow are larger.

In the present formulation, we obtain directly the Lagrangian mean flow, as pointed out in [18]. Quite often, however, the Stokes drift [30] is taken to represent the particle drift in periodic waves. This can be misleading, as we show below.

To second order in wave steepness, the Stokes drift $\overline{u}_S$ can be written (Longuet-Higgins [31]):

$$\overline{u}_S = \overline{(\int \tilde{u}dt)\tilde{u}_x} + \overline{(\int \tilde{v}dt)\tilde{u}_y}. \tag{43}$$

It is readily found from (23) and (24) that

$$\overline{u}_S = u_0(b^2 + l_0^2 + k^2)[\exp(-2by)/(4b^4\,(b+k)^2)][2bFF' + FF'' + F'^2]. \tag{44}$$

The Stokes drift is related to the mean momentum in the wave motion, and is virtually independent of the effect of a small friction. However, as pointed out in [31], for problems with decaying waves the mean wave momentum will not be lost, but reappear as Eulerian mean currents. Hence, we can write the Lagrangian mean velocity as

$$\overline{u}_L = \overline{u}_S + \overline{u}_E, \tag{45}$$

where $\overline{u}_E$ is the mean Eulerian current. Accordingly, we have for the Eulerian mean current that

$$\overline{u}_E = \overline{u}_L - \overline{u}_S. \tag{46}$$

To compare the magnitude and spatial variation of the various non-dimensional drift components, we have plotted them in Fig. 8 for $B = 60$ km, $b = 3.2 \cdot 10^{-5}$ m^{-1}, $l_0 = 4.3 \cdot 10^{-5}$ m^{-1}, and $k = 4 \cdot 10^{-5}$ m^{-1}, i.e. positive group velocity as seen from Fig. 5.

We note that the Stokes drift (blue curve) is positive over almost the entire shelf. Accordingly, by considering only the Stokes drift, this would yield a very incomplete picture of how floating particles in the sea (cod egg and larvae, oil spill) are transported by CSWs along the shelf. In particular, one would miss the larger maximum drift velocity at the coast, as well as the negative drift over the upper part of the slope, as seen from the black curve in Fig. 8.

5. Hydrographic conditions west of Norway

West of Norway we find two northward flowing currents. Here the relatively fresh and cold Norwegian Coastal Current (NCC) is trapped at the coast. It is wedge shaped, reaching down to about 100 m at the coast, with a typical width of 50 km, and near-surface velocities of the order 0.3 m s^{-1} [32]. The saltier and warmer Norwegian Atlantic Current (NwAC) is located further west. Outside Lofoten the core is typically 30 km wide. It reaches down to about 600 m, and has a maximum outside the shelf break with surface velocities of the order 0.3 m s^{-1} [33]. From our results, we realize that it is the NCC, with its location over the shallow part of the shelf, which mostly may affect the Lagrangian wave-induced drift due to diurnal CSWs. In our earlier example with $B = 60$ km, $b = 3.2 \cdot 10^{-5}$ m^{-1}, $l_0 = 4.3 \cdot 10^{-5}$ m^{-1}, and $k = 4 \cdot 10^{-5}$ m^{-1}, we find that the phase speed is $c = \omega/k = 1.8$ m s^{-1}. In this case we obtain for the group velocity from [20] that $c_g = 0.4$ m s^{-1}. For negative group velocity, with $k = 7 \cdot 10^{-5}$ m^{-1}, and $l_0 = 4.5 \cdot 10^{-5}$ m^{-1}, we find $c = 1$ m s^{-1}, and $c_g = -0.26$ m s^{-1}. We thus see that little (if any) wave energy will be located south of Lofoten in this case.

6. Discussion and concluding remarks

Numerical modelling of the tidal motion in the Lofoten–Vesterålen region [21,22] reveals a distinct amplification of the currents for the tidal diurnal K_1 component. By analogy with the generation of CSWs due to tidal flow in the Bass strait [7–9] we suggest that the strong Moskstraumen is instrumental in generating diurnal CSWs along the narrow continental shelf outside Lofoten; see also [22]. This is supported by results from the dispersion relation, showing that CSWs with diurnal frequencies are possible in a small wave number range centred around zero group velocity.

At the inner part of the shelf west of Norway, there are a multitude of small islands and narrow fjords. We here attempt to model the effect on the CSWs when the coastal boundary is permeable, through the application of a Robin condition. This is a novel approach that leads to spatial damping of the CSWs in the inviscid region over the sloping shelf. Nonlinearly, this damping makes it possible to determine the radiation stress components that force the Lagrangian depth averaged mean current along the shelf.

As an alternative to the Robin condition, it is possible to model the coastal archipelago as an idealized macroscopic porous medium governed by Darcy's law [34], and study the wave-induced exchange of fluid between the shelf and the porous inner layer. Now continuity of normal flow and pressure (here surface elevation) must be assumed at the common permeable boundary. A similar nonlinear problem of surface waves over a porous bottom layer has been studied in [15] and in [35]. With a porous inner shelf, the damping rate becomes a function of the macroscopic permeability and the eddy viscosity. However, this modelling complicates the algebra considerably. We will therefore not pursue this idea here.

The present analysis assumes a barotropic ocean, whereas the Lofoten region in reality is stratified. Huthnance [36] has considered the effect of stratification on trapped shelf waves in terms of the Burger number; see also [37]. However, idealized numerical model runs in [38] and [39] have revealed that the effect of stratification on CSWs are small along the Norwegian shelf. This indicates that the Burger number is small, as pointed out in [6].

The most interesting result of the nonlinear analysis of the present paper is that the Lagrangian mean current is independent of the value of the damping coefficient, however small, as long as it is nonzero. This is a clear parallel to the singular behaviour of the wave-drift problem in a direct Lagrangian description. In this formulation, the limit of solutions as a small viscosity $\nu \to 0$ is different from solutions obtained with $\nu = 0$; see [40]. Since the Stokes drift represents the inviscid mean wave momentum, it is the Eulerian mean current that is independent of the magnitude of the damping in this problem. This is special, since the Eulerian mean current normally increases when the effect of friction

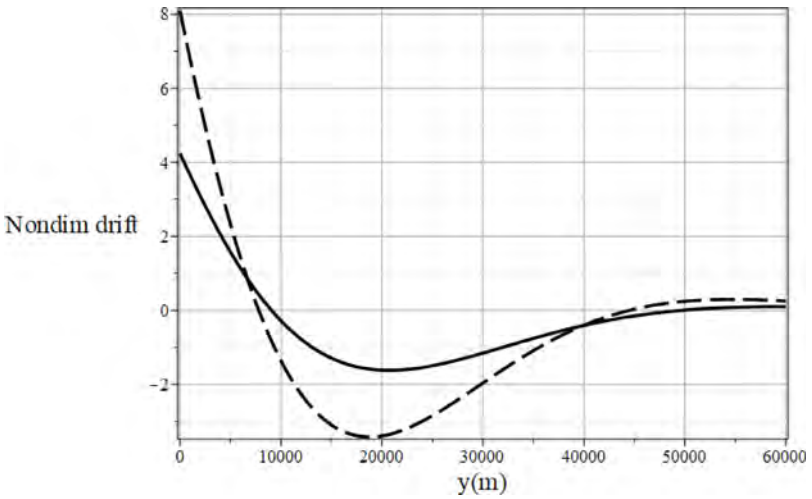

Fig. 7. The non-dimensional Lagrangian drift velocity $\overline{u}_L/u_0$ over the sloping shelf as function of the seaward coordinate. Solid curve: $k = 4 \cdot 10^{-5}\,\mathrm{m}^{-1}$ (positive group velocity). Dashed curve: $k = 7 \cdot 10^{-5}\,\mathrm{m}^{-1}$ (negative group velocity).

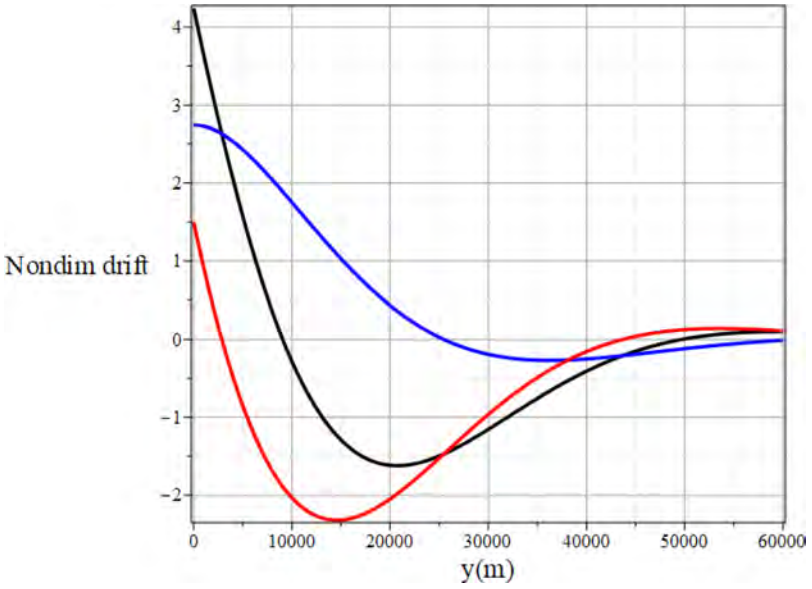

Fig. 8. Nondimensional drift velocities $\overline{u}_L/u_0$ (black), $\overline{u}_S/u_0$ (blue) and $\overline{u}_E/u_0$ (red) over the sloping shelf as function of the seaward coordinate for $k = 4 \cdot 10^{-5}\ \mathrm{m}^{-1}$ (positive group velocity). (For interpretation of the references to colour in this figure legend, the reader is referred to the web version of this article.)

(bottom friction or bulk friction) increases. In digression, it could be mentioned that for the case where the damping is caused by the interaction with an inner porous shelf instead of the Robin condition, as mentioned above, the result that the Lagrangian mean drift is independent of the damping coefficient becomes the same.

From the present calculations we note that by considering only the wave-induced Stokes drift, as often done, one would assess that particles, like cod egg and larvae, would drift northward over the entire shelf, and with a smaller speed than they actually have. This shows the importance of calculating the Lagrangian mean drift (Stokes plus Euler) when assessing wave-induced transports in the ocean. Concerning the dimensional magnitude of the Lagrangian drift, we note from Moe et al. [22] that the observed surface amplitude of the K_1 component in this area lies in the range 5–10 cm (their Table 2). If we take $\left|\tilde{\eta}_{K_1}\right| = 7$ cm as a typical value, and calculate the stream function amplitude from (3), we find that the Lagrangian drift velocity scale (41) then becomes $u_0 = 1.4$ cm s^{-1}. From Fig. 7 we thus infer that the dimensional Lagrangian drift velocity over the shallow part of the shelf due to the diurnal CSW is comparable in magnitude to the NCC.

Finally, it should be emphasized that the drift results for CSWs with a permeable coastal boundary is not valid only for diurnal waves as shown here, but applies in general to longer waves generated by moving weather systems over the continental shelf.

Declaration of competing interest

The authors declare that they have no known competing financial interests or personal relationships that could have appeared to influence the work reported in this paper.

Acknowledgements

The authors gratefully acknowledge support from the Research Council of Norway through Grant 280625 (JEW, travel) and by VISTA — a basic research program in collaboration between The Norwegian Academy of Science and Letters, and Equinor (EB, funding).

References

[1] M.S. Longuet-Higgins, Some dynamical aspects of ocean currents, Quart. J. R. Met.Soc. 91 (1965) 425–451.
[2] M.S. Longuet-Higgins, Double Kelvin waves with continuous depth profiles, J. Fluid Mech. 34 (1968) 49–80.
[3] V.T. Buchwald, J.K. Adams, The propagation of continental shelf waves, Proc. Roy. Soc. Lond. A 305 (1968) 235–250.
[4] A.E. Gill, E.H. Schumann, The generation of long shelf waves by the wind, J. Phys. Oceanogr. 4 (1974) 83–90.
[5] E.A. Martinsen, B. Gjevik, L.P. Røed, A numerical model for long barotropic wavesand storm surges along the western coast of Norway, J. Phys. Oceanogr. 9 (1979) 1126–1138.
[6] M. Drivdal, J.E. Weber, J.B. Debernard, Dispersion relation for continental shelfwaves when the shallow shelf part has an arbitrary width: Application to the shelf west of Norway, J. Phys. Oceanogr. 46 (2016) 537–549.
[7] V.T. Buchwald, B.J. Kachoyan, Shelf waves generated by coastal flux, Aust. J. Mar. Freshwater Res. 38 (1987) 429–437.
[8] J.F. Middleton, Long shelf waves generated by a coastal flux, J. Geophys. Res. 93 (1988) 10, 724-10, 730.
[9] R.A. Morrow, I.S.F. Jones, R.L. Smith, P.J. Stabeno, Bass strait forcing of coastaltrapped waves: ACE revisited, J. Phys. Oceanogr. 20 (1990) 1528–1538.
[10] D.E. Cartwright, Extraordinary tidal currents near St. Kilda, Nature 223 (1969) 928–932.
[11] F.-P.A. Lam, Shelf waves with diurnal tidal frequency at the greenland shelf edge, Deep-Sea Res. I 46 (1999) 895–923.
[12] A. Ommundsen, Models of cross shelf transport introduced by the Lofoten Maelstrom, Cont. Shelf Res. 22 (2002) 93–113.
[13] B. Gjevik, H. Moe, A. Ommundsen, Sources of the maelstrom, Nature 388 (1997) 837–838.
[14] R.O. Reid, K. Kajiura, On the damping of gravity waves over a permeable sea bed, Trans. Am. Geophys. Union 38 (1957) 662–666.
[15] J.J. Webber, H.E. Huppert, Stokes drift in coral reefs with depth-varying permeability, Phil. Trans. R. Soc. A 378 (2020) 20190531.
[16] K. Gustafson, Domain decomposition, operator trigonometry, Robin condition, Contemp. Math. 218 (1998) 432–437.
[17] J.E. Akin, Finite Element Analysis with Error Estimators: An Introduction To the FEMand Adaptive Error Analysis for Engineering Students, Elsevier, Butterworth-Heinemann, 2005.
[18] O.M. Phillips, The Dynamics of the Upper Ocean, Second Ed, Cambridge University Press, Cambridge, 1972.
[19] M.S. Longuet-Higgins, R.V. Stewart, Changes in the form of short gravity waves on long waves and tidal currents, J. Fluid Mech. 8 (1960) 565–583.
[20] J.E. Weber, M. Drivdal, Radiation stress and mean drift in continental shelf waves, Cont. Shelf Res. 35 (2012) 108–116.
[21] E. Børve, O.A. Nøst, P.E. Isachsen, Rectified tidal transports in Lofoten region, northern Norway, Ocean Sci. (2021) Submitted for publication.
[22] H. Moe, A. Ommundsen, B. Gjevik, A high resolution tidal model for the area around the Lofoten Islands, Cont. Shelf Res. 22 (2002) 485–504.
[23] A. Ommundsen, B. Gjevik, Scattering of tidal kelvin waves along shelves which vary intheir lengthwise direction, in: Preprint Series, Department of Mathematics, University ofOslo, 2000, p. 24.
[24] A.E. Gill, Atmosphere-Ocean Dynamics. Int. Geophys. Ser. 30, Academic Press, 1982.
[25] J.G. Charney, A. Eliassen, A numerical method for predicting the perturbations of themiddle latitude westerlies, Tellus 1 (1949) 38–54.
[26] H. Mitsudera, K. Hanawa, Effects of bottom friction on continental shelf waves, Cont. Shelf Res. 7 (1987) 699–714.
[27] E. Nøst, Calculating tidal current profiles from vertically integrated models near the critical latitude in the Barents Sea, J. Geophys. Res. 99 (1994) 7885–7901.
[28] J.E. Weber, G. Broström, Ø. Saetra, Eulerian versus Lagrangian approaches to the wave-induced transport in the upper ocean, J. Phys. Oceanogr. 36 (2006) 2106–2118.
[29] D. Moore, The mass transport velocity induced by free oscillations at a single frequency, Geophys. Fluid Dyn. 1 (1970) 237–247.
[30] G.G. Stokes, On the theory of oscillatory waves, Trans. Cam. Phil. Soc. 8 (1847) 441–455.
[31] M.S. Longuet-Higgins, Mass transport in water waves, Phil. Trans. R. Soc. A 245 (1953) 535–581.
[32] M. Mork, Experiments with theoretical models of the norwegian coastal current, in: R. Sætre, M. Mork (Eds.), The Norwegian Coastal Current, II, University of Bergen, 1981.
[33] I. Fer, A. Bosse, J. Dugstad, Norwegian atlantic slope current along the lofoten escarpment, Ocean Sci. 16 (2020) 685–701.
[34] J. Bear, Dynamics of Fluids in Porous Media, American Elsevier Publ. Comp. NY, 1972.
[35] J.E. Weber, P. Ghaffari, Wave-induced drift in a porous seabed, Env. Fluid Mech. (2021) Submitted for publication.
[36] J.M. Huthnance, On trapped waves over a continental shelf, J. Fluid Mech. 69 (1975) 689–704.
[37] L.A. Mysak, Recent advances in shelf wave dynamics, Rev. Geophys. Space Phys. 18 (1980) 211–241.
[38] B. Gjevik, Simulations of shelf sea response due to travelling storms, Cont. Shelf Res. 11 (1991) 139–166.
[39] L.H. Slørdal, E.A. Martinsen, A.F. Blumberg, Modelling the response of an idealizedcoastal ocean to a travelling storm and to flow over bottom topography, J. Phys. Oceanogr. 24 (1994) 1689–1705.
[40] J.E. Weber, Lagrangian studies of wave-induced flows in a viscous ocean, Deep-Sea Res. II 160 (2019) 68–81.